Radar remote sensing of wind vector and turbulence intensity fields from raindrop backscattering

Oude Nijhuis, Albert

Important note
To cite this publication, please use the final published version (if applicable).
Please check the document version above.

Radar remote sensing of wind vector and turbulence intensity fields from raindrop backscattering

Radar remote sensing of wind vector and turbulence intensity fields from raindrop backscattering

Dissertation

for the purpose of obtaining the degree of doctor
at Delft University of Technology
by the authority of the Rector Magnificus prof.dr.ir. T.H.J.J. van der Hagen,
chair of the Board for Doctorates,
to be defended publicly on
Wednesday 16 January 2019 at 15:00 o'clock

by

Albert Christiaan Plechelmus OUDE NIJHUIS

Master of Science in Meteorology, Physical Oceanography and Climate,
Utrecht University, the Netherlands,
born in Oldenzaal, the Netherlands.

This dissertation has been approved by the promotors.

Composition of the doctoral committee:

Rector Magnificus	chairperson
Prof.dr. A.G. Yarovoy	Delft University of Technology, promotor
Prof.dr.ir. H.W.J. Russchenberg	Delft University of Technology, promotor
Dr. O.A. Krasnov	Delft University of Technology, copromotor

Independent members:

Prof.dr. V. Chandrasekaran	Colorado State University
Prof.ir. F. Le Chevalier	Delft University of Technology
Prof.dr. A.P. Siebesma	Delft University of Technology
Prof.dr.ir. G.J.T. Leus	Delft University of Technology
Prof.dr.ir. R.F. Hanssen	Delft University of Technology

Ir. C.M.H. Unal has contributed significantly to the preparation of this dissertation.

TUDelft
Delft
University of
Technology

An electronic version of this dissertation is available at
https://repository.tudelft.nl/

Author e-mail: albertoudenijhuis@gmail.com

Contents

Summary

Scanning radars are promising sensors for atmospheric remote sensing, giving potential to retrieve parameters that characterize the local air dynamics during rain. For observing air motion radars are relying on the backscatter of particles, which can, for example, be raindrops or insects. To measure wind vectors and turbulence intensities remotely during rain the radar is a common choice. This is mainly because the radar signals are not attenuated too much by the rain itself, which is the case for instruments operating at other frequencies, such as lidars. There is, however, a problem with measuring air dynamics from raindrops. Raindrops are not perfect tracers of the air motion. It may thus be necessary to make some corrections when air-dynamics parameters are estimated with a radar during the rain, and account for that raindrops are imperfect tracers of the air motion. This dissertation focuses on this problem. In addition, existing radar-based wind vector and turbulence intensity retrieval techniques are assessed for when they are applied during the rain, and they have been further developed.

Nowadays, well-validated (experimentally and theoretically) formulas exist for the raindrop terminal fall velocity, which are based on a balance between the forces acting on a raindrop. In Chapter 2 the next step is taken, and raindrop inertial parameters are derived by considering an imbalance of forces acting on a raindrop. Based on the 'sudden jump' case, inertial distance and inertial time parameters are derived for each raindrop size, with different formulations for the x/y-direction and the z-direction. These parameters are essential for the development of models and retrieval techniques that take the influence of measuring from imperfect air tracers (read: raindrops) into account. A new raindrop-inertia-correction model was proposed that can easily be integrated into existing turbulence models and retrieval techniques as an extra factor. From simulations it was derived that for large radar total sampling scales ($\gg 30$ m), the influence of raindrop inertia on retrieved turbulence intensities becomes negligible. For radar total sampling scales comparable to or smaller than 30 m, the raindrop-inertia-correction model was suggested. For small radar total sampling scales (< 10 m) and large raindrops (e.g. 4 mm), the application of the proposed correction model becomes limited, because the uncertainty in the retrieved turbulence intensity becomes very large as a result of the influence of raindrop inertia.

In Chapter 3, state-of-the-art and commonly-used turbulence intensity retrieval techniques are assessed, when they are applied to raindrop-backscattering radar Doppler measurements. The inertia correction model was not used here for two reasons: (1) it is assumed that often a good estimation of the drop size distribution (DSD) is not available; and (2) it can be expected that the influence of inertia is negligible when a large total sampling scale is used. The quality of retrieved values for the energy dissipation rate (EDR) was optimized, based on comparisons with

in situ measurements from a sonic anemometer. As a result, the most optimal technique is the wind speed variance (WSV) EDR retrieval technique, which uses the full 3D wind vector from a profiling radar, TARA. Other turbulence intensity retrieval techniques, which rely on terminal fall velocity corrections, and thus depend on accurate estimation of the DSD, are compromised by errors in the estimated turbulence spectral width. For further applications, it is recommended that the concept of EDR is applied cautiously, because of complex estimation errors. It is suggested to always estimate a minimal retrievable EDR, give uncertainty estimates for the retrieved EDR value, and provide the sampling and total sampling scales that were used in the EDR retrieval technique.

In Chapter 4 the focus is on radar-based retrieved wind vectors. From a few simulations of raindrop motions in predefined wind fields, it was concluded that only for very special weather conditions a substantial influence of raindrop inertia on the retrieved wind vectors can be expected. As this work is not aimed at such special weather conditions, the influence of raindrop inertia is not accounted for in wind vector retrieval techniques that are proposed and studied in this work.

A new wind vector retrieval technique was developed and implemented, which is the four-dimensional variational analysis (4D-Var) wind vector retrieval technique, which provides a more coherent and realistic wind field in comparison to other existing techniques. With the 4D-Var wind vector retrieval technique, it is also possible to show the solution space of wind vectors, which are associated with measurements from a single scanning Doppler radar.

In the case of insufficient or no in situ wind vector measurements for validation, an alternative approach for quantitative validation of radar-based retrieved wind vectors is desired. Therefore, measures for curl and divergence of the wind vector field are used to qualify and optimize the retrieved wind vectors. By selecting the right settings for a wind vector retrieval technique, retrieval of spurious wind vectors can be prevented, which are related to the implementation and configuration of an algorithm.

In Chapter 5, the application of raindrop-backscattering radar-based turbulence intensity retrieval techniques to small sampling scales is studied in detail. With "small sampling scales" the radar resolution volume scale of modern research weather radars is meant, which has a typical spatial scale of 30 m. A non-stochastic turbulence implementation to model radar observables is developed, the so-called "ensemble of isotropic vectors" approach, which can be used in radar-based turbulence intensity retrieval techniques. The goal for this turbulence implementation is to get the same turbulence-intensity dependencies in the polarimetric radar observables as for stochastic turbulence implementations. A novelty of this "ensemble of isotropic vectors" approach is that it implicitly reproduces the canting angle distribution of raindrops, on which so many polarimetric radar observables depend.

The performance of the proposed technique is demonstrated in a case study. It was not possible to use radar-based estimations of the DSD in this case study at small sampling scales, because several state-of-the-art radar-based DSD estimations overestimated the Doppler spectral width due to raindrop terminal fall velocities. Therefore, in situ ground-level DSD measurements have been used in this

case study. With the ground-level DSD information, the application of the raindrop-inertia-correction model is demonstrated for radar-based turbulence intensity retrieval techniques applied to the small sampling scales of modern research weather radars during the rain.

In Chapter 6, the application of raindrop-backscattering radar-based retrieval techniques is demonstrated at an airport. This was done within the UFO project and can be used in the future to reduce wind hazards at airports. The 4D-Var wind vector retrieval technique is recommended, as it has several advanced processing features. In particular, this technique gives more control and versatility in the solutions. For turbulence intensity retrieval techniques applied at airports, it is recommended to avoid corrections for raindrop inertia, which relies on accurate estimation of the DSD.

Samenvatting

Scannende radars zijn veelbelovend voor remote sensing van de atmosfeer, en hebben de potentie om lokale luchtdynamicaparameters te leveren tijdens de regen. Voor de observatie van luchtbewegingen rekenen radars op deeltjes die de radiosignalen terugkaatsen. Die deeltjes kunnen bijvoorbeeld regendruppels of insecten zijn. Voor het meten van windvectoren of turbulentie intensiteit op afstand tijdens de regen is de radar een vanzelfsprekende keuze. Dat is voornamelijk zo omdat de elektromagnetische signalen afkomstig van de radar niet te veel worden gedempt door de regen, wat wel het geval is voor instrumenten die opereren op andere golflengtes zoals lidars. Er is toch - helaas pindakaas - een probleem met het meten van luchtdynamicaparameters door middel van regendruppels. De regendruppels zijn geen perfect volgers van de luchtbeweging. Het kan dus nodig zijn om enkele correcties te maken, wanneer luchtdynamicaparameters worden geschat met een radar tijdens de regen, en rekening te houden met dat de regendruppels een bepaalde mate van traagheid hebben. Deze dissertatie houdt zich met dit probleem bezig. Daarnaast zijn in dit werk bestaande op-radar-gebaseerde wind vector en turbulentie intensiteit schattingsalgoritmes beoordeeld voor wanneer ze worden toegepast tijdens de regen, en deze schattingsalgoritmes zijn verder doorontwikkeld.

Tegenwoordig bestaan er goed gevalideerde (zowel experimenteel als theoretisch) formules voor regendruppel terminale valsnelheden, die zijn gebaseerd op een balans van krachten op een regendruppel. De daarop volgende stap wordt in Hoofdstuk 2 genomen, door het beschouwen van het geval dat de krachten op een regendruppel uit balans zijn. Gebaseerd op het "ogenblikkelijke sprong" geval, worden parameters geschat voor de traagheidsafstand en de traagheidstijd voor iedere regendruppel met verschillende formuleringen voor de x/y-richting en de z-richting. Deze parameters zijn essentieel voor het ontwikkelen van modellen en schattingsalgoritmes die de invloed van het meten vanaf niet-perfecte volgers (lees: regendruppels) in rekening brengen.

Een nieuw regendruppel-traagheid-correctie-model wordt voorgesteld, dat makkelijk kan worden geïntegreerd in bestaande turbulentiemodellen en schattingsalgoritmes als een extra factor. Met simulaties wordt afgeleid dat wanneer grote ruimtelijke schalen voor bemonstering worden gebruikt ($\gg$ 30 m) met de radar, de invloed van regendruppeltraagheid op de gemeten turbulentie intensiteit verwaarloosbaar wordt. Voor kleine ruimtelijke schalen voor bemonstering ($<$ 10 m) en grote regendruppels (e.g. 4 mm), wordt de toepassing van het voorgestelde correctiemodel zeer beperkt, aangezien de onzekerheid in de geschatte turbulentie intensiteit zeer groot wordt, als gevolg van de invloed van regendruppeltraagheid.

In Hoofdstuk 3 worden de nieuwste en veelgebruikte turbulentie intensiteit schattingsmethoden beoordeeld, voor wanneer deze worden toegepast op radar

Doppler metingen tijdens de regen. Het traagheid-correctie-model is hier niet gebruikt vanwege twee redenen: (1) Het wordt aangenomen dat er vaak een goede schatting van de regendruppelverdeling ontbreekt; en (2) het kan worden verwacht dat de invloed van traagheid verwaarloosbaar is, zolang een grote ruimtelijke schaal voor bemonstering wordt gebruikt.

De kwaliteit van de geschatte waarden voor de energy dissipation rate (EDR) wordt verbeterd, gebaseerd op vergelijkingen met in situ metingen van een sonic anemometer. Als resultaat komt naar voren dat het meest optimale schattingsalgoritme het wind speed variance (WSV) EDR schattingsalgoritme is, die gebruikt maakt van de volledige 3D windvector van een profilerende radar, namelijk TARA. Andere turbulentie intensiteit schattingsalgoritmes, die afhangen van terminale-valsnelheid-correcties, en daardoor afhangen van een nauwkeurige regendruppel-verdeling, zijn gecompromitteerd door fouten in de geschatte turbulentie spectral breedte. In verdere toepassing, wordt het aangeraden het concept van EDR voorzichtig te gebruiken, vanwege complexe schattingsfouten. Het wordt aangeraden om altijd een minimaal-schatbare EDR waarde te leveren, onzekerheden te geven voor de gevonden EDR waarde, en de gebruikte bemonsteringsschalen te leveren die zijn gebruikt in het EDR schattingsalgoritme.

In hoofdstuk 4 verschuift de aandacht naar op-radar-gebaseerde windvectoren. Aan de hand van een paar simulaties van regendruppelbeweging in vooraf bepaalde windvelden, wordt geconcludeerd dat alleen voor zeer speciale weercondities een substantiële invloed van regendruppeltraagheid kan worden verwacht op de geschatte windvectoren. Aangezien dit werk niet is gericht op zulke speciale weercondities, wordt de invloed van regendruppeltraagheid niet meegenomen in de windvector schattingsalgoritmes die worden voorgesteld en bestudeerd in dit werk.

Een nieuwe windvectorschattingsalgoritme is ontwikkeld en geïmplementeerd, het zogenaamde vierdimensionale variatonele analyse (4D-Var) windvectorschattingsalgoritme, die meer coherente en realistische windvelden levert in vergelijking met andere technieken. Met het 4D-Var windvectorschattingsalgoritme is het ook mogelijk om de oplossingsruimte van windvectoren te laten zien, met betrekking tot de radar Doppler metingen.

In het geval van onvoldoende of een gebrek aan in situ windvector metingen voor validatie, is er behoefte aan een alternatieve aanpak voor een kwantitatieve validate van op-radar-gebaseerde gevonden windvectoren. Daarom zijn de maten voor rotatie en divergentie van windvelden gebruikt, om de gevonden windvectoren te kwalificeren en te optimaliseren. Door het selecteren van de juiste instellingen van een windvector schattingsalgoritme, kunnen rare uitschieters worden voorkomen die te maken hebben met de implementatie van het algoritme.

In Hoofdstuk 5 wordt de toepassing van regendruppel-terugkaatsing op-radar-gebaseerde turbulentie schattingsalgoritmes op kleine bemonsteringsschalen bestudeerd in detail. Met "kleine bemonsteringsschalen" wordt de radar resolutie volume schaal bedoeld van moderne onderzoeksweerradars, die een typische lengteschaal hebben van zo'n 30 m.

Een niet-stochastische turbulentie implementatie om radar waarnemingen te modelleren is ontwikkeld, de zogenaamde "ensemble of isotropic vectors" methode,

die kan worden gebruikt in op-radar-gebaseerde turbulentie-intensiteit schattings-algoritmes. Het doel van deze turbulentie implementatie is om dezelfde afhankelijk-heden voor turbulentie intensiteit te krijgen in polarimetrische radarwaarnemingen als voor stochastische turbulentie implementaties. Een nieuwtje aan deze "ensemble of isotropic vectors" methode is dat het impliciet de kantelhoekdistributie van regendruppels modelleert, waarvan de polarimetrische radarwaarnemingen sterk afhangen.

De prestatie van het voorgestelde algoritme wordt gedemonstreerd in een case study. Hierbij was het niet mogelijk om op-radar-gebaseerde schattingen van de regendruppelverdeling te gebruiken op de kleine bemonsteringsschalen, omdat alle op-radar-gebaseerde regendruppelverdelingen een overschatting van de Doppler spectrale breedte voor regendruppel valsnelheden maakten. Daarom zijn er in situ grondwaarnemingen van regendruppelverdelingen gebruikt voor deze case study. Met de grondwaarnemingen van de regeldruppelverdeling, kon dan toch de toepassing van het regendruppel-traagheid-correctiemodel worden gedemonstreerd voor op-radar-gebaseerde turbulentie intensiteit schattingsalgoritmes voor de kleine bemonsteringsschalen van moderne onderzoeksweerradars tijdens de regen.

In hoofdstuk 6 wordt de toepassing van regendruppel-terugkaatsing op-radar-gebaseerde schattingsalgoritmes gedemonstreerd bij een luchthaven. Dit was gedaan in het UFO project, en kan in de toekomst worden gebruikt om gevaren van wind te verminderen op luchthavens. Hiervoor wordt het 4D-Var windvectorschattings-algoritme aanbevolen, omdat het enkele geavanceerde verwerkingsmogelijkheden heeft. In het bijzonder geeft deze techniek meer veelzijdigheid aan en controle over de oplossingen. Voor turbulentie-intensiteit schattingsalgoritmes die worden toegepast op luchthavens, wordt het aangeraden om regendruppeltraagheidcorrecties te vermijden, aangezien die afhangen van een nauwkeurige schatting van de regendruppelverdeling.

1

Introduction

Let me tell you
what this research
is about ...

---
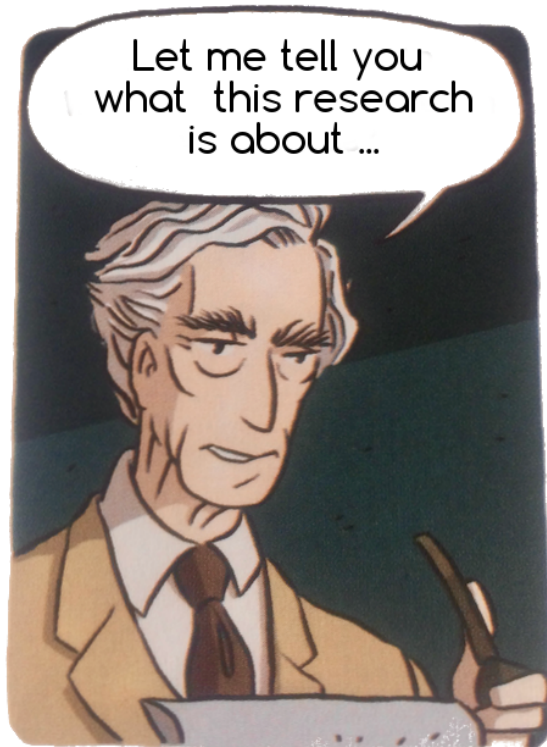
[1]Illustration adapted from the "logicomix", a nice graphic novel about the search for absolute truth in mathematics (Doxiadēs et al. 2009).

1

This research is dedicated to wind vector and turbulence intensity field retrieval techniques during rain by using weather radars. To understand this in more detail, first the relevant topics are introduced separately, which are: 1. wind vector and turbulence intensity fields, 2. weather radar remote sensing and, 3. raindrop backscattering. Subsequently, the research challenges are stated. And finally, the dissertation structure and approaches are described.

1.1. Wind vector and turbulence intensity fields

The knowledge of wind vector and turbulence intensity fields is relevant for many applications, such as aviation, shipping, recreation and atmospheric sciences. Certain weather phenomena, such as tornadoes and thunderstorms, are essential to detect in order to protect people from hazardous situations. Next to that, it is of interest to quantify the strength of a specific storm to give a more refined image of its potential hazard. Typical measures for a storm strength are the average wind speed [m s^{-1}] and the maximum gust wind speed [m s^{-1}]. Next to that, wind shear [s^{-1}] is a measure of the gradient of the wind speed, which is in particular of interest for aviation. Wind vectors can be measured in situ with cup or sonic anemometers. Wind vectors can also be measured remotely via the Doppler effect, where the frequency change of transmitted electromagnetic signals, backscattered from particles in the air, can be used to estimate the air motion. Such measurements of wind vectors have the potential to reduce and better estimate the risks of hazardous weather situations.

Regarding safety, wind hazards play an important role in aviation, especially during the take-off and landing phases, where the majority of accidents occur (Boeing 2013). Beside natural wind hazards, airport capacities are also limited by regulations for minimum distance separations between aircraft (ICAO 2007b). These distances have been defined for the worst weather conditions, which are low wind speed and/or low turbulence intensities that have the longest-lasting wake turbulence, to avoid the risks for a follower aircraft to encounter the wake turbulence from the leader aircraft. To further increase airport capacity, the dynamic distance separations should be adjusted with weather conditions.

It becomes a bit more complex when we start talking about turbulence. In the atmospheric sciences, turbulence is important because it mixes and churns water vapor, smoke, and other substances, as well as energy, which in effect become distributed. Air turbulence is often quantified with the turbulent energy dissipation rate (EDR), sometimes also called the eddy dissipation rate (Chan 2011; Nastrom and Eaton 1997). The turbulent EDR is a fundamental number to characterize the intensity of turbulence (e.g. Pope 2000). EDR is a measure of the viscous diffusion of turbulent kinetic energy (TKE), which is transformed from large scales to small scales within the inertial subrange via eddies, where eventually viscous effects dominate (Kolmogorov 1941). An advantage of using EDR is that just one single parameter is used to quantify the turbulence intensity. Therefore, models, measurements and other applications can be connected with this single parameter. Using just a single parameter for turbulence intensity can also be seen as a disadvantage, because the underlying assumptions are not always satisfied. The key

assumption made is that the energy spectrum follows the Kolmogorov -5/3 scaling (more details in Chapter 3). In other words, the sampling scale and the total sampling scale of the measurements need to be in the inertial range of the turbulence energy spectrum. The sampling scale is the spatial (or temporal) interval between consecutive measurements, and the total sampling scale is the spatial (or temporal) scale of the combined measurements that is used in an algorithm. In EDR retrieval techniques, these sampling scales are relevant as they represent the spatial scales at which the turbulent kinetic energy is estimated, which is necessary for the estimation of EDR. More about the sampling scales will follow in Chapter 3. The bottom line of estimation of turbulence intensity is that turbulence is a complex phenomenon, which is conveniently quantified - with some assumptions - with a single parameter, the EDR.

Turbulence can be measured from time or space fluctuations of many different atmospheric values, such as temperature, humidity and wind velocity. The Kolmogorov theory applies to the spatial domain. Measurements in the time domain are analyzed by using Taylor's hypothesis of "frozen" turbulence (Taylor 1938), which presupposes that the spatial turbulent fluctuations are advected with the flow. It is easily assumed that the measurements are in the inertial range, but often this is not validated because it requires good data quality with a high sampling rate. Also, the total sampling time/spatial scale of the fluctuations is important in an EDR retrieval technique, as it can be that the total sampling scale is outside the inertial range. The total sampling time/spatial scale is somewhat loosely defined as it can be related to different measurement principles. In the end, EDR can thus be derived from the fluctuations of many different atmospheric variables, with different spatial or time sampling scales, and by using many different instruments, which all affects the quality of the retrieved EDR values. Getting consistency in EDR values from different source can thus be rather tricky.

For many years, EDR values have been derived from in situ measurements. Close to the surface, EDR is typically derived from three-component sonic anemometers and/or fine platinum wire thermometers mounted on towers (e.g. Caughey et al. 1979; Kaimal et al. 1976; Piper and Lundquist 2004; Zhou et al. 1985). At higher altitudes, EDR is estimated from gust-wind-probe systems mounted on aircraft (e.g. Brost et al. 1982; Lemone and Pennell 1979; Nicholls 1978; Nucciarone and Young 1991), or from sonic anemometer carried by balloon-borne sondes (e.g. O'Connor et al. 2010). Next to deriving EDR from velocity or temperature fluctuations, it can be estimated from other atmospheric variables that are indirectly influenced, such as the atmospheric refractive index (e.g. Thiermann and Grassl 1992).

More recently, active remote sensors, such as profiling Doppler radars and lidars, have been used to estimate EDR (Borque et al. 2016; Bryant and Browning 1975; Fang et al. 2014; Kollias and Albrecht 2000; Kollias et al. 2001; O'Connor et al. 2010; Röhner and Träumner 2013; Shupe et al. 2012). Doppler lidars are able to measure air motions below and at the cloud base or in clear-sky conditions (Lamer and Kollias 2015). In the case of clouds, profiling cloud radars can be used to continue profiling of measurements beyond the cloud base. The combination of a

profiling Doppler lidar and a profiling Doppler cloud radar can then, for example, be used to deliver a continuous turbulence intensity profile (Borque et al. 2016). Active remote sensing of EDR has been proven to be valuable, for measurements of clear-sky and clouds, by comparison to independent measurements (O'Connor et al. 2010; Shupe et al. 2012).

In aviation, EDR is used as an indicator for turbulence hazards. For example, EDR can be estimated from vertical accelerations of aircraft, or virtually any device moving through air (MacCready 1964). In recent years, there is an increasing interest to exploit lidar and radar measurements at airports to estimate the EDR. For example at the Hong Kong international airport, operational turbulence monitoring is done by mapping the EDR field with a scanning lidar (Chan 2011). Currently, wake vortex monitoring systems are under development, where EDR has the potential to be used as an input parameter (Barbaresco et al. 2013; Gerz et al. 2005). It is necessary to mention that not only high but also low EDR values are hazardous for aviation. Very light or negligible air turbulence plays an important role as it favors long-lasting wake vortices. Fig. 1.1 illuminates wake vortices that are behind airplanes. When the EDR is accurately measured, it can be used to predict the lifetime of such wake vortices (Holzäpfel 2006). With accurately it is meant that the measurements can indicate areas with strong, moderate and low turbulence intensity, and that the uncertainty of the measurements is well understood.

Figure 1.1: Wake vortices visible in the clouds. Photo credits: Paul Bowen, Cessna Aircraft Company.

1.2. **Weather radar remote sensing**

Remote sensing is defined as the measurement of atmospheric properties and processes at a distance, using radiation sensors placed in space, on aircraft, and/or on the earth's surface (e.g. Petty 2006). To become familiar with this definition, we can recognize the human eyes as a remote sensor (e.g. Mather 2009). The human eyes measure the brightness of surrounding objects by sunlight radiation to sense its environment. Because of the properties of electromagnetic (EM) radiation - both intensity (brightness) and spectral characteristics (color) are strongly influenced by its interactions with matter - it is possible as a human to instantly distinguish objects, faces, textures, material compositions, and many other details (Petty 2006). Next to the human eyes, it is possible to use electronic devices - instruments - for remote sensing.

In the nineteenth century, more forms of EM radiation were discovered beyond the visible part of the spectrum. Other EM radiation forms are interesting to use in remote sensing applications, because they are able to measure different properties of the atmosphere. Radio waves were discovered by Hertz, and in 1863 Maxwell developed an extensive EM theory - now known as the classical theory of electromagnetic radiation - which for the first time explained electricity, magnetism, and light as different manifestations of the same phenomenon. Since the early 1960s, virtually all areas of the atmospheric sciences have been revolutionized by the development and application of remote sensing techniques (Petty 2006). They have been further developed with increasing sensitivity, spatiotemporal resolution, and gaining more versatility in a broad range of applications (Petty 2006; Rees 2012; Richards et al. 2010).

An important remote sensing instrument that was developed in the 20th century is the radar - the word originates from RADAR (RAdio Detection And Ranging). The radar is an object-detection system that uses radio waves to determine the range, angle, characteristics and/or velocity of objects. With respect to visual observation, the radar has some advantages as it is able to operate during day and night, under all weather conditions, and it is capable of observing targets at a large distance. Further developments led to many applications of radar remote sensing systems. These days radars are used for the identification and characterization of aircraft, ships, spacecraft, guided missiles, motor vehicles, weather formations, terrain, and many more (e.g. Rees 2012; Richards et al. 2010).

Radars can be further introduced by looking at some of their features. A radar is characterized by its hardware that includes the radar antenna shape and polarimetric capabilities, and the radar software that includes the signal processing. Some essential parameters for radar are the central frequency, the frequency bandwidth and the antenna dimensions. In the end such parameters result in a maximum unambiguous radar range, the beamwidth, the sampling space area for each radar cell, and an unambiguous velocity that can be estimated for targets. Such essential parameters are carefully selected to optimize a radar for a certain application. Some of the key parameters that can be measured by a radar are the distance of a target towards the radar (target range), the target velocity in the line of sight of the radar antenna and the radar cross section (RCS) of a target. The RCS is a

1

measure of the efficiency of a radar target in intercepting and returning radio energy, which depends upon the size, shape, aspect, and dielectric properties of the target. Interested readers could turn for a more in-depth comprehension of radar instruments to (e.g. Pozar 2009; Richards et al. 2010).

One important radar feature that is extensively used in this work is the measurement of a targets velocity via the Doppler effect. This is done as the frequency of an EM wave is changed with regard to the signal-transmitting instrument, because of the movement of the targets. In the case of a weather radar, which is observing raindrops, the raindrops can change the EM wave frequencies because of the raindrop motions. The frequency shift due to the Doppler effect can thus - in the end after dedicated radar signal processing - be used to remotely estimate parameters for wind dynamics.

A weather radar measures radar observables for each radar cell, which is a space-bounded area defined by a certain range interval and a certain radar antenna looking direction (azimuth and elevation). The exact size of the radar cell is determined by several parameters, which are the radar range resolution, the radar beamwidth in combination with the radar range (distance to the radar). The total sampling space L of a radar cell can be characterized by its volumetric sampling area V via $L = V^{1/3}$. With regards to the dynamics, the weather radar is able to measure the radar mean Doppler velocity, which is a measure of the reflectivity-weighted line-of-sight velocity of the targets. As a consequence, a single big raindrop will have more impact than a small raindrop on the measured radar observables. Also, note that only projected velocities in the radar antenna line of sight are measured, and the velocities from the cross-directions (with regard to the radar antenna line of sight) can not be measured (due to the Doppler frequency shift principles). As we deal with multiple target's in a single resolution volume, the radar can measure the radar Doppler spectral width, which is a measure of the variation of motions of the targets. The measured radar observables are thus never representative for a single raindrop, but they represent an ensemble of raindrops that are distributed in a space-bounded area, and next to that have a certain variation in raindrop sizes.

A few modern remote sensing instruments - which are relevant for this research - are shown in Fig. 1.2. They are: TARA (an S-band precipitation profiling Doppler radar, Heijnen et al. (2000)), IDRA (a scanning n X-band radar, Ventura and Russchenberg (2006)), PARSAX (a scanning S-band radar, Krasnov et al. (2008)), the Thales scanning X-band radar (Barbaresco et al. 2012), and the Leosphere 1.54 μm scanning lidar (Dolfi-Bouteyre et al. 2009). The shared property of these remote sensors is that they can measure wind dynamics with a high resolution. The typical range resolutions of these instruments (IDRA: 30 m, TARA: 30 m, PARSAX: 3 m) are much higher in comparison to a typical weather radar (the WSR-88D has a range-resolution of 250 m, Klazura and Imy (1993)). These instruments differ in many ways, such as the frequency that is being used, the antenna looking direction (horizontal/vertical/slanted/scanning), and the signal processing. The IDRA and TARA radars are located at a meteorological supersite in Cabauw (Ulden and Wieringa 1996), which makes their data interesting for research purposes as it can be validated with in situ data from co-located instruments. They have been op-

erating at this site for many years, which asserts that there are interesting study cases and that there is sufficient data for statistical analysis. The Leosphere 1.54 μm scanning lidar is the exception in Fig. 1.2: it uses ultraviolet radiation instead of radio waves.

(a) TARA   (b) IDRA   (c) PARSAX

(d) Thales X-band radar   (e) Leosphere 1.54 μm scanning lidar
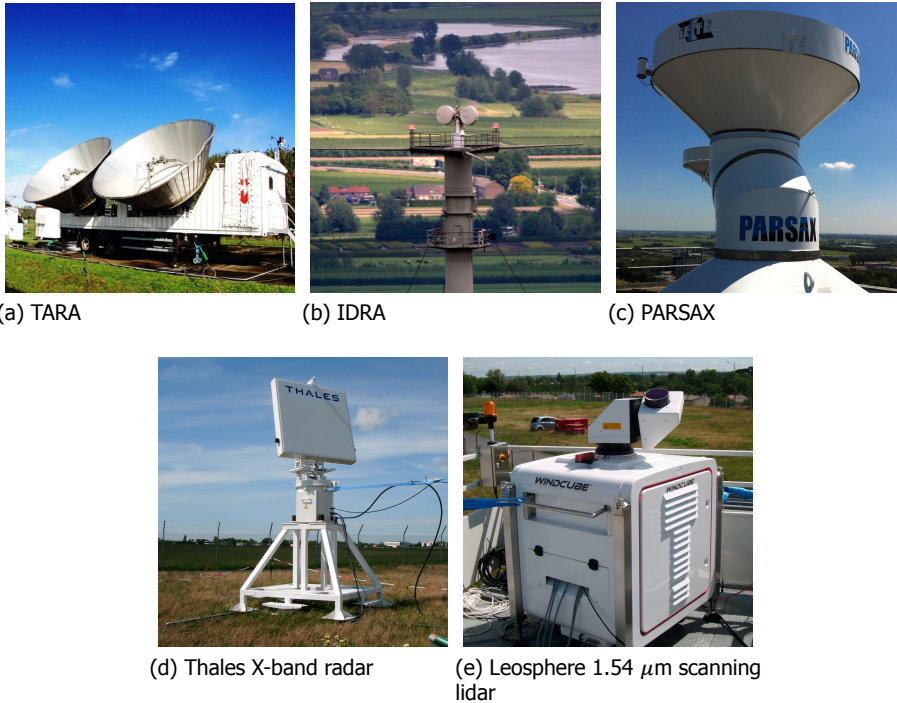
Figure 1.2: A few modern atmospheric remote sensing instruments, which can be used to remotely measure wind dynamics: (a) TARA, the TU Delft S-band precipitation profiling radar (Heijnen et al. 2000), (b) IDRA, the TU Delft X-band IRCTR Drizzle RAdar (Figueras i Ventura 2009), (c) PARSAX, the TU Delft S-Band PARSAX radar system (Krasnov et al. 2008), (d) the Thales scanning X-band radar (Barbaresco et al. 2012), and (e) the Leosphere 1.54 μm scanning lidar (Dolfi-Bouteyre et al. 2009). TARA photo credits: Tim Vlemix. IDRA photo credits: Jordi Figueras i Ventura.

The lidar measures the backscatter from aerosols, which allows measurements during clear-sky conditions. For the radar, the aerosols typically do not reflect sufficiently to be detected, and other targets such as snow, raindrops, cloud drops or insects are required to measure the properties of the atmosphere. Radars and lidars have the ability to work operationally in a complementary way in different weather conditions like fog, precipitation and dry air. For the observation of air motion, both instruments are relying on the backscatter of particles, which randomly fill the observation volume and are involved in air motion. Typical backscatterers for radar are rain/cloud drops and ice crystals, and aerosols for lidar. Different scattering and attenuation mechanisms of light/infrared waves for lidars and of microwaves for radars result in the fact that a lidar is able to retrieve the EDR remotely during

1

clear sky conditions, and a radar is able to do the same in presence of clouds or precipitation (Bringi and Chandrasekar 2001; Doviak and Zrnić 1993; Mishchenko et al. 2002).

1.3. Raindrop backscattering

With regard to radar-based retrieval of air-dynamics parameters, often the assumption is made that the motion of air is measured, where in reality the motion of the tracers is measured. For the weather radar, raindrops are the most common backscatters of which the motion is measured. Because of the much higher mass density of raindrops in comparison to the surrounding air (approximately a factor 1000), the raindrops do not follow the motion of the air perfectly. This is due to the inertia effect, and in this work we will refer to it as "the raindrop inertia effect". The raindrop inertia effect is typically not taken into account in retrieval techniques for wind vector or turbulence intensity estimation. An unanswered research question is:

- Is the raindrop inertia effect of the same importance for classical weather radars (typical total sampling scale for a radar cell of 250 m) as modern high-resolution radars (30 m)?

It is thus unclear when - and exactly under what circumstances - the raindrop inertia effect is important in radar-based wind vector and turbulence intensity retrieval techniques.

As a result, for an accurate estimation of wind vectors and turbulence intensities from raindrop-backscattering radar Doppler measurements, the peculiarities of using raindrops as tracers has to be considered. It is expected that the size of the raindrops will be of importance, and also the scales of turbulent eddies and the sampling scales of the measurement. A model to take the raindrop inertia effect into account for radar-based turbulence intensity retrieval techniques was proposed by Yanovsky et al. (2005), where a raindrop is either a perfect tracer of the turbulent motion, or not involved in the turbulent motions at all for a given turbulent length scale and an equivolumetric raindrop size. A drawback of the model from Yanovsky is that it has heuristic parameters, which are difficult to estimate, and make it difficult - if not impossible - to develop this model further. The challenge is thus to measure wind vectors and/or EDR with a Doppler radar during rain, and take into account that raindrops are not perfect tracers of the air motion.

In the state-of-the-art literature, turbulence is typically modeled in radar observables as an additional Doppler spectrum width term, or by smoothening and widening the spectrum via a convolution process (Borque et al. 2016; Bouniol et al. 2004; Doviak and Zrnić 1993; Kollias and Albrecht 2000; Shupe et al. 2012). There has been done only little research to challenge these state-of-the-art approaches, and in addition, for radar-based turbulence intensity retrieval techniques the influence of inertia is often ignored. Two research questions are then:

1. Does the turbulence intensity have an effect on the ensemble of orientations of the scatterers (raindrops)?

2. And can there - as a consequence - exist a dependence between polarimetric radar observables (Z_{dr}, L_{dr}) and turbulence intensity?

These points are not considered in the literature with regard to radar-based turbulence intensity retrieval techniques to our knowledge. It is not difficult to imagine that the ensemble distribution of particle orientations will be different for calm and turbulent conditions. There is thus clearly room for some improvement in radar-based turbulence intensity retrieval techniques, and potentially the polarimetric radar observables can be used in a better way.

1.4. Research challenges of the dissertation

This research is dedicated to the development of radar-based retrieval techniques that are used to retrieve air-dynamics parameters remotely during rain, but then more accurately. The key research challenges in this work are:

- Examine under what circumstances the raindrop inertia is of importance for radar-based turbulence intensity retrieval techniques. And more specifically, investigate if EDR can be derived accurately from the radar Doppler spectral width from a modern radar with a much higher spatial resolution than the classical weather radars.

- Find out if existing retrieval techniques for wind vector and turbulence intensity fields are accurate in the case that they are applied to radar-based Doppler measurements during the rain. And if so, verify this by comparisons to other measurements.

- Investigate if radar-based wind velocity field retrieval techniques can be further enhanced. In particular, study how a 3D wind vector can be reconstructed from Doppler radar line-of-sight velocity measurements.

- Explore how retrieval techniques for wind vector and EDR fields can be further adapted to the radar and enhanced with respect to the current state-of-the-art. More specifically, study if polarimetric radar observables can be used to enhance radar-based EDR retrieval techniques.

The novelties in this research are to take into account the influence of measuring air-dynamics parameters from imperfect air tracers (read: raindrops), and the usage of significantly smaller spatial sampling scales that are achieved with modern research (and some operational) weather radars. The approach to resolve these challenges is by analysis of radar measurements from these modern radars, and develop new radar-based turbulence models, which will be explained in detail in the following chapters.

1.5. Research approaches and outline of the dissertation

The research questions above are addressed in the thesis chapters in the following way:

1

Chapter 2 investigates the theory of turbulence intensity measurements from raindrop motions. The equations of motion for a raindrop are used as a starting point, from which raindrop inertial parameters are estimated. These raindrop inertial parameters, which now have a theoretical basis as they come from the equations of motion, have the potential to be used in turbulence retrieval techniques and make such techniques more accurate. To achieve this, a raindrop-inertia-correction model is proposed, to enhance radar-based turbulence intensity retrieval techniques. With turbulence simulations and using the equation of motion for a raindrop, the effectiveness of the proposed correction model is investigated.

Chapter 3 assesses energy dissipation rate (EDR) retrieval techniques, based on air-velocity measurements. A few state-of-the-art EDR retrieval techniques are applied to raindrop-backscattering radar Doppler measurements, without a correction for raindrop inertia. The research question that is addressed here is: Does the choice for a specific retrieval technique, and the chosen parameters, influence the accuracy on the retrieved EDR when applied to the Doppler radar during rain? The chosen parameters consist of using Doppler spectral width or a series of mean Doppler velocities, and the associated sampling and total sampling scale in the retrieval techniques. Consequently, the techniques are optimized, such that they can be used for radar-based EDR estimation during rain. The radar-retrieved EDR values are then compared to in situ measurements of EDR for validation. This comparison is then repeated for a massive dataset, to support conclusions that are valid for a wide variety of atmospheric conditions in the midlatitudes and a variety of EDR values.

Chapter 4 starts with an assessment of the influence of raindrop inertia on raindrop-backscattering radar-based retrieved wind vectors. A novel 4D-Var wind vector retrieval technique is introduced, which is applied to measurements from a single scanning Doppler radar. Advanced processing features, which are only possible with this technique, are then demonstrated with a case study. A comparison for the resulting wind vectors is made with the linear wind model, which is a commonly used wind vector retrieval technique (e.g. Doviak and Zrnić 1993). The retrieved wind vectors will be analyzed in detail, to assess which retrieval techniques provide the most realistic results.

Chapter 5 presents an advanced approach on turbulence estimation, where the influence of raindrop inertia is taken into account. The emphasis here is to apply turbulence intensity retrieval techniques to small spatial scales of modern research radars. For such small spatial scales, the DSD characteristics, the influence of raindrop inertia and turbulence effects are mixed in the radar observables, and the challenge is to disentangle this information. Therefore, a radar forward model is developed that can handle this, which takes turbulence into account, and - as a novelty - includes particle orientations as a function of turbulence intensity. A radar forward model is a procedure that calculates radar observables, e.g. radar reflectivity Z, starting from physical model variables, such as DSD. Once the radar forward model is there, differences between the radar measurements and simulated data are used in an optimal estimation procedure, to estimate the model parameters. Simulations are performed to justify the novel implementation of turbulence

in radar forward models. In a case study, turbulence intensity profiles are retrieved from the TARA Doppler radar data, for which the raindrop-inertia-correction model will be demonstrated.

Chapter 6 demonstrates the application of wind vector and turbulence intensity retrieval techniques at an airport for a fast scanning X-band radar. It will be studied which retrieval techniques, both for wind vectors and EDR, give the most reliable results when applied to an X-band radar during rain.

Chapter 7 contains the conclusions of this dissertation and presents an outlook on future research and applications.

1

2

The raindrop inertia effect

In this chapter, the focus is on how to account for the influence of raindrop inertia in radar-based turbulence intensity retrieval techniques, with a theoretical approach. Raindrop inertial parameters are derived from the equations of motion of a raindrop, which contain the relevant physical forces that are acting on a raindrop. The inertial distance is introduced, which is a typical distance at which a particle obtains the same wind velocity as its surroundings throughout its trajectory. Consequently, a new model for raindrop-inertia correction is proposed, which is able to obtain the variance of mean Doppler velocities as if there was no influence of raindrops. Such a model is necessary for radar-based estimation of turbulence intensity during rain. Two effects are taken into account into the new inertia-correction model. At first, the effect that inertial particles are less involved in wind velocity fluctuations due to their mass, which results in a decrease in the variance of measured mean Doppler velocities. Secondly, the effect that the velocity of an inertial particle is influenced by the history of its trajectory. For an ensemble of particles, this can lead to an increase in the variance of measured mean Doppler velocities. Theoretical simulations are performed to validate the proposed model and to obtain some essential tuning parameters. Finally the conclusions are drawn. It is in particular interesting to discover under which conditions (read: sampling scales and raindrop sizes) the influence of raindrop inertia is relevant, and under which conditions the influence of raindrop inertia can be neglected.

"I have never tried that before, so I think I should definitely be able to do that."
- Astrid Lindgren, Pippi Longstocking.

2

2.1. Introduction

An accurate estimation and validation of turbulence intensity during precipitation by using the radar has not received a lot of attention in the last years. A common approach to derive the energy dissipation rage (EDR) is to apply an analytical formula to the radar Doppler spectral width (DSW) or the variance of mean radar Doppler velocities (e.g. Bohne 1982; Frisch and Strauch 1976; Hocking 1986; Shupe et al. 2012; Yanovsky et al. 2002). Such a formula does not take the raindrop size distribution (DSD) into account. In recent years, the radar-based estimation of the rainfall rate has been improved by making use of a simultaneous retrieval of the rain DSD for radars with a low elevation angle (e.g. Brandes et al. 2003). Also, a retrieval technique from a slant looking radar has been developed to retrieve the DSD (Unal 2015).

The rain DSD is an essential input to radar-based EDR retrieval techniques to improve the accuracy of the resulting turbulence intensity (e.g. Yanovsky et al. 2005). The rain DSD parameters can, for example, be estimated from polarimetric parameters (e.g. Brandes et al. 2004; Yanovsky et al. 2015), but there are also other techniques. In spite of essential progress achieved, EDR retrieval techniques are nowadays not accurate enough for many applications. One point of concern is the impact of the inertia effect when Doppler radar measurements during rain are used for turbulence intensity estimation. This point is investigated in this chapter, theoretically and by performing simulations.

One of the most difficult issues related to accurate retrieval of EDR from the scattered signal is taking into account the inertia of the scatterers. Actually, the echo-signal is scattered from particles that are located in the resolution volume and not from the turbulence itself. Some early works suppose that the scatterers are able to follow turbulent eddies perfectly (e.g. Doviak et al. 1979). This is true for very small particles such as aerosols that are relevant for the lidar, it is almost true for dry snowflakes (e.g. Rogers and Tripp 1964), but it is rather doubtful for raindrops. It is rather obvious that larger droplets are less effective as the tracers of the air motion; but how to estimate this quantitatively? And how to use it in radar models to improve the results of turbulence intensity retrieval?

To answer some of these questions, an approach was developed by Yanovsky (1996), which was further applied in follow-up articles (Yanovsky et al. 2005; Yanovsky 2002). The approach of Yanovsky (1996) takes into account that atmospheric turbulence is a complex vortical motion with a spectrum of spatial scales of eddies. In other words, the air motions with larger scales have more energy for the same EDR value. The authors introduce a bounded deterministic function, which describes the relation between the drop size diameter D and the level of involvement of the droplet for a given turbulence-motion size. This approach is based on four presuppositions: 1) For each drop size there is a minimum length scale L_{min}; 2) For turbulent motions larger than L_{min} the drop is a perfect tracer; 3) For turbulent motions smaller than L_{min} the drop will not participate in the motion; 4) For $L_{min} = f(D)$, an approximation was introduced based on estimations of the droplet relaxation times. The approach of Yanovsky (1996) is based on heuristic suppositions that are rather flexible and allows adaption of the model to a real situation. Nevertheless,

it is much better to have an algorithm based on more fundamental physics, and the equations of motion for a raindrop seem to be a good starting point. In this chapter, we reuse existing theoretical and experimentally validated work in which the equations for raindrop motion, including the relevant constants, are derived (Khvorostyanov and Curry 2005). Based on these equations we estimate raindrop inertial parameters.

The chapter is structured as follows. In the second section we derive particle inertial parameters from the equations of motion. In the third section, a new model to account for the influence of raindrop inertia is described. In the fourth section tuning parameters of the model are obtained by using a stochastic 3-D homogeneous isotropic turbulence model. In the fifth section, mathematical relations are given that show how the model for inertia correction can be implemented in a radar retrieval technique. In the end, the conclusions are drawn.

2.2. **Raindrop inertial parameters**

In this section, the aim is to find raindrop inertial parameters, which quantify how much a particle behaves as a perfect tracer. Or alternatively speaking, how much a scatterer responds to fluctuations in wind velocities throughout its trajectory. To obtain raindrop inertial parameters that can be used in radar-based retrieval techniques for the estimation of the energy dissipation rate (EDR) from the DSW, it is logical to start from the equations of motion for a raindrop. However, a problem is that the equations of motion can not be applied directly in a turbulence intensity retrieval technique, because only limited information (read: not the motion of all particles at each location and time) is available from measurements.

To follow the approach of starting from the equations of motion for a raindrop, it is necessary to simplify these equations down to scalars, the inertial parameters, that represent the behavior of an ensemble of particles. An advantage of this approach is that it is possible to verify all model assumptions with simulations, and better adapt this approach to specific applications. In addition, the same procedure can be applied to other classes of hydrometeors such as ice crystals.

Works with such a fundamental approach already exist but with a different aim. Khvorostyanov and Curry (2005) started from the equations of motion for raindrop/ice particles and successfully estimated their terminal fall speeds. One of the most difficult parts in such works is the determination of the drag force coefficient for raindrops or ice particles. Here we reuse this existing work from Khvorostyanov and Curry (2005), but now with the aim of estimating inertial parameters instead of the terminal fall speed.

The equations of motion using a Cartesian East North Up (ENU) coordinate system for a particle in the x/y-direction and the z-direction can be written as:

$$\frac{dv_{p,xy}}{dt} = \frac{\pm F_{d,xy}}{m} = \mp \eta_{xy}(v_{a,xy} - v_{p,xy})^2, \tag{2.1}$$

$$\frac{dv_{p,z}}{dt} = \frac{-F_g + F_b \pm F_{d,z}}{m} = -\eta_z v_t^2 \mp \eta_z(v_{a,z} - v_{p,z})^2, \tag{2.2}$$

with

$$\eta_{xy} = \frac{\rho_F A_{xy} C_{d,xy}}{2m} \quad , \quad \eta_z = \frac{\rho_F A_z C_{d,z}}{2m}, \tag{2.3}$$

where $v_{p,*}$ is the particle velocity, $v_{a,*}$ is the air velocity, v_t is the terminal particle fall speed, $F_{d,*} = \frac{1}{2}\rho_F A_* C_{d,*}(v_{a,*} - v_{p,*})^2$ is the drag force, ρ_F is the air density, A_* is the projected particle surface area in direction *, $C_{d,*}$ is the drag force coefficient, $F_g = mg$ is the gravity, m is the particle mass, g is the gravitational acceleration, $F_b = \rho_F V_b g$ is the buoyancy force, and V_b is the volume of the particle. Here η_z [m^{-1}] and η_{xy} [m^{-1}] are scalars to write the equations of motion in a brief way. The x and y directions have the same equation and are for convenience combined.

The calculations for the drag force coefficients $C_{d,*}$ are extensive and can be obtained from the work of Khvorostyanov and Curry (2005). For raindrops in the air, the buoyancy force can be neglected, as the gravitational force is much larger (Khvorostyanov and Curry 2005). However, for crystallized ice particles, which can have much lower volumetric mass densities, the buoyancy force should also be considered. The direction of the drag force is opposite to the particle motion with respect to its surrounding air motion, which determines the right sign in the equations. For the remainder of this chapter the terminal fall velocities and scalars η_{xy} and η_z are obtained from the work of Khvorostyanov and Curry (2005).

As big raindrops have a spheroidal shape, also an axis ratio formula as a function of equivolumetric spherical drop diameter is used from Beard and Chuang (1987).

The raindrop terminal fall speed is obtained by assuming a balance between the gravitational, drag and buoyancy forces (Khvorostyanov and Curry 2005):

$$v_t(D) = \left[\frac{2(|mg - F_b|)}{\rho_F A_z C_{D,z}}\right]^{1/2}, \tag{2.4}$$

where D is the equivolumetric spherical drop diameter. Almost all variables on the right-hand side depend on D, except for ρ_F and g.

The total particle velocity $\vec{v}_p$ is written conveniently as:

$$\vec{v}_p = \vec{v}_t + \vec{v}_a + \vec{v}_p', \tag{2.5}$$

where $\vec{v}_t$ is the particle terminal fall velocity, $\vec{v}_a$ is the air velocity, and $\vec{v}_p'$ the additional velocity difference due to relaxation. The direction of the terminal fall velocity is always in the negative z-direction, pointing towards the Earth. The direction and magnitude of $\vec{v}_p'$ are obtained by numerically integrating the equations of motion, Eq. 2.1 and 2.2. The relaxation term $\vec{v}_p'$ contains thus some history of what the particle has experienced from the surrounding wind field throughout its trajectory.

With analytical solutions to the equations of motion for simple cases, it is then possible to estimate typical numbers that characterize the motion of an ensemble of particles. One of such simple cases is a sudden jump in velocity, from which a relaxation time can be estimated. For the x/y-direction, the 'sudden jump' case is formulated as:

$$v_{a,xy}(t) = \begin{cases} v_{a,xy}(-\infty) & \text{for } t < 0 \\ v_{a,xy}(\infty) & \text{for } t \geq 0 \end{cases}, \tag{2.6}$$

i.e. a step function at $t = 0$, for which the solution for the particle velocity at $t > 0$ is:

$$v_{p,xy}(t) = v_{a,xy}(\infty) + \frac{1}{1/[v_{a,xy}(-\infty) - v_{a,xy}(\infty)] - \eta_{xy}t}. \tag{2.7}$$

From the analysis of the 'sudden jump' case, we can obtain the relaxation time for the x/y-direction $\tau_{I,xy}$. It is defined as the time that is needed to decrease the relative difference in velocity with $exp(1)$:

$$\frac{v_{p,xy}(t) - v_{a,xy}(\infty)}{v_{a,xy}(-\infty) - v_{a,xy}(\infty)} = \exp(-1), \tag{2.8}$$

from which follows:

$$\tau_{I,xy} = \frac{1 - \exp(-1)}{\exp(-1)\eta_{xy}[v_{a,xy}(\infty) - v_{a,xy}(-\infty)]}. \tag{2.9}$$

This calculated relaxation time is then used as inertial time. It should be mentioned that such an inertial time is only a figure of merit, and the reality is that wind fields are more complex.

For the z-direction, no analytical solution is found yet for the general 'sudden jump' case. It is, however, possible to find analytical solutions for more specific cases, where the terminal fall speed is large or small, compared to the order of magnitude of velocity differences due to relaxation $\mathcal{O}(v_p')$. For the first case, a small terminal fall speed is assumed. With this assumption, i.e. $v_t \ll \mathcal{O}(v_p')$, it is possible to neglect some terms in Eq. 2.2, and the solution becomes similar for the x/y-direction. The relaxation time $\tau_{I,z1}$ is then:

$$\tau_{I,z1} = \frac{1 - \exp(-1)}{\exp(-1)\eta_z[v_{a,z}(\infty) - v_{a,z}(-\infty)]}. \tag{2.10}$$

In case the terminal fall speed is large, i.e. $v_t \gg \mathcal{O}(v_p')$, also some terms can be neglected, and the equation of motion for the z-direction is written as:

$$\frac{dv_{p,z}}{dt} = \frac{dv_{p,z}'}{dt} \approx \mp 2\eta_z v_t v_{p,z}' = \mp \frac{v_{p,z}'}{\tau_{I,z2}}, \tag{2.11}$$

with:

$$\tau_{I,z2} = \frac{1}{2\eta_z v_t}, \tag{2.12}$$

where $\tau_{I,z2}$ is the relaxation time for the z-direction. Again, the sign is such that the relaxation velocity, $v_{p,z}'$, is reduced, e.g. negative derivative, $\frac{dv_{p,z}'}{dt}$, when $v_{p,z}'$ is positive. For the 'sudden jump' case, the analytical solution is:

$$v_{p,z}(t) = \qquad -v_t + v_{a,z}(\infty)$$
$$+[v_{a,z}(-\infty) - v_{a,z}(\infty)]\exp(-\frac{t}{\tau_{I,z2}}). \tag{2.13}$$

direction	Inertial time	Inertial distance
x/y	$\tau_{I,xy} = \dfrac{1 - \exp(-1)}{\exp(-1)\eta_{xy}[v_{a,xy}(\infty) - v_{a,xy}(-\infty)]}$	$d_{I,xy} \approx \dfrac{1 - \exp(-1)}{\exp(-1)\eta_{xy}}$
z, $v_t \ll \mathcal{O}(v_p')$	$\tau_{I,z1} = \dfrac{1 - \exp(-1)}{\exp(-1)\eta_z[v_{a,z}(\infty) - v_{a,z}(-\infty)]}$	$d_{I,z1} \approx \dfrac{1 - \exp(-1)}{\exp(-1)\eta_z}$
z, $v_t \gg \mathcal{O}(v_p')$	$\tau_{I,z2} = \dfrac{1}{2\eta_z v_t}$	$d_{I,z2} \approx \dfrac{1}{2\eta_z}$

Table 2.1: Inertial parameters for raindrops.

Given the inertial times, it is now also possible to approximate the inertial distances, by assuming that the particles are moving with the terminal fall speed in the z-direction for $v_t \gg \mathcal{O}(v_p')$, or otherwise moving with the final speed $v_{a,z}(\infty) - v_{a,z}(-\infty)$. An overview of all the inertial distances and inertial times for raindrops that are defined in this chapter are given in Tab. 2.1.
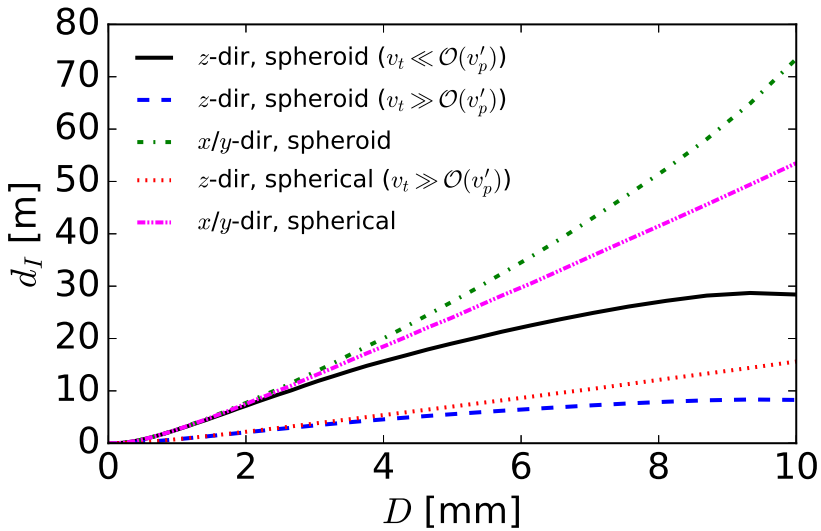
Figure 2.1: The inertial distance d_I for raindrops is plotted as a function of drop equivolumetric diameter D. The calculations are performed both for spherical and spheroid droplets, for which the axis ratio relation from Beard and Chuang (1987) is used. Note that 'z-dir, spherical, $v_t \ll \mathcal{O}(v_p')$' is not in the figure because it is the same solution as 'x/y-dir, spherical.'.

Calculated values for the inertial distance are shown in Fig. 2.1. The inertial distance is increasing rapidly with the drop size. For large terminal fall speeds, $v_t \gg \mathcal{O}(v_p')$, the inertial parameters are reduced. In Fig. 2.1 the calculated inertial parameters are also calculated for spherical drops, which shows that the spheroidal shape only has a minor impact.

From the equations of motion for a raindrop, inertial parameters have now been estimated by making several assumptions. Without any additional information, the

derived inertial parameters give a best guess for the time (distance), that a particle needs to respond to a change in the wind field. These assumptions include the simplification of the equations of motion to analytical solutions to the 'sudden jump' case. The analytical solutions are different for direction, either x/y or z, and in case of the z-direction the solutions deviate for relatively large or small terminal fall speeds. An additional assumption is made that the raindrops maintain their shape, which means that microphysics (evaporation/condensation) and vibrations are not considered. Such simplifications are rather crude, but they are necessary as a first step in the development of enhanced turbulence retrieval techniques that account for the raindrop inertia effect.

2.3. A new model for raindrop-inertia correction

Here we propose a new way on how to account for the inertia of raindrops, which can be used for modeling of radar observables such as the radar Doppler spectrum or the radar Doppler spectral width. The proposed method provides a correction for the observed variance of Doppler velocities, given the equivolumetric drop size, or drop size distribution, and the observed radar resolution volume parameters.

In the case of homogeneous isotropic turbulence, the Kolmogorov hypothesis (Kolmogorov 1991) states that, within the inertial subrange, the statistical representation of the turbulent energy spectrum of air velocities $S(k)$ is given by:

$$S(k) = C\epsilon^{2/3}k^{-5/3}, \tag{2.14}$$

where C is a Kolmogorov constant, and ϵ is the energy dissipation rate. The wavenumber k is related to a length scale L via $k = 2\pi/L$. The variance of velocities, σ^2, is then obtained as:

$$\sigma^2 = \int_{k_{min}}^{k_{max}} S(k)dk = \frac{3}{2}C\epsilon^{2/3}[k_{min}^{-2/3} - k_{max}^{-2/3}]. \tag{2.15}$$

The variance of velocities σ^2 is thus proportional to the length scales:

$$\sigma^2 \propto [L_{max}^{2/3} - L_{min}^{2/3}]. \tag{2.16}$$

A correction ζ to the variance due to turbulence intensity, Eq. 2.16, is now defined, which can be directly applied to the radar Doppler spectral width:

$$\zeta = \sigma_{inertia}/\sigma_{no,inertia} , \tag{2.17}$$

where $\sigma_{inertia}$ is the standard deviation of velocities for the inertial particles, and $\sigma_{no,inertia}$ is the standard deviation of velocities as if there was no inertia.

Typically, in a radar-based turbulence intensity retrieval technique $\sigma_{inertia}$ is measured and one would like to have $\sigma_{no,inertia}$, which can be directly related to the turbulence intensity. The term $\sigma_{no,inertia}$ is related to perfect tracers of the air, as if the radar was looking to particles that were following the air motion exactly.

A new inertia-correction model is proposed by making a correction to the scales L_{max} and L_{min} to account for the influence of raindrop inertia. This is achieved by

filling in Eq. 2.16 two times in Eq. 2.17. Both the maximum and the minimum scale for which the inertial particles are sensors are adjusted, based on the derived inertial parameters (Tab. 2.1). The maximal scale is adjusted, as an ensemble of inertial particles can have more variations of velocities that are representative for a larger volume than the total volumetric scale at which is measured. To do this, a typical distance is defined, $d_{I,xyz}$, which is a 3-D distance on which the particle responds to variations in the wind field. On the other side, the minimal scale is adjusted because the inertial particles need a certain distance to respond to variations in the wind velocity.

The inertia-correction model is then formulated as:

$$d_{I,xyz} = \sqrt{2 * d_{I,xy}^2 + d_{I,z2}^2}, \tag{2.18}$$

$$\zeta_{xy}^2(L_{xy}, D) = \frac{(L_{xy} + \alpha_{xy} d_{I,xyz})^{2/3} - (\beta_{xy} d_{I,xy})^{2/3}}{L_{xy}^{2/3}}, \tag{2.19}$$

$$\zeta_z^2(L_z, D) = \frac{(L_z + \alpha_z d_{I,xyz})^{2/3} - (\beta_z d_{I,z2})^{2/3}}{L_z^{2/3}}, \tag{2.20}$$

where L_* is the radar resolution volume scale for direction * and $d_{I,xyz}$ is 3-D inertial distance. Here we introduce α_* and β_*, which are dimensionless tuning parameters, that can be used to adapt this model, based on additional information such as simulations or experiments. Note that for $(\alpha_* = 0, \beta_* = 0)$ the result is that $\zeta = 1$ and there is no correction. The maximal scale is adjusted with the 3-D inertial distance, because the variance in the x- or y-component velocities is enlarged due to sensing of velocities over more space than just the sampling space due to the slow adaptation of the velocity of a particle to its expected velocity (terminal velocity + air velocity). The minimal distance is only adjusted with the 1-D inertial distance, because this idea fits the best with the analyzed "sudden jump" cases. Here we choose $d_{I,z2}$, i.e. the solution for $v_t \gg \mathcal{O}(v_p')$, which is valid for small turbulence intensities in precipitation. The alternative, $d_{I,z1}$, has a similar dependency on D, which is shown in Fig. 2.1.

Some choices in this model may be considered as rather crude, and they have the potential to be further developed. At this stage the concept is that the estimated tuning values for α_* and β_* should be able to cover for the model impurities. The uncertainties of these tuning values will give an impression of how good the model works.

In Fig. 2.2, the model for inertia correction is shown for different tuning parameters α_* and β_* for a drop of 0.5 mm which demonstrates both effects. The parameter α_* determines the importance of the correction for large scales. In Fig. 2.2, it is shown that an increased value of α_* leads to an increased value of $\sigma_{inertia}$, which can be attributed to the 'transport of velocity fluctuations' into the sampling space. The parameter β_* determines the relative importance of the classical inertia effect, i.e. the limited response to the small-scale velocity fluctuations. In Fig. 2.2, it is shown that an increased value of β_* leads to a decrease in the value of $\sigma_{inertia}$, which can be interpreted as little (/no) response of inertial particles to small-scale fluctuations.
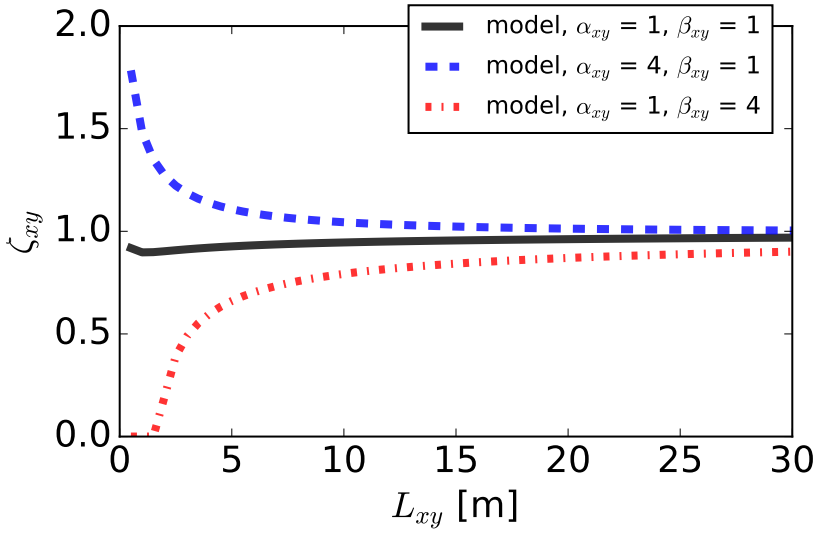
(a) D = 0.5 mm, x/y-direction
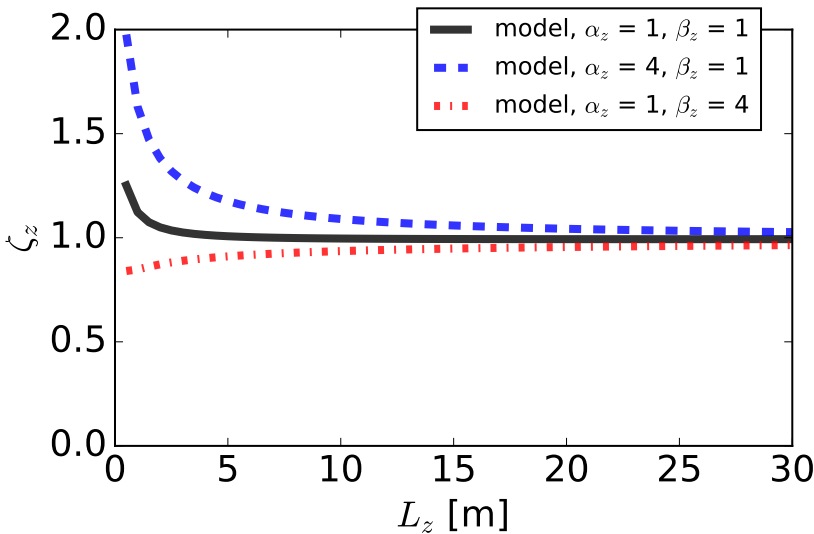
(b) D = 0.5 mm, z-direction

Figure 2.2: The inertia correction ζ_* is plotted as a function of the observation length scale L_* for the direction $*$, which is x/y or z for a droplet with a diameter of $D = 0.5$ mm. The plots are for different tuning parameters α_* and β_*.

For reference, we also give here the correction for any radar line of sight (LOS), which can be relevant for further applications. Given the radar antenna elevation looking angle θ, this is:

$$
\begin{aligned}
\zeta^2(L_{xy}, L_z, D, \theta) =\ & \cos^2(\theta)\zeta_{xy}^2(L_{xy}, D) \\
& + \sin^2(\theta)\zeta_z^2(L_z, D).
\end{aligned} \tag{2.21}
$$

2.4. Simulations of raindrop inertia

In this section, it is shown how wind field simulations can be used to adapt the model for inertia correction. A 3-D homogeneous isotropic turbulence model from Mann (1998) is used to estimate the tuning parameters α_* and β_* in the inertia-correction model (Eq. 2.19 and 2.20). The simulated wind field and the terminal fall speed of droplets are used to calculate backward trajectories of raindrops. Given the backward trajectories, the additional velocity differences due to relaxation are then calculated, by implicit integration of the equations of motion (Eqs. 2.1 and 2.2). The additional velocity differences due to relaxation, i.e. the inertia effect, are then used to estimate the difference in variance of Doppler velocities, within a radar resolution volume. The result of the simulations will also give an estimate for the uncertainties due to the raindrop inertia effect for EDR estimation from the Doppler spectral width.

Here we use the work of Mann (1998) to obtain a 3-D homogeneous isotropic turbulence periodic field with spatial scales of 30 x 30 x 30 m^3, a spatial resolution of 1.2 m and an EDR of 0.01 m^2 s^{-3}, which is a typical value of daytime atmospheric EDR. The scale of 30 m is chosen because this is a typical maximum distance where inertia becomes less important (see Fig. 2.1). The parameters in the wind field simulation are chosen in such a way that the simulated wind field satisfies the Kolmogorov energy spectrum for the inertial subrange (Eq. 2.14). Details of such simulations can be found in Mann (1998). The simulated wind fields are shown in the background of Fig. 2.3. Given the terminal particle velocity, the wind field and the assumption of no inertia, $\vec{v}_p' = 0$ in Eq. 2.5, the backward trajectories of particles are then calculated. In Fig. 2.3 it is shown that for small raindrops (0.01 and 0.1 mm) the trajectories and the origins have a random nature. For larger raindrops (0.5 and 4 mm) the trajectories have an orchestrated nature and the drops mainly originate from above.

To estimate the effect of inertia on the radar Doppler spectral width, the following method is applied. On a line, either parallel to the x-direction or the z-direction, at a random position in the simulation, 100 equidistant points are taken, for which the radar Doppler velocities are calculated (see Fig. 2.3 for some examples). For the Doppler velocities the projected velocities in the radar LOS are taken, e.g. u for the x-direction. Consequently, the standard deviations of the Doppler velocities are calculated two times, with and without the velocity difference due to relaxation $v_{p,*}'$. The standard deviations of LOS velocities are then used to calculate the inertia factor $\zeta_{*,i}$ for direction $*$, which is specific for the realization of this wind field and specific for the random location of the line that spans 100 equidistant drop locations

(a) D = 0.01 mm

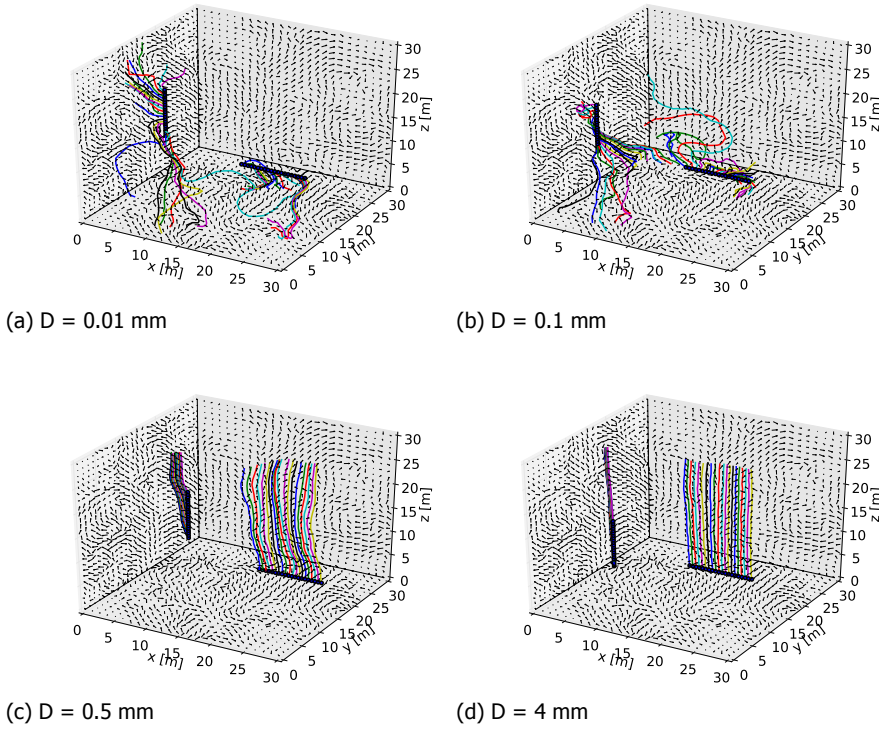(b) D = 0.1 mm

(c) D = 0.5 mm

(d) D = 4 mm

Figure 2.3: Backward trajectories of raindrops are shown for different equivolumetric drop sizes D for the same 3-D wind field. The black dots represent the final locations of the drops, which are used in the simulations. In the background, wind vectors are shown on the xy, xz and yz-planes of a 3-D wind field simulation (Mann 1998).

for simulation number i:

$$\zeta_{*,i} = \sigma_{*,i,inertia}/\sigma_{*,i,no,inertia} , \qquad (2.22)$$

where $\sigma_{inertia}$ is the standard deviation of LOS velocities with $v'_{p,*}$ included. For $\sigma_{no,inertia}$ the relaxation term $v'_{p,*}$ is not included. An ensemble of such calculations are then used to calculate optimal tuning parameters in the model for inertia correction, and to estimate the uncertainty due to raindrop inertia effect in EDR estimation from the Doppler spectral width.

For the estimation of the inertia factor $\zeta_{*,i}$, the velocity difference due to relaxation $v'_{p,*}$ has to be calculated. First a backward trajectory is calculated, under the assumption that $v'_{p,*}$ is not too large and has a negligible influence on the trajectory. An advantage of this assumption is that the final position is not altered. See Fig. 2.3 for some examples of backward trajectories.

Consequently, the equations of motion are integrated over the trajectory to find

the particle velocity difference due to relaxation $v'_{p,*}$. To do this, first the equations of motion, Eqs. 2.1 and 2.2, are rewritten in terms of the relaxation term $v'_{p,*}$:

$$\frac{dv'_{p,xy}}{dt} = \begin{cases} +\eta_{xy}v'^2_{p,xy} & \text{for } v'_{p,xy} < 0 \\ -\eta_{xy}v'^2_{p,xy} & \text{for } v'_{p,xy} > 0 \end{cases}, \tag{2.23}$$

$$\frac{dv'_{p,z}}{dt} = \begin{cases} +\eta_z\left[v'^2_{p,z} - 2v_t v'_{p,z}\right] & \text{for } v'_{p,z} < 0 \\ -\eta_z\left[v'^2_{p,z} - 2v_t v'_{p,z}\right] & \text{for } 0 < v'_{p,z} < \frac{v_t}{2} \\ +\eta_z\left[-2v_t^2 + 2v_t v'_{p,z} - v'^2_{p,z}\right] & \text{for } v'_{p,z} > \frac{v_t}{2} \end{cases}. \tag{2.24}$$

Implicit integration of the differential equation:

$$\frac{dy}{dt} = ay^2 + by + c, \tag{2.25}$$

has the following solution:

$$y_{i+1} = -\frac{b}{2a} + \frac{1}{2a\Delta t} \pm \sqrt{\left(\frac{b}{2a} - \frac{1}{2a\Delta t}\right)^2 - \frac{y_i + c\Delta t}{a\Delta t}}, \tag{2.26}$$

which are applied to find the following solutions of Eqs. 2.23 and 2.24:

$$v'_{p,xy,i+1} = \begin{cases} +Q_1 - \sqrt{Q_1^2 + Q_2} & \text{for } U_{xy,i} < 0 \\ -Q_1 + \sqrt{Q_1^2 + Q_2} & \text{for } U_{xy,i} > 0 \end{cases}, \tag{2.27}$$

$$v'_{p,z,i+1} = \begin{cases} +Q_3 - \sqrt{Q_3^2 + Q_4} & \text{for } U_{z,i} < 0 \\ -Q_3 + \sqrt{Q_3^2 + Q_4} & \text{for } 0 < U_{z,i} < \frac{v_t}{2} \\ -Q_3 + \sqrt{Q_3^2 + Q_5} & \text{for } U_{z,i} > \frac{v_t}{2} \end{cases}, \tag{2.28}$$

with

$$U_{xy,i} = v_{a,xy,i+1} - (v'_{p,xy,i} + v_{a,xy,i}), \tag{2.29}$$

$$U_{z,i} = v_{a,z,i+1} - (v'_{p,i,z} + v_{a,z,i}), \tag{2.30}$$

$$Q_1 = \frac{1}{2\eta_{xy}\Delta t}, \quad Q_2 = \left|\frac{U_{xy,i}}{\eta_{xy}\Delta t}\right|, \tag{2.31}$$

$$Q_3 = v_t + \frac{1}{2\eta_z\Delta t}, \quad Q_4 = \left|\frac{U_{z,i}}{\eta_z\Delta t}\right|, \quad Q_5 = Q_4 - 2v_t^2. \tag{2.32}$$

Given the terminal fall speed v_t, raindrop parameters to calculate η_* and a 3-D wind field simulation, it is now possible to integrate the relaxation term $v'_{p,*}$ with finite differences. Typically it is necessary to integrate over a distance on the order of several $d_{I,xyz}$ to obtain a stable solution.

The results of the inertia-correction factors, $\zeta_{*,i}$, that are calculated from the simulations are shown in Fig. 2.4. On the x-axis the length scale L_* is varied, which defines the total distance of the line that spans the raindrop locations. On the y-axis the raindrop-inertia-correction factor is shown. Simulations are performed for
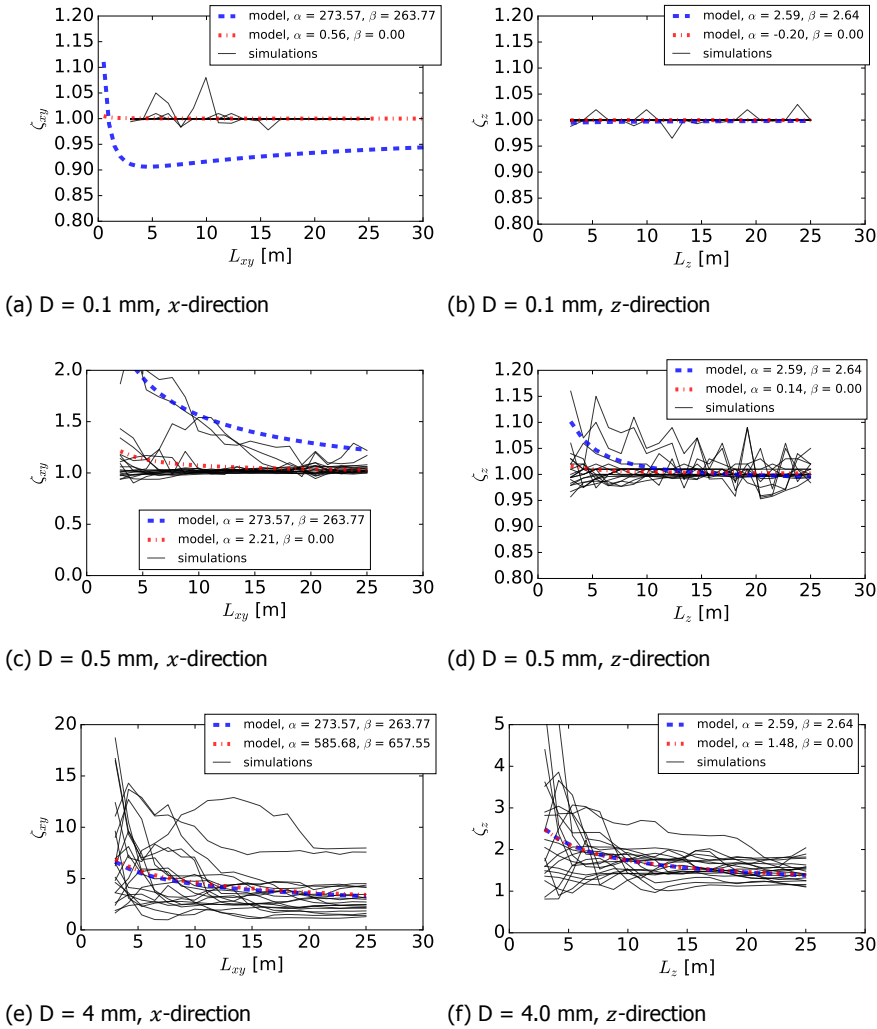
Figure 2.4: Calculation of the inertia factor $\zeta_{*,i}$ for different simulations i, that have a random position in the 3-D wind field simulation. The calculations are performed for different equivolumetric raindrop diameters D, and for different wind velocity components (either x-direction or z-direction).

multiple drop sizes and for different looking directions (x and z). In Fig. 2.4e and Fig. 2.4f, it is shown that for larger droplets the correction becomes more important as it deviates more from 1. The smaller the spatial scale L_*, which corresponds to a smaller spatial sampling volume, the more important the inertia correction becomes.

With a minimization of a cost function (Nelder-Mead Simplex, see e.g. Johnson 2017), where the modeled inertia correction ζ is compared to an inertia correction

D [mm]	α_{xy}	β_{xy}	RMSE of ζ
0.10	0.56	0.00	1.08e-03
0.50	2.21	0.00	9.22e-02
4.00	585.68	657.55	1.94e+00
all	273.57	263.77	8.11e-01
D [mm]	α_z	β_z	RMSE of ζ
0.10	-0.20	0.00	5.34e-04
0.50	0.14	0.00	1.45e-02
4.00	1.48	0.00	3.36e-01
all	2.59	2.64	1.21e-01

Table 2.2: Optimized tuning parameters α_* and β_* for the inertia-correction model for raindrops with various equivolumetric diameters D. Also, the root mean square error (RMSE) is calculated.

from the stochastic simulations, it is possible to estimate optimal tuning parameters α_* and β_*, which are summarized in Tab. 2.2. The minimization is executed separately for the x-direction and z-direction, and for different drop sizes. In addition, the optimization of inertial parameters is done for all the drop sizes at the same time. The root mean square error (RMSE) in ζ increases for larger droplets, which can be expected as large raindrops behave more as inertial particles. In Fig. 2.4 it is shown that the model is sufficiently adaptable for the different cases. Another interesting result from the simulations is that especially for large raindrops (e.g. 4 mm) and a high radar resolution ($L \leq 10$ m) the uncertainty for EDR estimation due to the raindrop inertia effect becomes very large.

So in the end, a homogeneous isotropic turbulence was used to estimate the tuning parameters for the proposed inertia-correction model. This was done by calculating the additional velocity due to relaxation for raindrops of different sizes that were moving in the simulated 3D turbulent wind field. Consequently, the radar-measured variance of velocities was calculated with and without adding the additional velocities due to relaxation. This resulted in a correction factor for each individual simulation, which was used to estimate the tuning parameters and their uncertainty. The tuning parameters were estimated for different raindrop sizes and different directions, which showed that the model was sufficiently adaptable for different raindrop size distributions (DSDs). The model may need to be further developed, such that the tuning parameters depend less on the raindrop size distributions. For EDR retrieval techniques, it is suggested to apply the tuning parameters for the equivolumetric raindrop size that fits the best for a certain application. A further interesting result from the simulations was that especially for large raindrops (e.g. 4 mm) and a high radar resolution ($L \leq 10$ m) the uncertainty for EDR estimation due to the raindrop inertia effect becomes very large.

2.5. **Conclusions**

In this chapter, raindrop inertia parameters were estimated from the raindrop equations of motion. The equations of motion for a raindrop were solved analytically for the 'sudden jump case', from which the inertial distance and the inertial time were defined. It became clear that the inertia effect is anisotropic, i.e. has a different behavior in the x/y-direction and z-direction. These inertial parameters, based on the 'sudden jump' case, take the forces that are acting on a droplet into account, and are suitable to be used in radar-based turbulence intensity retrieval techniques during rain.

For the application to radar-based turbulence intensity retrieval techniques, a new inertia-correction model is proposed. This model is based on a correction for turbulence scales, given the radar cell sampling space parameters, raindrop inertial distance and model tuning parameters. The inertial correction factor reduces the measured variance of velocities ($\zeta < 1$), as heavy particles respond slowly to the variance of air velocities over their trajectory. It was found that the inertial correction factor can also be amplifying ($\zeta > 1$), as an ensemble of raindrops is able to sense air velocities in a larger space than the radar cell sampling space. The tuning parameters in the inertia-correction model are necessary to connect the raindrop inertial distance parameters (based on the 'sudden jump' case) with the influence of raindrop inertia on the variance of velocities for an ensemble of raindrops. Optimal tuning values have been estimated for different directions and raindrop sizes from the simulations. For large radar total sampling scales ($\gg 30$ m), the influence of inertia on retrieved turbulence intensity becomes negligible. For radar total sampling scales comparable to or smaller than 30 m, the raindrop inertia correction is suggested. For small radar total sampling scales (e.g. ≤ 10 m) and large raindrops (e.g. 4 mm), the application of a turbulence retrieval technique is limited, because the uncertainty in estimated EDR values due to raindrop inertia becomes very large.

In the following chapters, two approaches to apply turbulence intensity retrieval techniques to raindrop scatterers are taken, given the radar total sampling scale dependency: 1) Using large radar total sampling scales, and thus avoiding the influence of raindrop inertia, for the estimation of EDR and wind vectors without applying the proposed novel inertia-correction model (chapters 3 and 4), and 2) The estimation of the drop size distribution (DSD) and EDR, using a radar forward model with the model for raindrop inertia correction included (chapter 5).

3

Velocity-based EDR retrieval techniques

In this chapter, five velocity-based energy dissipation rate (EDR) retrieval techniques are assessed. These techniques are applied without a correction for the influence of raindrop inertia. This is the way how such techniques always have been applied to Doppler-radar and other velocity measurements. The EDR retrieval techniques are applied to Doppler measurements from TARA (Transportable Atmospheric Radar) - a precipitation profiling radar - operating in the vertically fixed-pointing mode. A generalized formula for the Kolmogorov constant is derived, which gives potential for the application of the EDR retrieval techniques to any radar line of sight (LOS). Two case studies are discussed that contain long-lasting rain events. Consequently, from a comparison of remote with in situ collocated EDR values for the case studies, it is derived which retrieval technique is the best for application to the Doppler radar during rain. To see if the technique is also the best for many other rainy cases in the Netherlands, a massive data analysis is applied to further support the conclusions.

"Scientific progress is comparable to, and is also influenced by, the Dutch weather."

3.1. Introduction

With a radar the Doppler spectral width, or the standard deviation of a series of Doppler velocities, σ_v is measured, which can be modeled as a summation of independent terms as:

$$\sigma_v^2 = \sigma_d^2 + \sigma_0^2 + \sigma_\alpha^2 + \sigma_s^2 + \zeta_I^2 \sigma_T^2 + \sigma_{err}^2, \qquad (3.1)$$

where σ_d is due to variety in hydrometeor fall speeds, σ_0 is due to variety in hydrometeor orientations and vibrations, σ_α is due to antenna motion, σ_s is due to shear, σ_T is due to turbulence, ζ_I is a hydrometeor inertia correction, and σ_{err} is an error due to model assumptions and/or measurement noise (Doviak and Zrnić 1993; Oude Nijhuis et al. 2016b). Under special circumstances, additional terms can exist in Eq. 3.1, such as gravity waves (e.g. Nastrom 1997; Nastrom and Eaton 1997; Wilson 2004). The shear term can be retrieved from estimates of the wind vector derivatives (Borque et al. 2016; Gossard 1990). Precipitating raindrops have a non-negligible terminal fall velocity, because of their relatively large mass and volume. Therefore, a significant contribution in Eq. 3.1 due to variety in hydrometeor fall velocities σ_d can be expected. In addition, the raindrop inertia effect, which can be characterized as velocity differences due to relaxation, can enlarge or reduce the measured variance of turbulence velocities via ζ_I (chapter 2). The terms that are related to the rain characteristics, σ_d and ζ_I, can be estimated from radar observables via the raindrop size distribution (DSD) parameters. The rain DSD parameters can be estimated from the radar reflectivity, and/or other radar observables (e.g. Brandes et al. 2004; Marshall and Palmer 1948; Unal 2015).
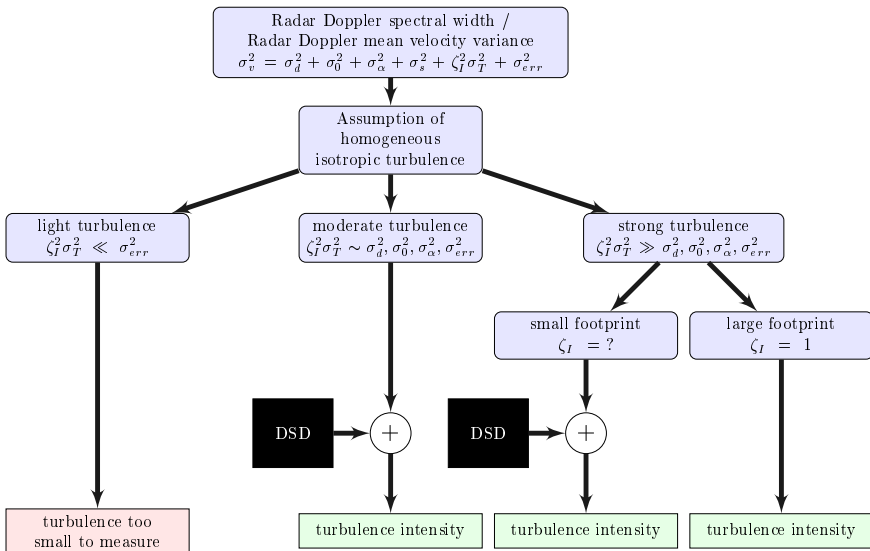

Figure 3.1: The schematic illustrates the assumptions and simplifications that are used in radar-based turbulence intensity retrieval techniques.

The relative sizes of the terms in Eq. 3.1 determine how complex a radar-

based turbulence intensity retrieval technique becomes. This is demonstrated in a schematic in Fig. 3.1. In this schematic the turbulence intensity is qualified by the relative magnitude of the turbulence term in comparison to the other terms in Eq. 3.1. When the turbulence term is smaller than the error term (relative light turbulence), the radar is not able to measure the turbulence intensity. To identify when this is occurring, a minimal value for turbulence intensity that can be measured with the radar can be estimated. When the turbulence term is larger than the error term, the turbulence intensity can be estimated but will rely on corrections for the other terms.

The rain DSD and the total sampling scale of the measurements have an important role in the radar-based turbulence intensity estimation. The total sampling scale λ_{TS} is a measure of the scale at which the velocity measurements are taken to calculate the standard deviation of velocities σ_v, and is used in the calculation of EDR. When EDR is estimated from the radar Doppler spectral width, the total sampling scale can be roughly estimated as $\lambda_{TS} = V^{1/3}$, where V is the total volumetric area that is illuminated in a single radar cell. A more refined expression that takes the power distribution pattern of the radar into account is given by White et al. (1999). The turbulence contribution to the Doppler spectral width, σ_T (Eq. 3.1), increases approximately with the total sampling scale λ_{TS} as $\sigma_T \propto \lambda_{TS}^{1/3}$ in the inertial range due to the Kolmogorov -5/3 power law (e.g. Eq. 3.5 in White et al. 1999). It is not expected that the non-turbulent terms depend on the total sampling scale. Therefore, one solution to reduce the bias in EDR due to inaccurate information on the DSD is to enlarge the total sampling scale λ_{TS} by using multiple radar cells for the estimation of velocity variance due to turbulence.

In the case that σ_d is comparable to $\zeta_I \sigma_T$ (relative moderate turbulence), the DSD parameters are necessary to estimate the turbulence intensity. In the case that σ_d is negligible compared to $\zeta_I \sigma_T$ (relative strong turbulence), it depends on the total sampling scale λ_{TS} whether the influence of the DSD has to be take into account. The exact value for "a sufficiently large total sampling scale to neglect the influence of measuring from raindrops" depends on the characteristics of the rain, where in general it can be stated that larger raindrops have a larger impact on the raindrop inertia term ζ_I. The influence of raindrop inertia can be neglected for radar-based turbulence intensity retrieval techniques for all raindrop DSDs when the total sampling scale is larger than 30 m (chapter 2). Considering all effects of measuring EDR during rain with a radar, the turbulence intensity may be too small to measure, may need additional assumptions on the rain DSD, or can be derived without taking into account the influence of raindrops.

In the radar-based estimation of EDR, it is assumed that turbulence is homogeneous and isotropic, and the measurements are in the inertial range, until it is eventually dissipated to heat at the dissipation scale. An idealized energy spectrum is assumed, having an extensive inertial range: The energy production takes places at the scale of weather systems, which is in the end via eddies dissipated to heat. This means that the energy production scale is approximately 1-10 km, depending on the meteorological conditions, and the energy dissipation occurs at approximately the millimeter scale. In between the energy production scale and the

dissipation scale, there is the inertial range where energy is converted to smaller and smaller scales via eddies. A schematic that illustrates the transfer of energy in the inertial range via eddies is presented in Fig. 3.2. As the dissipation takes place at the millimeter scale (e.g. Piper and Lundquist 2004; Pope 2000), this scale is irrelevant to weather radar measurements of turbulence intensity. For many EDR retrieval techniques, the measurements are assumed to be in the inertial range of the energy spectrum in Fig. 3.2. It should be stressed that this assumption of measuring in the inertial range of the energy spectrum has to be validated, as the turbulent kinetic energy spectrum shown in Fig. 3.2 is just a model.

Next to large-scale weather systems, there are many atmospheric phenomena at smaller scales that produce energy, such as frontal systems, building-induced turbulence or surface friction. At airports, aircraft wake turbulence can be relevant (e.g. Frech 2007). For the cases where the measurements are not in the inertial range, it can be expected that the estimated EDR values are biased. Such cases should somehow be detected in an ideal EDR retrieval technique, and be accounted for in a radar-based estimation of EDR.
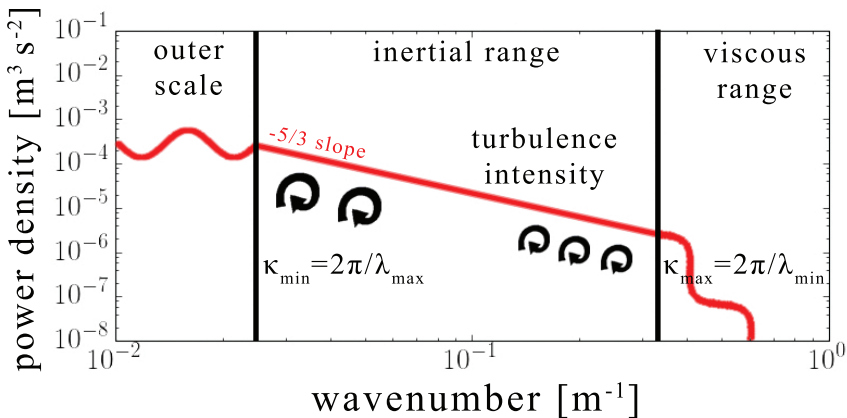

Figure 3.2: In this schematic the theoretical power density of the energy spectrum is plotted against the wavenumber k. The outer scale provides the energy that is eventually dissipated to heat in the viscous range via eddies. In the middle, we find the inertial range, where energy is dissipated from larger to smaller scales, having a -5/3 power law according to Kolmogorov's hypothesis (Kolmogorov 1941).

A correction for the influence of measuring from raindrops in radar-based EDR retrieval technique is challenging, and only useful for some specific scales given the rain DSD. A solution on how to account for the influence of raindrop inertia in radar-based turbulence intensity retrieval techniques is given in chapter 2, where an inertia correction model is proposed using inertial parameters based on the equations of motion for a raindrop and tuning parameters estimated from turbulence simulations.

To account for the inertia of scatterers, the DSD parameters have to be known, which can be based on the radar observables. Such a correction for raindrop inertia allows to resolve for a bias in EDR when it is not too dominant (ζ_I close to 1 in Eq.

3.1). A large correction for raindrop inertia ($\zeta_I > 2$) becomes ineffective, as the uncertainty increases with the stochastic nature of turbulence (chapter 2). In this chapter, we do not use a correction for the influence of raindrop inertia ($\zeta_I = 1$) as the focus is mainly on EDR retrieval techniques that have total sampling scales larger than 30 m (chapter 2).

The goal of this chapter is to apply a set of five velocity-based EDR retrieval techniques to radar-based estimated wind velocities during rain, and prove that the radar is capable of measuring turbulence under rainy conditions. The novelty lies in the active remote sensing of EDR during rain, which can be seen as an extension to other works, which applied such techniques during clear, cloudy and/or drizzle conditions (e.g. Borque et al. 2016; Bryant and Browning 1975; Fang et al. 2014; Kollias and Albrecht 2000; Kollias et al. 2001; O'Connor et al. 2010; Röhner and Träumner 2013; Shupe et al. 2012).

To achieve this goal, a few velocity-based EDR retrieval techniques are selected, which can be applied to both in situ velocity measurements as well as remote radar Doppler measurements. Consequently, EDR values are compared to qualify the performance of these EDR retrieval techniques when applied to the radar during rainy conditions. In this chapter, the emphasis is on the application of EDR retrieval techniques with a total sampling scale larger than 30 m, for which it is expected that the influence of raindrop inertia can be neglected. Energy spectra from collocated sonic anemometers are analyzed to validate that the measurements are in the inertial range. The EDR retrieval techniques are applied to measurements from TARA (Heijnen et al. 2000), which is a precipitation profiling Doppler radar at the Cabauw meteorological supersite (Ulden and Wieringa 1996). This site contains a 200 m tower, with sonic anemometers located at tower levers, which can be used for in situ validation of EDR. Two illustrative cases have been selected, which both contain a long and almost continuous rain event. One case study has relative high EDR values during a storm, whereas the other case has relative low EDR values.

This chapter is organized as follows. In section 2, a set of five velocity-based EDR retrieval techniques is described. In section 3, retrieved EDR values from the radar are validated with an in situ comparison. This chapter ends with the conclusions.

3.2. **Velocity-based EDR retrieval techniques**

In this section, an overview is given of a few velocity-based energy dissipation rate (EDR) retrieval techniques. When they are applied to the radar, a correction is applied for the terminal fall velocities of raindrops, based on the estimation of DSD parameters. The further specific details of the retrieval techniques are provided after this section.

As a consequence of Kolmogorov's similarity hypotheses, which are valid for homogeneous and isotropic turbulence, the turbulent energy spectrum $E(\kappa)$ of three-dimensional wind velocities in the inertial subrange is partitioned among the eddies in a universal form (Kolmogorov 1941; Pope 2000; Sutton 1953):

$$E(\kappa) = C\epsilon^{2/3}\kappa^{-5/3} \qquad [\text{m}^3\text{s}^{-2}], \qquad (3.2)$$

where $\kappa = 2\pi/\lambda$ [m^{-1}] is the wavenumber with length scale λ [m], κ is in the

inertial range, $C = 1.5$ is a Kolmogorov constant obtained from experiments (Pope 2000), and ϵ [m² s⁻³] is the EDR.

In addition to Eq. 3.2, there are similar expressions for the turbulent energy spectrum of the wind components, which are relevant for velocity measurements in the directions longitudinal or transverse to the main wind direction (e.g. Pope 2000). For application of turbulence retrieval techniques to a Doppler radar, it is convenient to be able to use any antenna looking direction, or alternatively speaking, any line of sight (LOS). Therefore, the turbulent energy spectrum is formulated for any arbitrary LOS E_{LOS}:

$$E_{LOS}(\kappa) = C_{LOS}\epsilon^{2/3}\kappa^{-5/3}, \tag{3.3}$$

where C_{LOS} is the Kolmogorov constant for the LOS, given by:

$$C_{LOS}(\theta, \Delta_\phi) = \cos^2\theta\cos^2\Delta_\phi C_{LL} + \cos^2\theta\sin^2\Delta_\phi C_{TT}$$
$$+ \sin^2\theta C_{TT}, \tag{3.4}$$

where θ is the radar antenna elevation angle, and Δ_ϕ is the angle between the LOS and wind direction in the horizontal plane, given by:

$$\Delta_\phi = \phi - \phi_0, \tag{3.5}$$

where ϕ is the radar antenna azimuth, and ϕ_0 is the angle of the horizontal wind direction. The longitudinal Kolmogorov constant C_{LL} and the transverse Kolmogorov constant C_{TT} are given by (e.g. Pope 2000):

$$C_{LL} = \frac{18}{55}C \approx 0.49, \tag{3.6}$$

$$C_{TT} = \frac{4}{3}C_{LL} = \frac{24}{55}C \approx 0.65. \tag{3.7}$$

For writing down the radar Kolmogorov constant, Eq. 3.4, isotropy is assumed, which results in zero shear stress spectra (see §6.5.8 of Pope (2000) for more details). Note that the formulation of Eq. 3.3 still satisfies the turbulent energy spectrum for the longitudinal direction E_{LL}, as $E_{LOS} = E_{LL}$ for ($\theta = 0, \Delta_\phi = 0$), and for the transverse direction as $E_{LOS} = E_{TT}$ for ($\theta = 0, \Delta_\phi = \pi/2$) or ($\theta = \pi/2$).

An alternative representation of the turbulent energy spectrum is the model for the second-order structure function (SSF), which is defined for each spatial separation r as (Pope 2000):

$$D_{2,*}(r) \equiv \langle[x(r'+r) - x(r')]^2\rangle, \tag{3.8}$$
$$= 4C_*(\epsilon r)^{2/3} \quad [\text{m}^2\text{s}^{-2}], \tag{3.9}$$

where x is the 1D wind velocity component or the 3D wind speed, and C_* is a Kolmogorov constant, either C or C_{LOS}. The averaging is done over all possible locations r'. Next to the second-order structure function model, there are models for higher-order structure functions (Katul 1994; Pope 2000). In this work, the higher order structure functions are not considered, as it can be expected that the

EDR retrieval technique	total sampling scale	input variables
VWVV (Vertical Wind Velocity Variance)	long	Standard deviation of vertical wind velocities and the average 3D wind speed
WSV (Wind Speed Variance)	long	Standard deviation of full 3D wind speeds and the average 3D wind speed
STWSV (Short Time Wind Speed Variance)	short	Standard deviation of full 3D wind speeds and the average 3D wind speed
PS (Power Spectrum)	long	series of 3D wind speeds
SSF (Second=order Structure Function)	long	series of 3D wind speeds

Table 3.1: Overview of EDR retrieval techniques that are used in this work, their abbreviations, the scale at which they are applied and the essential input variables. In this work a long time scale of 10 minutes is used, and for a short time scale 5 seconds.

application of higher order statistics results in inaccurate EDR values, because the higher order statistics have stricter requirements with respect to sampling errors.

The formulas for the turbulence energy spectrum, Eq. 3.2 and 3.3, and SSF, Eq. 3.9, are relevant for the spatial domain. In order to apply them to a time series of measurements, it is necessary to convert the energy spectrum and the structure function into the time domain. Using the Taylor hypothesis of frozen turbulence, the formulas are modified (Taylor 1938). For the conversion of the energy spectrum, wavenumbers are replaced by angular frequencies $\chi = 2\pi/t$ [s^{-1}] via the relation $\chi = U_0\kappa$, where U_0 [ms^{-1}] is the average 3D ambient wind speed, and the same kinetic energy is maintained as:

$$E_*(\chi) = C_*\epsilon^{2/3}\chi^{-5/3}U_0^{2/3} \quad [\text{m}^2\text{s}^{-1}]. \tag{3.10}$$

For the structure functions, space lags r are replaced by time lags t via the relation $r = U_0 t$. The values for χ are obtained from the sampling time interval and the total sampling time, with the assumption that the measurements are performed in the inertial range.

In this work, EDR retrieval techniques are relying on a series of 3D wind speed/1D wind velocity measurements, which can be obtained remotely via the Doppler effect with a radar, or in situ with a sonic anemometer. An overview of these techniques is given in Tab. 3.1, and the details are provided in the next subsections.

The set of EDR retrieval techniques includes a reference technique, the vertical wind velocity variance (VWVV) technique, which is often used (e.g. Bouniol et al.

2004; O'Connor et al. 2010; Shupe et al. 2012). It is desirable to apply this VWVV technique to the radar, to be able to make a better comparison with other works, and understand the limitations of this technique with regard to the radar instrument. This technique can be modified into the wind speed variance (WSV) technique, by using the variance of 3D wind speeds instead of the variance of vertical velocities. It can be expected that EDR values estimated with the WSV and VWVV techniques are unbiased for in situ measurements, and that they are approximately the same under the assumption of isotropic turbulence, which was already assumed in the Kolmogorov model to satisfy Eq. 3.2. However, for remote radar measurements during rain, the resulting EDR values from the WSV technique could be much more accurate than the VWVV technique, because the more dominant horizontal wind velocity components are not prone to inaccurate terminal fall velocity corrections.

To address the turbulence scale dependency in this work, two total sampling times are used: a long time scale of 10 minutes and a short time scale of 5 seconds. The 10 minutes time scale is a typically used value (e.g. Siebert et al. 2006). Changing only the time scale in the WSV technique leads to the short time wind speed variance (STWSV) technique. When the sampling for these techniques (WSV and STWSV) with different sampling scales occurs in the inertial range, it is expected that they result in unbiased and similar EDR values. A large difference in EDR due to the applied total sampling time (short/long) can on the other hand thus be seen as an indication that the assumption of measuring isotropic turbulence in the inertial range is not satisfied.

In addition to the given techniques, we also consider a few other techniques, that use the second-order structure function (SSF) or the power spectrum (PS) of the wind speeds/velocities series. They are in particular interesting as they give an alternative uncertainty estimate for the retrieved EDR value, based on differences between a model function and measurements.

The set of EDR retrieval techniques that is given here has been implemented in a Python module, which is publicly available at `https://github.com/albertoudenijhuis/edrlib`. It contains all the necessary functions to apply the EDR retrievals. Documentation and worked examples are available that demonstrate the application of the EDR retrieval techniques described in this work.

3.2.1. Terminal fall velocity correction
To obtain the vertical air velocity from radar Doppler measurements during rain, it is necessary to correct for the terminal fall velocities of raindrops. First, assumptions are made on the used rain DSD model and raindrop terminal fall velocity. Consequently, the DSD parameters are estimated, and a correction for the radar mean terminal fall velocity can be applied.

A common way to describe the rain DSD is by assuming a generalized gamma distribution with three parameters N_0, μ and Λ (e.g. Brandes et al. 2004):

$$N(D) = N_0 D^\mu \exp\left(-\Lambda D\right), \qquad (3.11)$$

where $N(D)$ [mm^{-1} m^{-3}] is the number of particles with an equivolumetric drop diameter between D and $D + dD$, D [mm] is the drop equivolumetric diameter, N_0

is an absolute factor determining the number of particles per unit volume, and Λ [mm^{-1}] and μ [-] are distribution shape parameters.

The terminal fall velocity component along the radar beam is equal to (Atlas et al. 1973):

$$v_f(D) = \alpha - \beta \exp(-0.6D) \quad , \quad D \geq 0.109, \tag{3.12}$$

where D [mm] is the equivolumetric drop diameter, and the parameters are given by:

$$\alpha = 9.65 \sin\theta \text{ [m s}^{-1}\text{]} \quad , \quad \beta = 10.3 \sin\theta \text{ [m s}^{-1}\text{]}, \tag{3.13}$$

where θ is the radar antenna elevation angle.

The estimate for the radar mean terminal fall velocity $\overline{v_f}$ is obtained by the following integral:

$$\overline{v_f} = \int_0^\infty v_f(D)N(D)\sigma(D)dD \Big/ \int_0^\infty N(D)\sigma(D)dD , \tag{3.14}$$

where $\sigma(D)$ is the radar cross section (RCS). For the estimation of $\overline{v_f}$, the absolute factor N_0 of the DSD is not required, and regarding the RCS only the dependency with D has to be known. For weather radars we can assume Rayleigh scattering, and then the RCS is proportional to D^6. The estimate for the radar mean Doppler terminal fall velocity then simplifies to:

$$\overline{v_f} = \alpha - \beta \left[\frac{\Lambda}{\Lambda + 0.6} \right]^{\mu+7} . \tag{3.15}$$

The estimated vertical air velocity is then obtained by subtracting the estimated radar mean fall velocity from the measured mean Doppler velocity.

The estimation of radar DSD parameters is a challenging task for which several approaches can be taken. They can be based on a subset of radar observables, such as radar reflectivity, differential reflectivity, specific differential phases (e.g. Brandes et al. 2004), Doppler spectral analysis (e.g. Unal 2015), multi-frequency techniques (e.g. Meagher and Haddad 2006), or an adaptive approach that uses in situ DSD measurements for calibration (e.g. Takis et al. 2014). The radar mean terminal Doppler velocity can be estimated for most of these radar-based estimated DSDs, as long as the DSD is assumed to have a generalized gamma distribution.

For our case studies the DSD parameters are estimated with work from Marshall and Palmer (1948), because the polarimetric approach is not effective as the radar is vertically oriented, and there is a lack of additional in situ DSD measurements for calibration or validation. Although this approach is not the state-of-the-art (with regards to the aforementioned references), applying this first-order correction will improve the results for the estimated vertical velocities.

3.2.2. Variance techniques (WSV, VWVV and STWSV)

Three EDR retrieval techniques that use the variance of wind as input are explained here. To apply these techniques in the time domain, the Taylor hypothesis of frozen turbulence (Taylor 1938) is used, which requires an average ambient wind speed

U_0. The variance of the 3D wind speed sample series (or the variance of a wind component velocity series due to turbulence) is equivalent to the integral of the power spectrum, Eq. 3.10. For the time domain that is:

$$\sigma_T^2 = \int_{\chi_S}^{\chi_{TS}} E(\chi) d\chi \tag{3.16}$$

$$= \frac{3}{2} C_* \epsilon^{2/3} U_0^{2/3} \left[\chi_S^{-2/3} - \chi_{TS}^{-2/3} \right], \tag{3.17}$$

where χ_S is the angular sampling frequency, and χ_{TS} is the total angular sampling frequency. The angular sampling frequency χ_S is related to the sampling time t_S via $\chi_S = 2\pi/t_S$. And the total angular sampling frequency χ_{TS} is in the same way related to the total sampling time t_{TS}. Here σ_T^2 is the 3D wind speed variance in the case of the WSV or STWSV techniques, and σ_T^2 is the 1D wind component vertical velocity variance in the case of VWVV. The EDR can then be found by solving Eq. 3.17 for ϵ:

$$\epsilon = \left(\frac{3}{2} C_* \left[\chi_S^{-2/3} - \chi_{TS}^{-2/3} \right] \right)^{-3/2} U_0^{-1} \sigma_T^3. \tag{3.18}$$
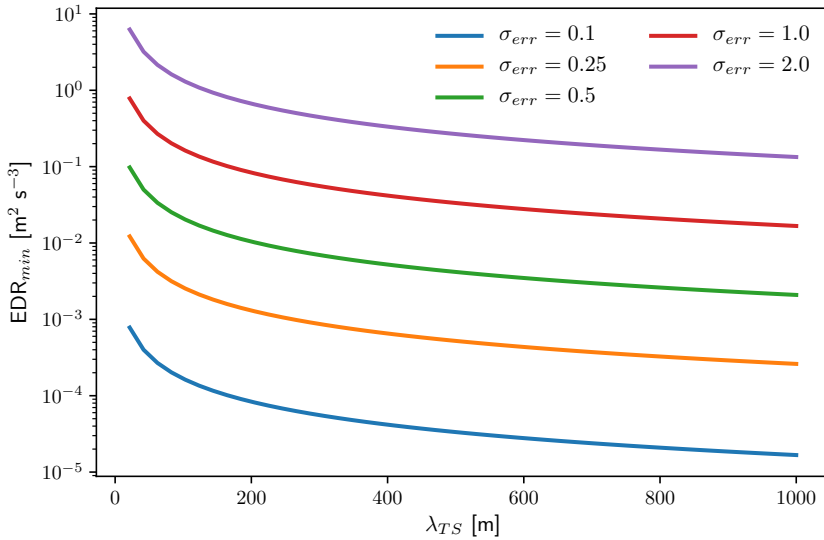

Figure 3.3: Minimal retrievable EDR EDR_{min} as a function of the total sampling scale λ_{TS} for different uncertainties in the variance of a series of wind velocities σ_{err} [m s^{-1}]. A Kolmogorov constant of $C = 1.5$ is used, and the assumption is made of 50 equidistant samples ($\lambda_{TS} = 50\lambda_S$).

A potential problem with the wind variance measurements is that due to noise or errors the turbulence can be too small to measure, and an accurate retrieval of EDR is impossible. This is in particular relevant for the radar, where there are contributions to the wind variance measurements that can be comparable to or

even larger in size than the turbulence contribution (see Eq. 3.1). Given the error in the wind velocity standard deviation σ_{err} (see Eq. 3.1), a criterion for which EDR values can not be accurately retrieved can then be formulated as:

$$\sigma_T \leq 2\sigma_{err}. \tag{3.19}$$

In combination with Eq. 3.17, this results in a lower limit EDR$_{min}$ for retrievable EDR , and is given by:

$$\text{EDR}_{min} = \left(\frac{3}{2} C \left(\left(\frac{2\pi}{\lambda_S} \right)^{-2/3} - \left(\frac{2\pi}{\lambda_{TS}} \right)^{-2/3} \right) \right)^{-3/2} (2\sigma_{err})^3, \tag{3.20}$$

where C is a Kolmogorov constant, $\lambda_S = 2\pi/\kappa_S$ is the spatial sampling scale and $\lambda_{TS} = 2\pi/\kappa_{TS}$ is the total spatial sampling scale. The dependency of EDR$_{min}$ with the total spatial sampling scale λ_{TS} is shown in Fig. 3.3. This figure demonstrates that by using a larger total sampling scale λ_{TS} the accuracy of EDR can be improved, in particular for light turbulence values. The assumption for this is that the measurements are in the inertial range (Eq. 3.2 applies), and that the other contributions to the wind variance measurement in Eq. 3.1 have no or weak dependencies on the total sampling scale.

In addition to the estimation of EDR$_{min}$, the uncertainty of retrieved EDR values for the variance techniques can be estimated with error propagation (e.g. Taylor 1997). Error propagation assumes uncorrelated and Gaussian distributed errors. As ϵ varies on several orders of magnitude, this variable is not suitable for error propagation. The variable $\epsilon^{1/3}$ is used here for the examination of the propagation of errors. Note that typical values for ϵ and $\epsilon^{1/3}$ are given in the introduction. For the time domain we obtain:

$$\left(\frac{\sigma_\epsilon}{\epsilon^{1/3}} \right)^2 = \left[\frac{1}{\epsilon^{1/3}} \left(\partial \epsilon^{1/3} / \partial \chi_{TS} \right) \sigma_{\chi,TS} \right]^2$$

$$+ \left[\frac{1}{\epsilon^{1/3}} \left(\partial \epsilon^{1/3} / \partial \chi_S \right) \sigma_{\chi,S} \right]^2$$

$$+ \left[\frac{1}{\epsilon^{1/3}} \left(\partial \epsilon^{1/3} / \partial U_0 \right) \sigma_{U0} \right]^2$$

$$+ \left[\frac{1}{\epsilon^{1/3}} \left(\partial \epsilon^{1/3} / \partial \sigma_T \right) \sigma_{\sigma,T} \right]^2, \tag{3.21}$$

$$= \frac{1}{9} \frac{\left[\chi_{TS}^{-10/3} \sigma_{\chi,TS}^2 + \chi_S^{-10/3} \sigma_{\chi,S}^2 \right]}{\left[\chi_{TS}^{-2/3} - \chi_S^{-2/3} \right]^2}$$

$$+ \frac{1}{9} \left(\frac{\sigma_{U0}}{U_0} \right)^2 + \frac{1}{9} \frac{9}{2(N-1)}, \tag{3.22}$$

$$\approx \frac{1}{9} \left(\frac{\chi_S}{\chi_{TS}} \right)^{4/3} + \frac{1}{9} \left(\frac{\sigma_{U0}}{U_0} \right)^2 + \frac{1}{2(N-1)}, \tag{3.23}$$

where N is the number of samples, and $\sigma_{\chi,TS}$, $\sigma_{\chi,S}$, σ_{U0}, $\sigma_{\sigma,T}$ are the uncertainties of the variables in the subscript. The last approximation, Eq. 3.23, has been made

by assuming that $\chi_S \ll \chi_{TS}$. Here we used the relation $\sigma_{\sigma,T}/\sigma_T = [2(N-1)]^{-1/2}$ (Taylor 1997), and that $\sigma_\chi \approx \chi^2/\chi_{TS}$. The last relation is derived from uncertainty propagation (e.g. Taylor 1997), $\frac{\sigma_{\chi,TS}}{\chi_{TS}} = \frac{\sigma_{t,TS}}{t_{TS}}$, and that $\sigma_{t,TS} \approx t_S$, where $\sigma_{t,TS}$ is the uncertainty in sampling time. From this uncertainty analysis, we conclude that sufficient samples are necessary for averaging ($N > 50$), the EDR estimation uncertainty increases with the relative variation of the wind speed σ_{U0}/U_0, and the EDR estimation uncertainty increases with χ_S/χ_{TS}. For reference we give the uncertainty propagation result for the space domain as well, for which the derivation is similar:

$$\left(\frac{\sigma_\epsilon}{\epsilon^{1/3}}\right)^2 \approx \frac{1}{9}\left(\frac{\kappa_S}{\kappa_{TS}}\right)^{4/3} + \frac{1}{2(N-1)}, \tag{3.24}$$

where the assumption is made that $\kappa_S \ll \kappa_{TS}$. We note here that this estimated uncertainty for EDR values should be treated carefully, and can be artificially low when the measurements are not in the inertial range, or the turbulence intensity fluctuates during the measurements (i.e. when the turbulence is not stationary). The estimated uncertainty of this and other methods will be further discussed for the measurements in the study cases.

3.2.3. Techniques based on time series of wind speeds (PS, SSF)

In this subsection, retrieval techniques are discussed where the EDR is obtained from the power spectrum (PS), or from the second-order structure function (SSF). The assumption is that the measured velocity samples are in the inertial range of the energy spectrum. These two techniques allow for the estimation of EDR in sampling subdomains, and thus provide an alternative EDR uncertainty estimation.

For the power spectrum EDR retrieval technique (referred to as PS), first the power spectrum is calculated for a series of 3D wind speeds. The power spectrum is obtained via the Wiener-Khinchin theorem, where a discrete Fourier transformation is applied to the autocorrelation of the given samples. For each discrete frequency χ_j the power P_j is calculated. Consequently, the spectrum is divided into a certain number of frequency intervals, and for each i-th interval $[\chi_1, \chi_2]$ we can find the standard deviation of wind speeds σ_i:

$$\sigma_i^2 = \sum_{\chi_1}^{\chi_2} P_j. \tag{3.25}$$

Given σ_i, χ_1, χ_2, Eq. 3.18 is used to calculate an EDR value for the i-th frequency interval. The final estimate $\widehat{\epsilon_f^{1/3}}$ comes from the average of $\epsilon^{1/3}$-values:

$$\widehat{\epsilon_f^{1/3}} = \overline{\epsilon^{1/3}} \pm \sigma_\epsilon, \tag{3.26}$$

where the uncertainty in EDR is estimated from the standard deviation of $\epsilon^{1/3}$-values.

To better comprehend the PS technique, we can look at the number of frequency intervals. In the limit of 1 frequency interval, the PS retrieval technique is the same as the WSV technique. This emphasizes the difference between the PS and WSV techniques. The WSV technique gives most of the weight of the retrieved EDR to the smallest frequencies (largest spatial/time scales), due to the -5/3 scaling with frequency in the spectrum (see Eq. 3.10). On the contrary, the PS technique with multiple frequency intervals gives extra weight to the larger frequencies (smaller spatial/time scales). For the PS technique in this work, the spectrum is divided into three equally-sized frequency intervals. With this choice, the PS technique deviates from the WSV technique (just one interval), and at the same time unstable results are avoided that can occur with insufficient sampling.

The second-order structure function EDR retrieval technique (referred to as SSF) is applied in the time domain in this work. A time series of wind speeds with N samples is used to calculate the structure function (Eq. 3.9 in combination with $r = U_0 t$) from time lags $t = t_S$ until $t = N t_S/2$, where t_S is the sampling time. This is done in a such way that at least $N/2$ samples are used to calculate each term (for non-periodic signals). Consequently, for each time lag t an EDR value is obtained with:

$$\epsilon = \frac{1}{U_0 t} \left[\frac{D_{2,*}(t)}{4C_*} \right]^{3/2}. \tag{3.27}$$

The final EDR value and its uncertainty are then calculated from the $\epsilon^{1/3}$-values for each time lag t, via Eq. 3.26.

Advantages of these techniques, with respect to the variance techniques, are that: (1) insight can be obtained from visual inspection of fitted functions with regard to processed measurements; and (2) a model error can be estimated from the fitted results. A disadvantage is that the processing becomes more complex, and more retrieval settings have to be chosen, which can lead to unstable results. With unstable it is meant that the result can depend on the chosen parameters, such as the number of frequency intervals for the PS technique.

In this work 3D wind speeds are used as input for the PS and SSF techniques, because the aim is to find techniques for the radar during rain, which are less dependent on accurate DSD parameter estimation, and the 3D wind speeds are less prone to terminal fall velocity corrections. Alternatively, wind velocity components could be used.

Two cases are shown in Fig. 3.4 for sonic anemometer measurements. For the PS technique, the discrete power P_k [m^2 s^{-2}] is plotted versus angular frequency χ [s^{-1}]. The model (Eq. 3.17) is plotted for the three frequency interval for which EDR is estimated. In addition to that, the estimated uncertainty is plotted (Eq. 3.17) with dashed lines. For case A the uncertainty was rather large, and there was no lower limit for the uncertainty ($\widehat{\epsilon_f^{1/3}} - 2\sigma_e < 0$). For case B the uncertainty was much less, which indicates that the samples are more likely in the inertial range. For the SSF technique, the estimated EDR for each time lag (Eq. 3.27) and the model function (Eq. 3.9) are shown. Also, for the SSF the uncertainty of the estimated EDR is plotted with dashed lines.
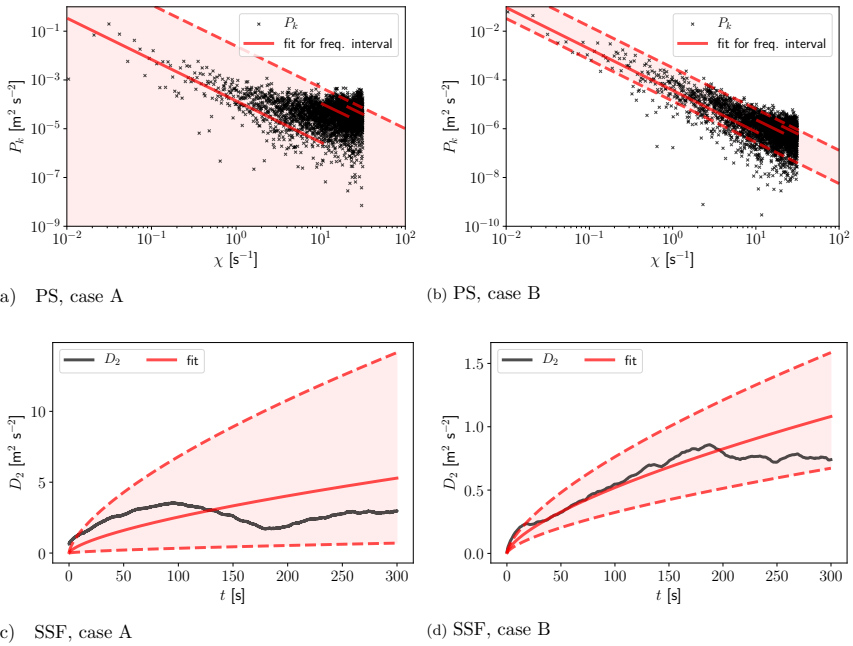
3

(a)   PS, case A

(b)   PS, case B

(c)   SSF, case A

(d)   SSF, case B

Figure 3.4: Examples of the (a) - (b) PS and (c) - (d) SSF retrieval retrieval techniques for EDR, which have a series of 3D wind speeds as input. In (a) - (b) the discrete power P_k [m² s⁻²] is plotted as a function of angular frequency χ [s⁻¹]. In (c) - (d) the second-order structure function D_2 [m² s⁻²] (Eq. 3.9) is plotted as a function of lag time t [s]. The black crosses/lines show the processed velocity samples, and the red lines show the model functions. The dashed red lines show the 2 times STD uncertainty of the model (model function evaluated at $\overline{\epsilon^{1/3}} \pm 2\sigma_\epsilon$). Sonic anemometers are used for the input for 3D wind speeds, which have a sampling time of $t_S = 0.1$ s, and a total sampling time of $t_{TS} = 600$ s. Case A is for 900 UTC 10 April 2012, and case B is for 1200 UTC 10 April 2012.

3.3. Selected case studies

The validation of EDR retrieval techniques is done by a comparison of EDR values from a Doppler radar during rain with EDR values from in situ measurements. In this study two instruments are used, which are TARA - an S-band precipitation profiling radar (Heijnen et al. 2000) - and sonic anemometers placed on levers at several altitudes of a 200 m research tower in the Netherlands. These instruments are located on a meteorological supersite, which is well equipped for atmospheric boundary layer research (Casso-Torralba et al. 2008; Ulden and Wieringa 1996). On this site the TARA radar and the research tower are closely located, and can be used for the comparison and validation of the EDR retrieval techniques.

For the validation of EDR by comparison, two rain events are chosen on 10 April 2012 and 21 June 2012. The first case study has moderate turbulence levels, whereas the latter case has some peak values for turbulence intensity (turbulence intensity levels can be found in e.g. ICAO 2007a).

On 10 April 2012, a cold front passes Cabauw during the morning. The daily

total rainfall is 4.1 mm, which is accumulated in approximately 9 hours. The wind is coming mainly from the south south west.

On 21 June 2012 a cold front passes over the site in the evening. The daily total rainfall is 14.1 mm, which is accumulated in approximately 3 hours. The wind is coming mainly from the east south east. During the rain on this day, there was a summer storm, for which lightning strikes were reported.

3.3.1. Sonic anemometers

For the estimation of in situ EDR values, the Gill R3 sonic anemometers are used, which are mounted at levers at 5, 60, 100 and 180 m on the Cabauw research tower. The instantaneous wind speed and direction are determined using the effect of the wind influence on the propagation time of acoustic pulses transmitted in opposite directions from two arms of the instrument. The raw data, including the three orthogonal wind components and the sonic anemometer temperature, are stored with a frequency of 10 Hz.

The wind component measurement accuracy is less than 0.02 m s^{-1}, where effects of tower mounting are not taken into account. The sonic anemometer measurements can be disrupted by the presence of water droplets on the transducer. To mitigate this effect, we filter out data with unrealistic wind changes that are higher than 500 m s^{-2}. Less than 1% is filtered by this procedure, and unrealistic velocity spikes during rain events are filtered out. Whenever the horizontal wind direction is in the range of 280-340 degrees, the data quality is flagged, because for such cases the sonic anemometer is in the wake of the tower. For the calculation of moving averages we require to have at least 50% of the samples available within the total sampling time, and otherwise the data quality is flagged. Whenever the data quality is flagged, it is not used for comparisons or in plots.

Fig. 3.5 shows measurements of the sonic anemometers wind speeds at different altitudes. We can see a typical vertical structure within these rain events for the wind speed, as it increases with height. In Fig. 3.6 the vertical wind velocity is shown for the sonic anemometer at 180 m altitude. A 10-minute-moving average is used to calculate the vertical wind velocity, which is on average close to zero and for the case studies never exceeds more than 2 m s^{-1} in magnitude. The 10-minute-moving average for the vertical wind velocity is in particular useful for the validation of the radar-based vertical-velocity correction for raindrops. Using 10 minutes for averaging also overcomes difficulties of comparing the results from two instruments that are spatially separated. Figs. 3.5 and 3.6 demonstrate thus that the sonic anemometers were capable to measure the vertical velocities during these rain events, and can thus be used for in situ validation. This is not trivial, because unrealistic spiked velocities had to be removed with the filtering strategy.

3.3.2. TARA radar

TARA is a polarimetric S-band (frequency 3.298 GHz, wavelength 9.1 cm, horizontal/vertical polarizations, far-field region starting at ∼200 m range) FMCW radar that was developed at the Delft University of Technology (Heijnen et al. 2000). Besides the main beam with polarimetric measurement capabilities, TARA has two offset

beams at vertical polarization pointing with an offset angle of 15 ° with respect to the main beam in the radar-antenna-elevation-looking angle and the radar-antenna-azimuth-looking angle directions. Its antennas are pointing with a fixed antenna elevation ($\sigma_\alpha = 0$ in Eq. 3.1). In this work, the main beam has a radar antenna elevation looking angle of $\theta = 75°$. The first offset beam has the same radar antenna azimuth looking angle and an elevation looking angle of $\theta = 90°$, and the second offset beam has a radar antenna azimuth looking angle offset of $+15°$, with a radar elevation looking angle of $\theta = 69°$. The radar transmits linear frequency modulated sweeps, alternately at horizontal and vertical polarization for the main beam, and linear frequency modulated sweeps at vertical polarization for the two offset beams. The backscattered signal is received by a one-channel receiver, either from the main beam (horizontal or vertical polarization) or by one of the two offset beams.

The velocity estimation is based on analysis of the Doppler frequency shift, caused by the displacement of hydrometeor particles and spatial irregularities of atmospheric refractive index, which are related to variations in air temperature and humidity. A Doppler polarimetric dealiasing technique, described in Unal and Moisseev (2004), takes care of unfolding the Doppler velocities. By combining the Doppler measurements from the three beams, the horizontal wind speed and direction, and the vertical Doppler velocity can be estimated at high time and spatial resolution (Unal et al. 2012). The dataset contains the time-height indicators of the main beam reflectivity (dBZ), the estimated horizontal wind speed and direction and the vertical Doppler velocity. The processed radar data have 2.5 s time resolution and 30 m range resolution. The altitude range is between 200 m and 15 km. There is no radar data available from TARA in the case of clear air and very calm conditions, because the measurement technique relies on backscattering from atmospheric inhomogeneities or particles. There is also no information when the LOS velocity modulus is below ± 0.2 m s^{-1}, due to the Doppler filtering strategy in the non-polarimetric offset beams.

In Fig. 3.7 the measured reflectivity factors and Doppler velocities for the main beam from TARA are shown. We can see that there was strong precipitation on 21 June 2012, as there were high reflectivity factors. On 10 April 2012 the rain intensities were moderate. For both cases, a melting layer can be recognized from increased reflectivity factors at ~1.7 km and ~3 km respectively. At these and higher altitudes, the interaction between the ambient wind and the tracers becomes much more complex due to the presence of non-liquid hydrometeors, and is outside the scope of this study.

3.3.3. Comparison of remote with in situ measurements

In this work, only the first radar range cell of TARA is used for EDR estimation, because only at this altitude there is an in situ comparison possible with a sonic anemometer at 180 m altitude. The first range cell of TARA has a sampling space that has its altitude between 173 and 202 m. Only the data with good quality is used for data analysis and in the EDR retrieval techniques. The data is not used in case of one of the following conditions:

1. the sonic anemometer is possibly in the wake of the tower (explained in sub-section 3.3.1);

2. the radar reflectivity factor is less than -20 dBZ for the main or offset beam;

3. the backscattering is inhomogeneous for the three beams (one beam reflectivity is more than the average $\pm$ 3 dB);

4. less than 50% of the samples are usable for a given total sampling time.

In the presence of precipitation, the measured radar Doppler velocity represents the reflectivity weighted LOS velocities of the scatterers. An estimate for the air LOS velocity is then obtained by a correction for the radar mean Doppler terminal fall velocity (details in section 3.2.1).

The resulting 3D wind speed retrieved from TARA for the first range cell is shown in Fig. 3.5, and the vertical wind velocity is shown in Fig. 3.6. The figures show qualitatively that the air wind speed is well captured by TARA, but the remotely retrieved vertical wind velocity has biases of up to 3 m s^{-1}. A bias in the radar-based retrieved vertical velocities is by itself not problematic for the estimation of EDR, which is based on the velocity fluctuations. However, if the bias in estimated vertical velocity fluctuates with time, then the estimate for standard deviation of vertical air velocities will be compromised. In Fig. 3.6, fluctuations in the estimated vertical wind velocity of about 2 m s^{-1} are shown for the study cases. Therefore, it can be expected that the EDR values from the VWVV technique are less accurate.

The biases in vertical velocity have a complex origin that differs from case to case, and could be explained by inaccurately estimated rain DSD parameters. To our knowledge, there has been no validation of radar-based estimated vertical air velocities during rain, which includes the estimation of DSD parameters. Note that for the case studies, the used correction for terminal fall velocity was still useful, because without such a correction the biases could be as large as the largest terminal fall speeds, which are up to about 10 m s^{-1}.

3.3.4. Comparison of retrieved EDR values

One concern with the application of EDR retrieval techniques is whether the measurements are in the inertial range. Or with other words, Eq. 3.2 applies to the measurements. To analyze this, averaged power spectra are obtained from sonic anemometer wind speed measurements at 180 m altitude for a few times points, and are shown in Fig. 3.8. We note here that the radar is not useful for estimating power spectra, because of the much longer sampling time and the radar data quality. Fig. 3.8 shows that for short time scales (smaller than approximately 10^2 s, or approximately $\chi > 10^{-1}$ rad s^{-1}), the power spectra do not satisfy the $-5/3$ power scaling for 0900 and 1200 UTC 10 April 2012. This can be associated with boundary layer processes, such as energy transport, surface friction, and windshear (see Fig. 3.5). The part of the power spectra of 3D wind speeds for time scales longer than 10^2 s are in the inertial range. This proves that the velocity measurements at the scale of 10 minutes are in the inertial range. As a result, the assumption of measuring in the inertial range is demonstrated for the EDR retrieval techniques

that are based on the energy estimate of velocities at the scale of 10 minutes in this work (WSV, VWVV) . For the STWSV technique, the measurements will not always be in the inertial range, for which biased EDR estimates can be expected. For the techniques that process spectra of 3D wind speeds (PS, SSF), EDR values will be biased if the measurements are not in the inertial range, but at the same time their error estimate gives a measure of how well the measurements are in the inertial range.

Estimated EDR values and uncertainties are shown in Fig. 3.9 for both the TARA radar and the in situ measurements from the sonic anemometer. These EDR estimations are for the same times as the estimated power spectra in Fig. 3.8. For 1200 UTC 10 April 2012, consistency is found for the different EDR retrieval techniques, which can be expected as the obtained spectra in Fig. 3.8 showed that the inertial range was applicable for time scales from $\sim10^1$ until $\sim10^3$ s. For the PS technique, rather large errors are found, which may be a consequence of insufficient averaging of spectra. We further note that the estimated uncertainty with error propagation (VWVV, WSV and STWSV in Fig. 3.9) are often on the low side. This may be a consequence of that this estimated uncertainty does not include a broader range of the energy spectrum, which the other uncertainty estimates do (PS, SSF). In contrast to the PS technique, the error estimated with the SSF technique does not suffer from insufficient samples or averaging, and thus seems to be the best choice for uncertainty estimation from the discussed techniques.

In Figs. 3.10a and 3.10b, time series of EDR are shown for EDR retrieval techniques applied to in situ measurements from the sonic anemometer at 180 m altitude. Both cases have values of EDR varying on a logarithmic scale from approximately 10^{-7} up to 10^{-2} m^2 s^{-3}. An agreement is found for the different EDR retrieval techniques (WSV, VWVV, SSF), where the time variation of EDR is similar. The EDR values do not differ much more than one order of magnitude.

Time series for the remote retrieval of EDR values during rain from the TARA instrument are shown in Fig. 3.10c and 3.10d. The differences in EDR values from the remote radar measurements during rain from different techniques are now, in contrast to the in situ measurements, larger and up to 2 orders of magnitude. The time variation of the SSF technique is very similar to the WSV technique in Fig. 3.10c, which is based on the same measurements of 3D wind speeds. In Fig. 3.10d the SSF could not be applied, because the radar measurements contained incomplete time series, due to insufficient quality (see quality conditions in section 3.3.3), which makes this technique less versatile in its application. The times series from the PS and STWSV techniques are not shown in Fig. 3.10, because of its large biases and uncertainties (see Fig. 3.9).

In Fig. 3.11 scatter density plots are shown for the VWVV and WSV techniques to assess these techniques quantitatively. A good correlation of 0.79 was found for the comparison of in situ versus remote EDR values for the WSV technique during rain. The retrieved values from the radar are, however, biased towards higher EDR values: the sonic values are predominantly between 10^{-4} and 10^{-3} m^2 s^{-3}, and the radar values are predominantly between $10^{-3.5}$ and $10^{-2.5}$ m^2 s^{-3}. In addition to this bias, the radar did not measure EDR values lower than $10^{-4.5}$ m^2 s^{-3} for the

WSV technique. The VWVV comparison of in situ versus remote EDR values during rain is not very impressive, which is most likely due to non-reliable raindrop terminal fall velocity corrections. Therefore, the WSV is recommended for applications, but caution is necessary because very low EDR values can not be estimated, and a small bias towards higher EDR values should be expected.
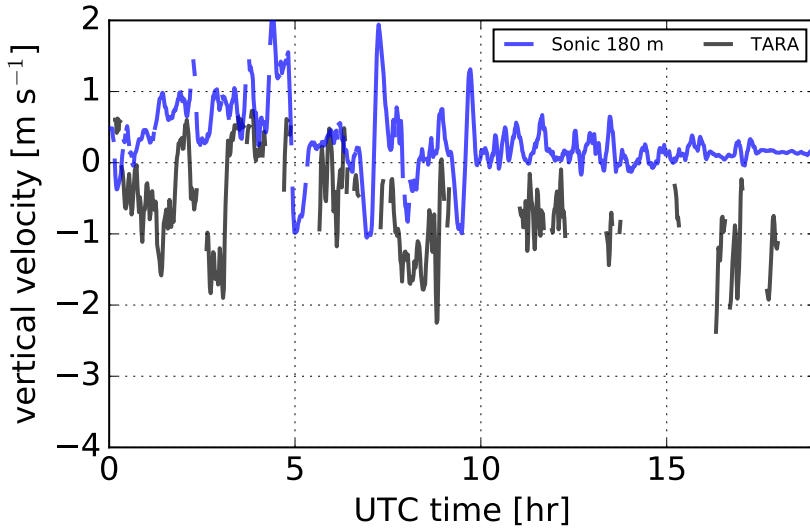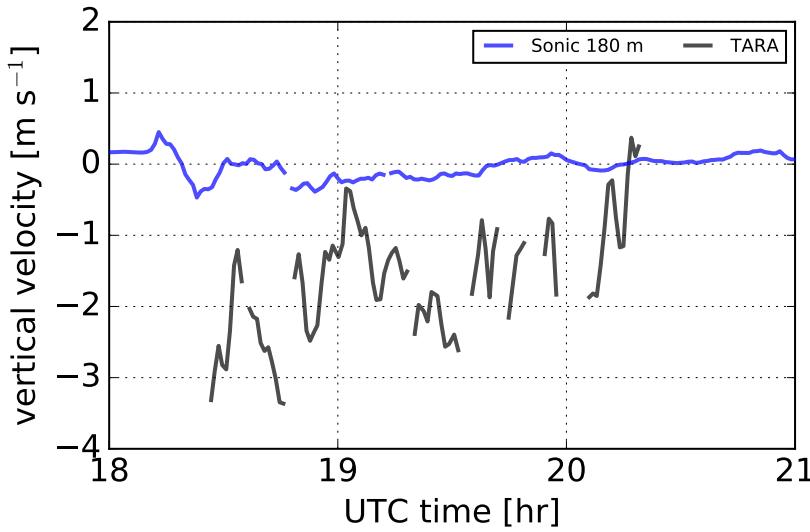
3

3
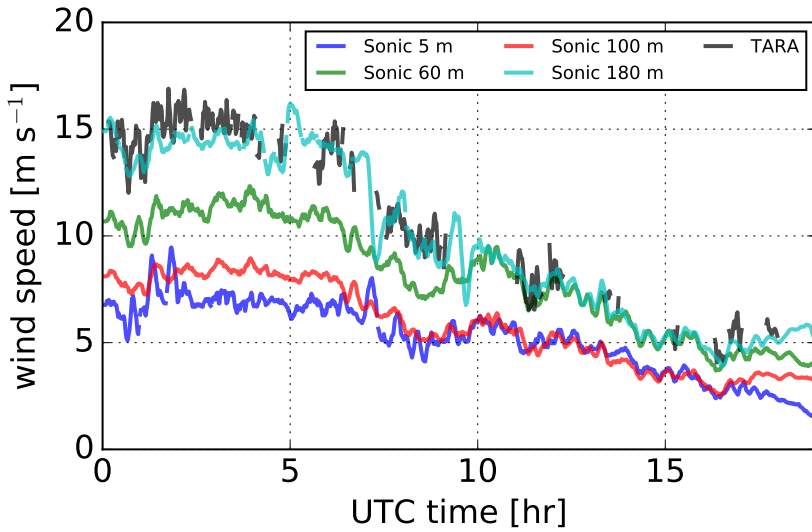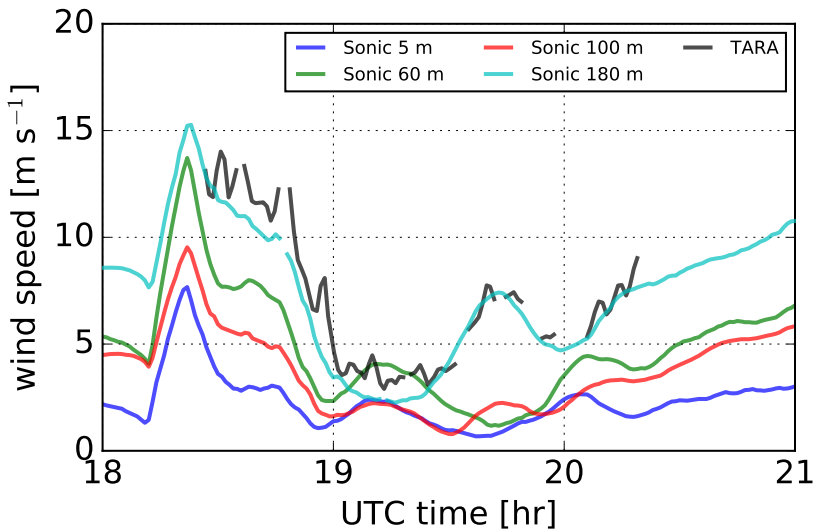
(a)   10 April 2012

(b)   21 June 2012

Figure 3.5: 10-minute-moving average of wind speed on (a) 10 April 2012, and (b) 21 June 2012 for the sonic anemometers at different altitudes and the first range cell of TARA where the radar resolution volume spans from 173 to 202 m altitude.

(a) 10 April 2012

(b) 21 June 2012

Figure 3.6: 10-minute-moving average of vertical wind velocity measured with a sonic anemometer at 180 m altitude and with TARA for the first range cell on (a) 10 April 2012 and (b) 21 June 2012. For TARA a correction has been applied for the raindrop terminal fall velocity (Eq. 3.15).
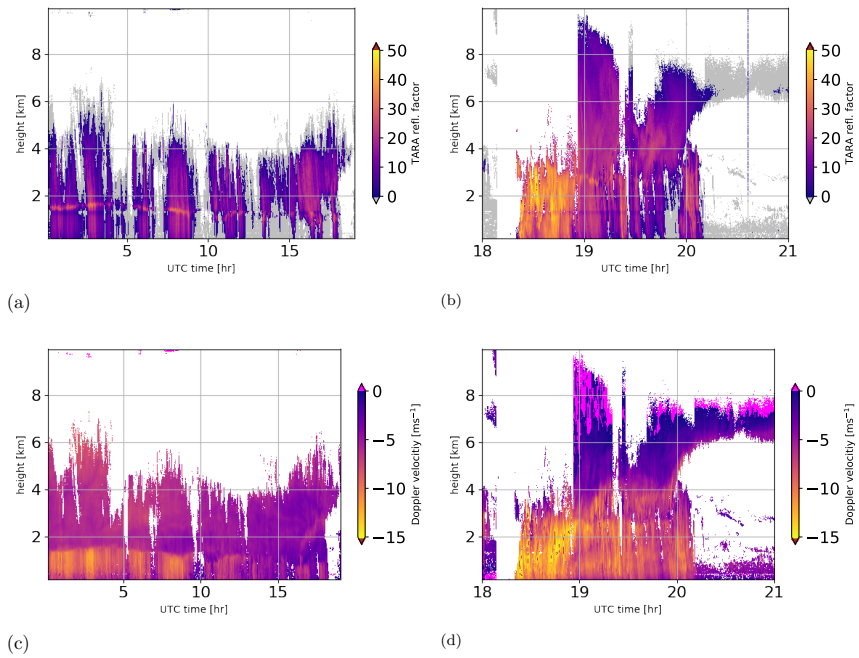
3

(a)

(b)

(c)

(d)

Figure 3.7: Radar measurements from TARA: (a) - (b) reflectivity factors and (c) - (d) Doppler velocities for the main beam (antenna elevation angle of 75 °) on 10 April 2012 (left) and 21 June 2012 (right). Note that the measurement of the upper part of the precipitating cloud is missing before 19:00 in (b) and (d), because of the automatic decrease of the transmit power to avoid receiver saturation.
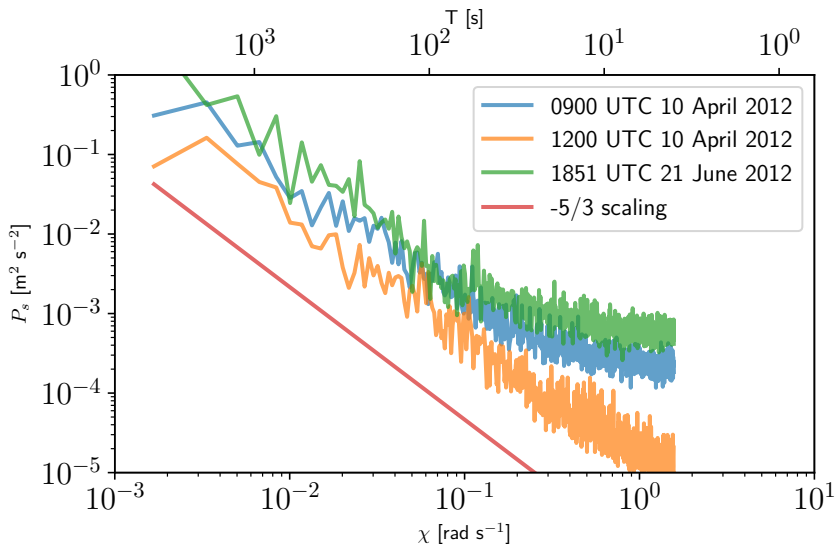
Figure 3.8: Averaged power spectrum of wind speed from the sonic anemometer. The discrete power P_k [m² s⁻²] is plotted as a function of angular frequency χ [s⁻¹]. The averaging has been applied over 1000 spectra to reduce noise. The total sampling time was one hour (± 3 minutes with respect to the time in the legend).

3

(a)   0900 UTC 10 April 2012   (b) 1200 UTC 10 April 2012
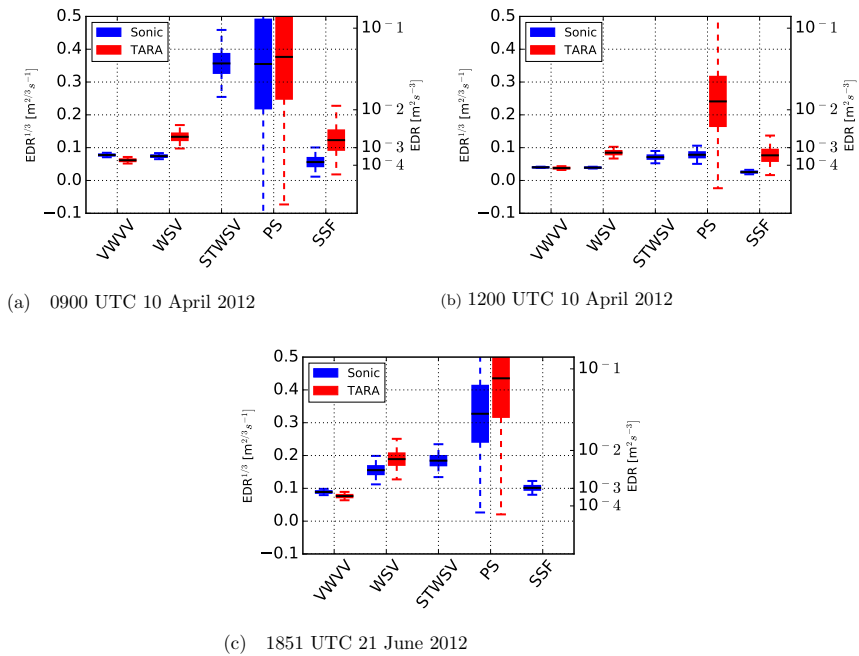
(c)   1851 UTC 21 June 2012

Figure 3.9: Estimated EDR values and uncertainties for TARA and the sonic anemometer on: (a) 0900 UTC 10 April 2012, (b) 1200 UTC 10 April 2012, and (c) 1851 UTC 21 June 2012. The box indicates the standard deviation (STD) uncertainty and the outer edges 2 times the STD. For TARA the SSF could not be applied on 1851, because of insufficient samples.
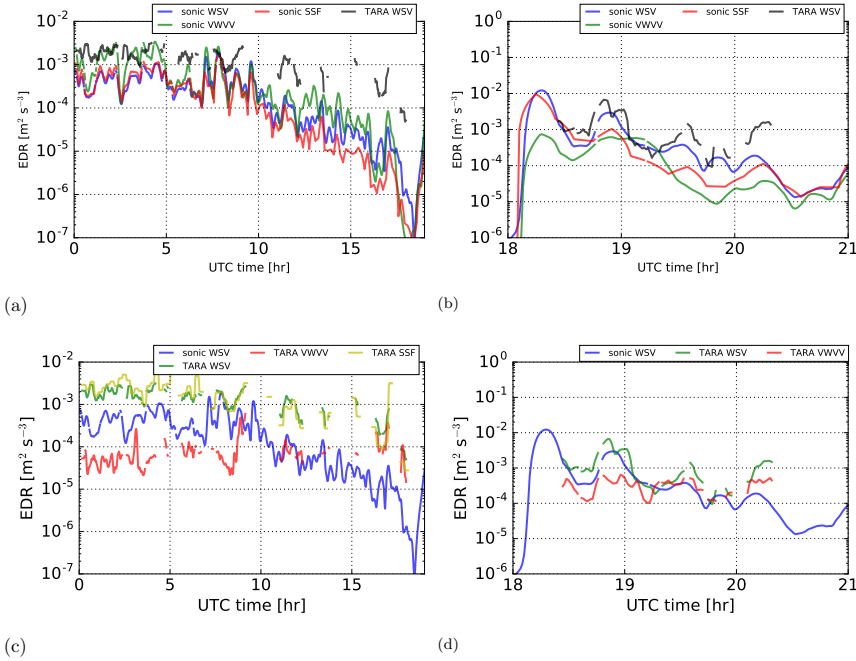
3

Figure 3.10: Retrieved EDR values from the sonic anemometer and the TARA radar for 10 April 2012 (left) and 21 June 2012 (right). In the top results from a set of EDR retrieval techniques are shown, which were obtained from the sonic anemometer at 180 m altitude. In the bottom, results from a set of EDR retrieval techniques applied to TARA are shown. For comparison, the WSV technique is always shown for both instruments.
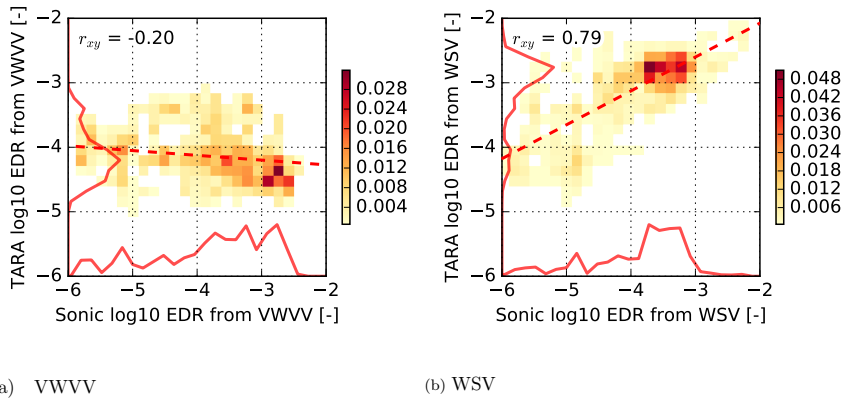
3

(a)   VWVV

(b) WSV

Figure 3.11: Scatter density plot of EDR values obtained with (a) VWVV and (b) WSV retrieval techniques for the two case studies. Relative occurrence is plotted in each pixel for the radar (y-axis) against the in situ sonic measurements (x-axis). On top of the axis the relative distribution is plotted and the correlation coefficient r_{xy} is printed.

3.4. Massive data analysis

In the previous section, the analysis of EDR retrieval techniques was limited to just two study cases. A potential problem with the derived conclusions for the two study cases is that they may be only valid for the same specific weather conditions. Therefore, the performance of the EDR retrieval techniques is tested in this section with an extensive analysis of 140 days of radar data. The main advantage of such an extensive data analysis is that the estimation of statistics, such as correlation coefficients and distributions, is improved significantly, and the statistics are more representative for all rainy weather conditions in the Netherlands, instead of being representative for just the two study cases.

In this work, a massive data analysis tool has been developed and applied to overcome the difficulties when dealing with large amounts of data. When a dataset becomes very large, ordinary statistical data analysis tools become either unfeasible or impractical. Such datasets are qualified as massive datasets (Hoerl et al. 2014; Kettenring 2009). The addition of summary statistics is an exact solution to problems with the calculation of statistics for massive datasets. The addition of summary statistics is implemented in a tool that is called "comparison of everything with everything" (CEWE), which is another massive data analysis tool in the form of a Python module (Oude Nijhuis 2016). Some other handy features of this massive data analysis tool are that: (1) it can handle circular variables and (2) it produces self-descriptive hierarchical data 5 (HDF5) format files, containing statistics that can easily be recombined.

The CEWE tool is applied to TARA (Heijnen et al. 2000) data, which is located at the Cabauw meteorological supersite (Ulden and Wieringa 1996). In total 140 days are processed, covering a time period from 1 January until 13 August 2012, which all have the 75 ° main beam elevation configuration. Statistics were calculated for about 80 atmospheric parameters, including EDR values from different retrieval techniques and more regular atmospheric variables from the research site, such as temperature and relative humidity. The total dataset for which the statistics are calculated have a size with an order of magnitude of 100s of gigabyte. Some of the results from this CEWE are presented here, and are also made available in an online tool called TARA CEWE, `http://taracewe.ewi.tudelft.nl`, and can be used as an exploratory research tool to study dependencies between atmospheric variables. In this section, the focus is on the validation results of EDR retrieval techniques, which come from this massive data analysis effort.

The goal of the massive data analysis was to further validate the EDR retrieval techniques. One of the results of the TARA CEWE tool are one-to-one scatter density plots, which can be used for the comparison of remote with in situ measurements of wind and EDR. Here we start with a comparison of wind, which is a relatively simple atmospheric variable in comparison to EDR.

The one-to-one scatter density plots of 10 minute averaged 3D wind speed and wind direction are shown in Fig. 3.12. The correlation coefficients for the comparison of remote versus in situ values for wind speed and wind direction are very good, with deviations that are less than 5% from perfect (perfect one-to-one correlation values are $r_{xy} = 1$ and $r_{\theta\phi} = 1.41$.). Therefore, the comparison of

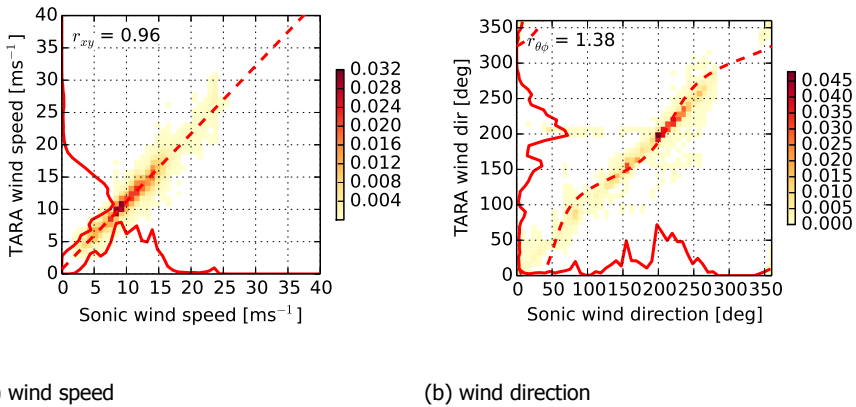(a) wind speed   (b) wind direction

Figure 3.12: Scatter density plot of (a) wind speed and (b) wind direction for 140 days in 2012. Relative occurrence is plotted in each pixel for the radar (y-axis) against the in situ sonic measurements (x-axis). On top of the axis the relative distribution is plotted, the correlation coefficient r_{xy} is printed and/or a measure of circular to circular variable dependence $r_{\theta\phi}$ (Mardia and Jupp 1999) is printed.

the remote measurements from TARA versus in situ measurements from the sonic anemometer placed at the tower at 180 m altitude went very well. This gives confidence that this comparison via a massive data analysis tool called CEWE can also be used for the validation of more complex atmospheric variables, such as EDR.

The comparison of remote against in situ EDR values is now repeated for 140 days in 2012. Previously, this comparison was done for just two case studies (Fig. 3.11). In Fig. 3.13 the result for the massive data analysis is shown. For the VWVV EDR retrieval technique almost no correlation is found ($r_{XY} = 0.20$), which is similar to what was found for the two case studies ($r_{XY} = -0.20$). For the WSV technique a good correlation is found (again) for the massive comparison ($r_{XY} = 0.58$), but the correlation is lower than for the two case studies ($r_{XY} = 0.79$).

The conclusions that were obtained for the two case studies are also thus valid for the larger dataset. The VWVV technique is not very promising, likely due to inaccurate raindrop-DSD-based terminal fall velocity corrections. The best agreement of TARA with the in situ EDR values is found for the WSV technique with a good correlation ($r_{XY} = 0.58$). A problem with the radar is that the EDR values are overestimated with about one order of magnitude. For future applications, such a bias can be removed by calibration that is based on (massive) data analysis or radar simulations. Further research would be required to estimate calibration factors for every remote instrument.

The in situ distributions of EDR values are interesting to study to get a better picture of biases, and potential problems with the retrieval techniques. For a small dataset, estimated distributions of EDR are typically spiky and only limited to a small range of EDR values. The two case studies are exemplary for this, where
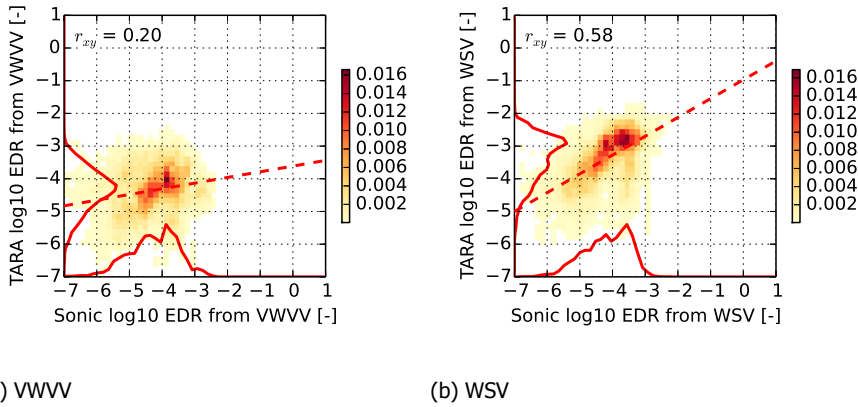
(a) VWVV   (b) WSV

Figure 3.13: Scatter density plot of EDR values obtained with (a) VWVV and (b) WSV retrieval techniques for 140 days in 2012. Relative occurrence is plotted in each pixel for the radar (y-axis) against the in situ sonic measurements (x-axis). On top of the axis the relative distribution is plotted and the correlation coefficient r_{xy} is printed.

EDR values were mostly between 10^{-4} and 10^{-3}, and the distributions are not so smooth (see Fig. 3.11). The advantage of using more data is that the estimated distributions of EDR values become wider and more continuous. For 140 days in 2012, in situ EDR values varied between 10^{-6} and 10^{-3}. Hence, the estimated distributions of EDR with the massive data effort will provide a much better picture regarding biases and potential problems with the EDR retrieval techniques.

The distributions of EDR values for all retrieval techniques with this massive data analysis are shown in Fig. 3.14. The distributions of in situ EDR values from the sonic anemometer are consistent for techniques that use the variance of 3D velocities (WSV), variance of vertical wind velocities (VWVV), or the second-order structure function (SSF). Here we take the distributions of these techniques as reference for comparison to other techniques. The power spectrum (PS) technique is biased with EDR values that are one order of magnitude higher, which can be associated with large errors that this technique has (See Fig. 3.9). All the in situ techniques are applied with a total sampling time of 10 minutes, except for the STWSV technique where the total sampling time is 5 seconds. The STWSV is biased with about one order of magnitude higher EDR values, which is due to the applied smaller total sampling time. The fact that the STWSV EDR values are biased with respect to the WSV values is an indication that the measurements are not in the inertial subrange. It suggests that the Kolmogorov -5/3 power law (Eq. 3.10) does not apply often to the short time scale of 5 seconds for the measurements in the boundary layer. This was also illustrated for some cases with averaged power spectra of in situ 3D wind speeds (Fig. 3.8).

If the Kolmogorov model is not always applicable, the concept of EDR has to be
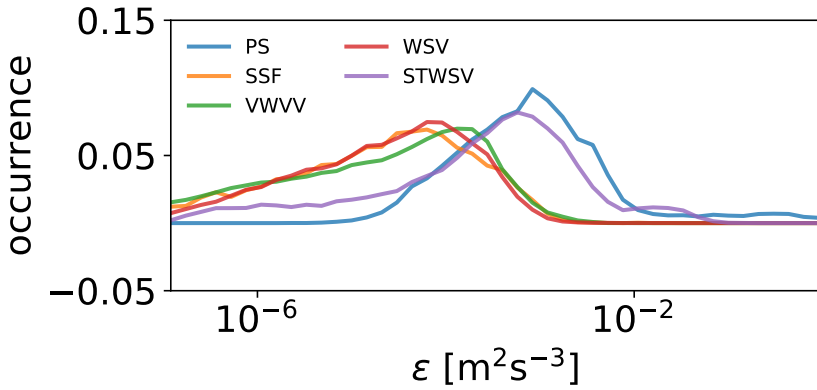
(a) in situ
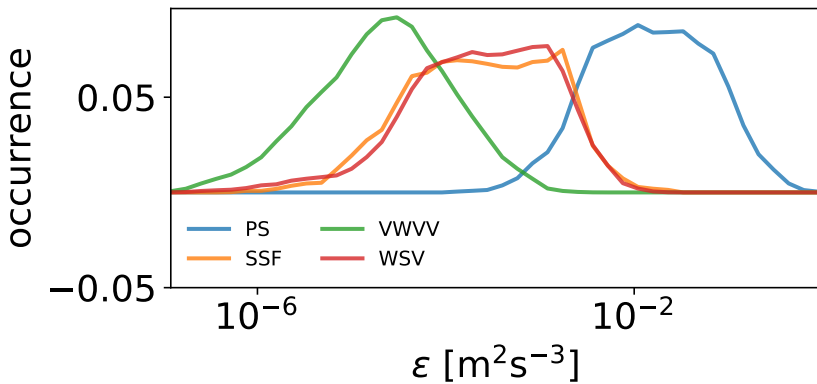
(b) remote

Figure 3.14: Distributions of EDR values for a set of retrieval techniques for (a) in situ from sonic anemometers and (b) remote measurements from TARA. Abbreviations of the EDR retrieval techniques can be found in Table 3.1.

applied cautiously. For example, this can be done by providing large uncertainties of EDR values when necessary, or by providing the length/time scales for which the estimated EDR value is relevant based on averaged power spectra from in situ measurements.

The next step is to look at the distributions of EDR retrieved with the radar, and the possibilities to explain them with what we learned so far from the two case studies. The distribution of EDR values retrieved with remote data from TARA are shown in Fig 3.14b. As for the in situ comparison of EDR value distributions, there is a set of consistent EDR retrieval techniques (WSV, SSF) and the PS technique is biased with too high values due to the large errors (again see Fig. 3.9). The

technique based on the variance of vertical velocities (VWVV) is biased with respect to the other techniques, which is due to inaccurate estimation of vertical velocities that were based on the rain DSD. From the retrieved distributions with TARA, it is apparent that values below 10^{-6} m^2 s^{-3} are almost never retrieved. This seems to be consistent with the fact there is a minimal retrievable EDR (Fig. 3.3).

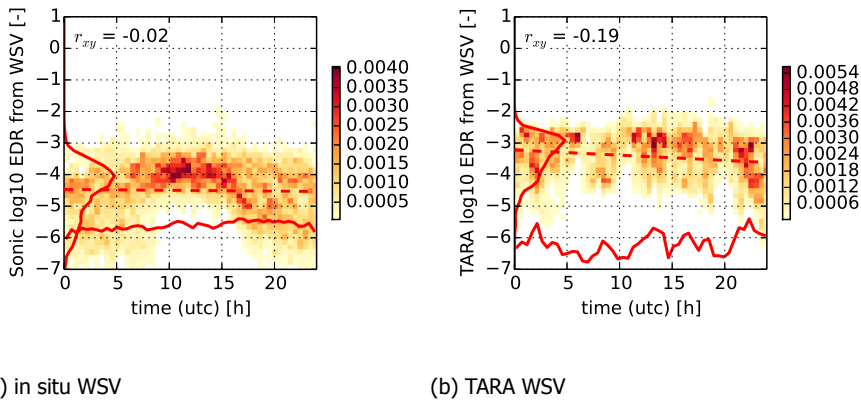(a) in situ WSV   (b) TARA WSV

Figure 3.15: Averaged daily pattern for one month, April 2012. Scatter density plots of EDR values versus time are plotted for (a) in situ WSV EDR, and (b) TARA WSV EDR.

With measurements that do no rely on the presence of raindrops, trust can be gained in the results by looking at the daily time evolution of EDR. For the two study cases in 2012, this was not possible because the radar data did not contain sufficiently long rain events. When radar data is abundant, a trick can be applied to get an idea of the daily pattern retrieved from raindrops, without having a single day where it rains the full day. The trick is to average the time pattern for one month of data. The result is shown in Fig. 3.15, which gives an impression of the evolution of EDR during a typical day. In Fig. 3.15a we see a typical day for the in situ measurements of EDR values: often low EDR values during the night and high EDR values during the day. In Fig. 3.15b we can see a similar pattern for the radar, but it is more vague. An obvious reason to explain this, is that the radar is limited in estimating low EDR values.

With the massive data analysis that was performed, it was found the WSV is the best EDR retrieval technique to be used with TARA during rain, based on a good correlation coefficient with in situ measurements from EDR. This confirms the conclusion from the two case studies, and demonstrates that this technique can be applied to all rainy cases in the Netherlands. By looking at distributions for a large dataset, it becomes clear which EDR retrieval techniques are consistent and which ones are problematic. A bias in retrieved EDR values can be corrected for and should, in principle, not be a problem. With further applications, care has to be taken when EDR values are estimated, because the measurements are not always

in the inertial range, and the radar is not capable of estimating very low EDR values, which is consistent with the results from Eq. 3.20 and Fig. 3.3.

3

3.5. **Conclusions**

In this chapter, the goal was to find the best EDR retrieval technique - from five typically applied EDR retrieval techniques - for the Doppler radar that is capable to measure EDR under rainy conditions. A correction for the raindrop terminal fall speed was applied. The best retrieval technique was determined by comparing retrieved EDR values based on estimated wind velocities from the TARA radar during rain and collocated EDR values from a sonic anemometer on a tower lever at 180 m altitude.

One concern with the retrieval of EDR values is whether the measurements are in the inertial subrange. To verify this, power spectra of 3D wind speeds from a sonic anemometer at 180 m altitude were analyzed, and with them it was demonstrated that there was always an inertial range of time scales between 10^2 and 10^3 s. For shorter time scales, boundary layer processes such as energy transport, surface friction or strong windshear, can lead to anisotropic turbulence, and thus implicate that the measurements are outside the inertial range. Therefore, the EDR retrieval techniques that use a time scale of 10 minutes in this work were applied in the inertial range. These techniques are: the wind speed variance (WSV) and the vertical wind velocity variance (VWVV) EDR retrieval techniques. For techniques that were applied at a shorter time scale or take a spectrum of times scales into account in this work EDR values could be biased, because they may be applied outside the inertial range. These techniques are: the power spectrum (PS), the second-order structure function (SSF) and the short time wind speed variance (STWSV) EDR retrieval techniques. The estimated uncertainty from the processing of 3D wind speed spectra (SSF, PS) can be useful for these cases, as it quantifies how well the measurements are in the inertial range.

Two rain events on 10 April 2012 and on 21 June 2012 were used to demonstrate and assess the EDR retrieval techniques. For these case studies, an agreement was found for EDR retrieval techniques (WSV, VWVV, SSF), when they were applied to the sonic anemometer. Other techniques were biased, likely due to large errors (PS), or the application to a short time scale (STWSV). When the EDR retrieval techniques are applied to Doppler velocity measurements from the radar during rain, more diversity appears in the retrieved results. A good correlation was found between remote EDR values and in situ EDR values for the WSV EDR retrieval technique, and is considered the best. The VWVV EDR retrieval technique, which is often applied to lidar and sonic anemometer measurements, is less effective for the radar during rain, because the radar-based estimated vertical velocities were not sufficiently accurate. Although the technique based on the SSF can be useful, in particular for a reliable uncertainty estimation that is based on a broad range of time scales, its application to Doppler radar measurements is limited because of incomplete time series due to noncontinuous beam filling.

With a massive data analysis it was possible to show that the conclusions for the two case studies are also valid for 140 days in 2012, and are thus representative for rainy weather in the Netherlands. A more detailed analysis was given with the large data analysis, by estimating distributions of retrieved EDR values and showing the EDR time evolution with daily averaged EDR patterns. The massive data analysis

revealed that there are biases in the EDR values that were estimated with the TARA radar, and also that this radar is limited in estimating very low EDR values.

For further applications to other Doppler radars during rain, it is recommended that the concept of EDR is applied cautiously. A minimal retrievable EDR should be estimated for the used instrument, and for each EDR value uncertainties should be provided. In addition, it is suggested to always provide the sampling and total sampling scales that were used in the EDR retrieval technique. Also, the estimation of energy spectra of 3D wind speeds is advised, which can be used to validate if the measurements were taken in the inertial range. With regard to the radar-based drop size distribution (DSD) estimation, not only the DSD parameters should be verified, but also the associated vertical velocities. Further, it is expected that these retrieval techniques can also be applied - with some modifications - to radar-based EDR retrievals during snow and hail. In all of the future studies, long-term and consistent observations of EDR are recommended, which leads to testing of the algorithms under sufficiently various weather conditions.

4

Model-based estimation of wind vector fields

This chapter starts with an assessment of the influence of raindrop inertia on radar-based retrieved wind vectors. Consequently, two wind vector retrieval techniques are described, which are the "linear wind model" and the "four-dimensional variational analysis (4D-Var)" techniques. The retrieved wind vectors from the linear wind model technique, which is commonly used, are used as a reference in this work. The proposed 4D-Var wind vector retrieval technique, where optimal estimation is used, has some advanced processing features. In a case study, the techniques are applied to one scan of IDRA radar measurements. By selecting extreme algorithm settings in 4D-Var, the solution space of wind fields can be shown that is associated with the measurements from a single Doppler scanning radar. In addition to these two techniques, a trial is made to retrieve wind vectors from the advection of the radar reflectivity pattern. The quality of the retrieved wind vectors from the different retrieval techniques are assessed by making a comparison of measures for curl and divergence as a function of range, and by a comparison of the standard deviation of residuals as a function of time.

"The invention of the light bulb has had more influence on the life of people than any philosophical work." - Steve Jobs.

4.1. Introduction

With a lidar or radar, the line-of-sight velocity, v_r, is measured using the Doppler-induced frequency shift on the backscattered signal, and is expressed by (e.g. Doviak and Zrnić 1993):

$$v_r = u \cos \gamma' \sin \alpha + v \cos \gamma' \cos \alpha + w \sin \gamma', \qquad (4.1)$$

where γ' is the elevation angle, α is the radar antenna azimuth looking angle, and (u, v, w) are the wind-components in an ENU Cartesian coordinate system (see Appendix A). Consequently, wind vectors can be reconstructed by model-based parameter estimation.

For the lidar, the Volume Velocity Processing (VVP) method is often used to obtain wind vectors (e.g. Kongara et al. 2012; Krishnamurthy et al. 2013). With the VVP method, a linear wind model is used for each analysis volume (e.g. Doviak and Zrnić 1993). The accuracy of the retrieved wind vectors depends on the number of measurement samples within an analysis volume, and the set of the fitted parameters. More samples will give a higher accuracy to averaged wind speeds. On the other hand, too much fitting parameters with insufficient samples can lead to unstable results. When these parameters are properly chosen, good validation results can be found, e.g. an accuracy of 0.06 m s^{-1} at 1.6 km range (Wagner and Courtney 2014).

For the radar, Eq. 4.1 also applies, but more challenges in the wind vector retrieval technique arise, due to the radar measurement principles. In comparison to a lidar, we can - generally speaking - state that the weather radar has a much wider beam and a larger range resolution, which is due to the nature of the used radar frequencies and the radar operating principles. Further, the scatterers for a weather radar are much larger than for a lidar. For the weather radar the scatterers are typically raindrops, snow/hail or insects, and for the lidar they are typically aerosols (small dust particles). All these mentioned features of a weather radar measurement have to be taken into account to obtain the most accurate result to retrieve a physical parameter. This includes the radar projection, the radar beam pattern, the pulse shape, range folding and the radar signal processing (see e.g. Fabry 2010).

One solution to enhance wind vector retrievals is by using multiple Doppler radars (e.g. Friedrich and Hagen 2004; Gao et al. 2001; Satoh and Wurman 2003). Also, often the mass continuity equation is used as a constraint in a fitting routine to obtain wind vectors (e.g. Bousquet and Chong 1998; Chong and Cosma 2000; Chong et al. 2000; Gao et al. 2004, 1999, 2001). This is only relevant when 3D wind vectors can be obtained, for example, with a single radar that scans both in the azimuthal and elevational directions, or by combining observations from multiple instruments. The adjustment of wind vectors to the continuity equation is sometimes seen as somewhat arbitrary, and is thus questioned in the literature (e.g. Chong and Testud 1983; Gao et al. 1999). On the scale of weather systems the mass continuity constraint is true, but on smaller scales, variations of air density can be very significant. In this work, the mass continuity constraint is not used.

Problems with wind vector retrieval techniques can exist when they are applied to the radar during rain, because: (1) rain/cloud drops are not perfect tracers of the air motion, and (2) data gaps exist in the scanning area. These two problems are addressed in this chapter, by analysis of the raindrop inertia effect on radar-based wind vector retrievals during rain, and by the development of advanced wind vector retrieval techniques. These wind vector retrieval techniques are tested on a single scanning Doppler radar, with no variation in the radar-antenna elevation looking angle for the retrieval of horizontal wind vector components. This is challenging, because the mass continuity equation can thus not be applied, and the wind vectors can not be retrieved by combining measurements from different looking directions.

In this chapter, it is investigated how to use Doppler measurements from a scanning radar to obtain a reliable and useful local wind field estimate at the scale of an airport. First, it is investigated what the influence of raindrop inertia is on radar-based wind vector retrievals during rain. Next, the linear wind model retrieval technique is applied to IDRA (Figueras i Ventura 2009; Otto and Russchenberg 2010) radar measurements. In order to compensate for the shortages of the linear wind model, the 4D-Var wind retrieval is introduced and is applied to the same IDRA radar measurements. With 4D-Var, the ambiguity of the wind vector fields that is associated with the measurements from a single scanning Doppler radar is shown. After that, an effort is made to validate the radar-based retrieved wind vectors. In the end, the conclusions are drawn.

4

4.2. Assessment of the influence of raindrop inertia on radar-based retrieved wind vectors

One might ask the question under what circumstances the influence of raindrop inertia is important for radar-based wind vector retrievals. In the case of a uniform wind field, raindrops will fall with the air velocity plus their terminal fall velocities, until they reach the surface. If the raindrop size distribution (DSD) is known, it is possible to correct for the terminal fall speeds of the raindrops, and obtain the air velocity in the radar line of sight. In the case of a non-uniform wind field, it becomes more complex. Two examples of these non-uniform wind fields are wind shear and a boundary-layer wind structure, for which the influence of raindrop inertia is simulated in this section.

In the simulations, raindrops with different sizes are used, and the difference in horizontal wind velocity of the raindrop with regarding to its surroundings is calculated for two theoretical case studies. This difference in horizontal wind velocity can be expected as the mass of the raindrop needs some time - while it is falling - to respond to changes in the surrounding motion. The most simple case study is vertical shear (change of the wind speed with altitude). A slightly more complex case study is an Ekman layer, which is a common boundary layer profile (e.g. Holton 2001), where both wind speed and wind direction are changing with altitude. In the theoretical case study simulations, the raindrop velocity is obtained by implicit integration of the relaxation velocity over a backward trajectory (details in §2.4).

The simulation results are presented in Fig. 4.1. In the case of an Ekman layer (e.g. Holton 2001) and raindrops of 4 mm, the raindrop inertia leads to a deviation between air and raindrop velocities of about 1.5 m s^{-1}. The deviations between air and raindrop velocities due to shear can be as much as 5 m s^{-1}. Note that such large deviations are only present for large raindrops and very strong shear in the simulation, which are raindrops of 4 mm (or larger) and changes of 10 m s^{-1} over 25 m in altitude (or more). For smaller droplets, it is demonstrated with these simulations that the influence of raindrop inertia is negligible on the scale of about 10 m or larger.

From these simulations, it is concluded that for most cases, the raindrop inertia effect for radar-based wind vector retrieval techniques is not important. Only for special conditions, such as very strong shear in combination with the presence of large raindrops, a substantial bias can be expected and should be corrected for. In this work, we are not considering study cases with such special conditions. Therefore, in this work no additional effort is made to correct for the influence of the raindrop inertia in wind vector retrieval techniques. It is part of future research how to account for the raindrop inertia effect, which is expected to be only relevant for special case studies.

One approach to account for the influence of raindrop inertia in wind vector retrieval techniques is to calculate the relaxation velocity term with a backward trajectory in an optimal estimation technique. The consequence of doing this is that the wind vector retrieval technique becomes much slower, because of the multiplicity of the extra calculations: For each raindrop size in a certain DSD, for each
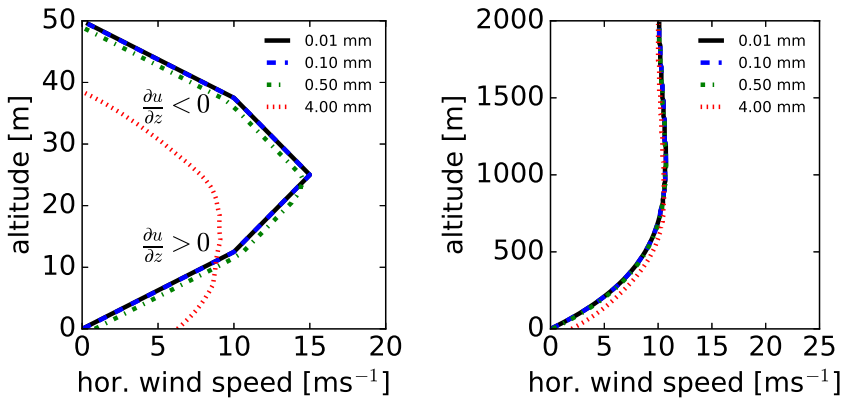
(a)

(b)
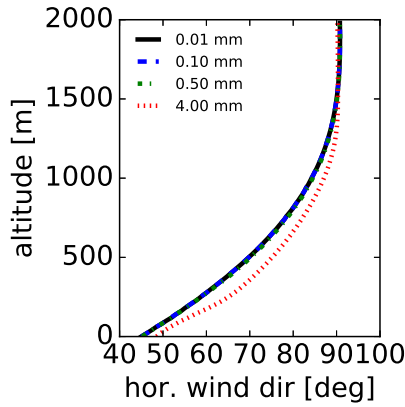
(c)

Figure 4.1: Simulation of the influence of raindrop inertia on vertical wind profiles. The horizontal wind speed and horizontal wind direction is calculated of raindrops for different equivolumetric raindrop sizes for: (a) vertical wind shear with some variation, and (b) - (c) a typical boundary layer profile (an Ekman layer).

measurement point in space, and for all backward trajectory points calculations have to be done, making such an approach a large and thus unattractive computational effort. This could be a good approach for some case studies where processing time is not an issue, but for general application an efficient approach is more desirable.

4.3. **Wind vector retrieval techniques**

In this section, two wind vector retrieval techniques are described that will be later applied to a scanning Doppler weather radar during rain for further analysis. First the linear wind model is described, which is a commonly used approach and taken as a reference in this work. And then the 4D-Var wind vector retrieval technique is explained, which is a novel approach that is based on optimal estimation.

The concept to obtain wind vectors from line-of-sight (LOS) velocities, or sometimes called radial velocities, which are obtained with a radar (or lidar) from backscattering targets via the Doppler effect, is to derive the wind velocity components by combining measurements from different antenna looking angles. The difficulties for when they are applied to radar measurements are that wind fields can be inhomogeneous and that the radar measurements typically contain data gaps. Let us look a little bit more into these difficulties.

For a homogeneous horizontal wind field, a harmonic series of LOS velocities is produced as a function of the antenna azimuth looking angle. In that case, the wind vector retrieval technique becomes relatively simple. The wind vector can be obtained with analytical formulas and by combining a few measurements from different looking angles, or alternatively by a least squares fit of radial velocities (e.g. Brown and Wood 2007; Doviak and Zrnić 1993). In reality, wind fields are rarely uniform over the large volumes surveyed by radars. For non-homogeneous wind fields, the difficulty is thus to obtain a wind vector field, including all its fluctuations, from remote LOS velocity measurements, and a more advanced wind vector retrieval technique is desired.

For the weather radar that is relying on tracers - e.g. raindrops, hail, snow, or insects - an additional challenge (with regards to a Doppler lidar) is the existence of data gaps due to inhomogeneous filling of the air with the weather radar scatterers (e.g. rain cells). It can be expected that the retrieved wind vectors will be biased when there are data gaps, and the question is then how to quantify which retrieval technique is performing the best. This question will be answered later with the study cases.

4.3.1. **Linear wind model**

In the linear wind model, the wind vector $\vec{v} = (u, v, w)^T$, at radial distance r, elevation angle γ and azimuth angle α, is assumed to be well represented by a first-order Taylor series in a small region, a so-called analysis volume, around the point (x_0, y_0, z_0), the center of the analysis volume:

$$\vec{v}(x, y, z) = \vec{v}(x_0, y_0, z_0) + \frac{\partial \vec{v}}{\partial x}(x - x_0) + \frac{\partial \vec{v}}{\partial y}(y - y_0) + \frac{\partial \vec{v}}{\partial z}(z - z_0). \tag{4.2}$$

Here the ENU coordinate system is used to uniquely determine the position of points in space (see Appendix A).

In the following parts, the estimated variables are indicated with a hat (ˆ) and the physical parameters are put in a mathematical vector $\mathbf{K}$. A projection vector $\mathbf{P_r}$ is used to convert the parameters to the estimated variable. For the linear wind model, $\mathbf{P_r}$ and $\mathbf{K}$ are vectors, and the mathematical dot product is used to get the

result. The modeled radial Doppler velocity $\hat{v}_r$ can then be written as:

$$\hat{v}_r(r, \gamma', \alpha) = \mathbf{P_r} \cdot \mathbf{K}, \tag{4.3}$$

and the horizontal wind components as:

$$\hat{u}(x, y, z) = \mathbf{P_u} \cdot \mathbf{K}, \tag{4.4}$$
$$\hat{v}(x, y, z) = \mathbf{P_v} \cdot \mathbf{K}. \tag{4.5}$$

Here $\mathbf{P_r}$, $\mathbf{P_u}$, and $\mathbf{P_v}$ are the projection vectors for $\hat{v}_r$, $\hat{u}$ and $\hat{v}$ respectively, and $\mathbf{K}$ is the parameter vector. The terms in these expressions are:

$$\mathbf{P_r} = \begin{pmatrix} \cos\gamma' \sin\alpha \\ \cos\gamma' \sin\alpha(x - x_0) \\ \cos\gamma' \sin\alpha(z - z_0) \\ \cos\gamma' \cos\alpha \\ \cos\gamma' \cos\alpha(y - y_0) \\ \cos\gamma' \cos\alpha(z - z_0) \\ \cos\gamma' \left[r\cos\gamma' \sin\alpha\cos\alpha - \frac{1}{2}(x_0\cos\alpha + y_0\sin\alpha) \right] \\ \sin\gamma' \\ \sin\gamma'(x - x_0) \\ \sin\gamma'(y - y_0) \\ \sin\gamma'(z - z_0) \end{pmatrix}, \tag{4.6}$$

$$\mathbf{P_u} = (\quad 1., \ x - x_0, \ 0., \ 0., \ 0., \ 0., \ \tfrac{1}{2}(y - y_0), \quad 0., \ 0., \ 0., \ 0. \ )^T, \tag{4.7}$$

$$\mathbf{P_v} = (\quad 0., \ 0., \ 0., \ 1., \ y - y_0,, \ 0., \ \tfrac{1}{2}(x - x_0), \quad 0., \ 0., \ 0., \ 0. \ )^T \tag{4.8}$$

and

$$\mathbf{K} = (\quad u_0, \ u_x, \ u_z, \ v_0, \ v_y, \ v_z, \ (u_y + v_x), \quad w_0, \ w_x, \ w_y, \ w_z \ )^T, \tag{4.9}$$

where these formulas have been adapted from Doviak and Zrnić (1993). Here γ' is the radar antenna elevation looking angle and α is the radar antenna azimuth looking angle. And $\vec{v}(x_0, y_0, z_0) = (u_0, v_0, w_0)$ is the velocity at the center of the analysis volume, and u_x is the scalar parameter for the x-derivative of the u velocity component, and the same holds true for all the other components.

The goal is thus to find all these parameters, and they can be obtained with a least squares fit minimization of the χ^2 function:

$$\chi^2 = \sum_i \left(\frac{\mathbf{P}_{r,i} \cdot \mathbf{K} - v_{r,i}}{\sigma_{v,r,i}} \right)^2, \tag{4.10}$$

where $v_{r,i}$ is the measured Doppler velocity for measurement i with uncertainty $\sigma_{v,r,i}$.

Simplification to other linear wind models

The linear wind model is a generalization of several wind vector retrieval techniques (Doviak and Zrnić 1993). Because of the mathematical formulation, this might be hard to see. To illustrate this, we give here an example of reducing the linear wind model to a more simple wind vector retrieval algorithm. Here just two radar Doppler measurements are used to calculate the horizontal wind components. In such a case, the vertical wind component w is neglected, and we can write the modeled LOS radar Doppler velocity as:

$$v_r = u_0 \cos \gamma' \sin \alpha + v_0 \cos \gamma' \cos \alpha. \tag{4.11}$$

Given this linear equation, just two measurements, with different azimuth looking angles, are sufficient to solve for the horizontal wind components, u_0 and v_0. When we are given just two such radial velocity measurements v_{r1} and v_{r2}, we can obtain u and v via:

$$u_0 = \frac{\cos \gamma_2' \cos \alpha_2 v_{r1} - \cos \gamma_1' \cos \alpha_1 v_{r2}}{\cos \gamma_1' \sin \alpha_1 \cos \gamma_2' \cos \alpha_2 - \gamma_1' \cos \alpha_1 \cos \gamma_2' \sin \alpha_2}, \tag{4.12}$$

$$v_0 = \frac{\cos \gamma_1' \sin \alpha_1 v_{r2} - \cos \gamma_2' \sin \alpha_2 v_{r1}}{\cos \gamma_1' \sin \alpha_1 \cos \gamma_2' \cos \alpha_2 - \cos \gamma_1' \cos \alpha_1 \cos \gamma_2' \sin \alpha_2}. \tag{4.13}$$

In addition to this example, there exists more formulations and variations of the linear wind model (Doviak and Zrnić 1993). They can be regarded as a subset of this general formulation, where a subset of all the parameters is solved for. In the way that the linear wind model is formulated here, it can be simplified to such simpler models, by using a subset of the full list of parameters in **K**.

Further details

In the linear wind model, the analysis volume size has to be chosen, which results in the number of measurements that are used in the least square fit to retrieve the wind vector field parameters. The combination of the number of fitted parameters in **K**, the number of measurements, and the quality of the measurements (noise and variation in looking angles) determine how good and stable the retrieved wind vectors become. Typically, a satisfying solution is found by using different parameters with trail and error.

Another common problem is that a small analysis volume contains too little information on the global wind field, with the consequence of fitting a random direction and/or random wind speed. A simple solution to this problem - that is also used in this work - is to add a few additional Doppler measurements from a larger analysis volume to the least squares fit to stabilize the retrieved wind vectors.

4.3.2. 4D-Var

Here we propose the four-dimensional variational assimilation (4D-Var), for the retrieval of the local wind field with radar Doppler measurements (Oude Nijhuis et al. 2014a), with the goal to retrieve reliable and realistic wind vectors. This 4D-Var wind vector retrieval technique is inspired by 4D-Var techniques, which are

typically used in numerical weather models, like ECMWF (Bouttier and Kelly 2003; Kopken et al. 2003), and optimal estimation techniques in general, such as ozone profile retrievals from hyperspectral radiances (Liu et al. 2010).

4D-Var is a model-based retrieval technique for parameter estimation. Some recognized advantages of 4D-Var and optimal estimation techniques are: 1) the time variation can be taken into account, with the consequence that the parameters of interest can be estimated in a more optimal way, and more measurements can be assimilated at once, and 2) prior errors and correlation lengths of wind vector components can be taken into account.

In this work, we propose to see the pattern in the wind field fluctuations as an advected field, and to see the pattern in the radar reflectivity field as an advected pattern as well. The wind fluctuations patterns are conserved with time and advected with the flow.

Here we use the meteorological wind direction, Θ, and horizontal wind speed, H, which are defined in terms of the horizontal wind components u and v as:

$$u = -H \sin(\Theta), \tag{4.14}$$
$$v = -H \cos(\Theta). \tag{4.15}$$

Both formulations, (u, v) and (H, Θ), are used in this work, depending on which ones gives the most convenient expressions.

The geostrophic wind is generally a good approximation for the time-evolution of wind vectors in extratropical synoptic-scale disturbances, except for some extraordinary cases (Holton 2001). The time evolution of the horizontal wind direction can then be approximated as:

$$\Theta(t) = \Theta(0) + ft, \tag{4.16}$$

where $f = 2\Omega \sin \phi$ is the Coriolis parameter, Ω is the rotation rate of the Earth, and ϕ is the latitude. The combination of advection and geostrophic evolution of the wind field can then be written as:

$$u(x, y, z, t) = u(x(t), y(t), z(t)) \cos(ft) + v(x(t), y(t), z(t)) \sin(ft), \tag{4.17}$$
$$v(x, y, z, t) = -u(x(t), y(t), z(t)) \sin(ft) + v(x(t), y(t), z(t)) \cos(ft), \tag{4.18}$$
$$w(x, y, z, t) = w(x(t), y(t), z(t)), \tag{4.19}$$
$$L(x, y, z, t) = L(x(t), y(t), z(t)), \tag{4.20}$$

where u, v, w are the wind components, and L is the liquid water content (LWC). The LWC variable is used here to match simulated radar reflectivities with the measured radar reflectivities. Note that the LWC is only relevant for the retrieval of wind vectors via the advection of the radar reflectivity pattern.

The displacement of the advected fields is given by:

$$x(t) = \int_0^t u(t')dt' = \sum_i \frac{H}{f} \left[\cos(\Theta + f\Delta t_i) - \cos(\Theta)\right], \tag{4.21}$$

$$y(t) = \int_0^t v(t')dt' = \sum_i \frac{-H}{f} \left[\sin(\Theta + f\Delta t_i) - \sin(\Theta)\right], \tag{4.22}$$

$$z(t) = \int_0^t w(t')dt' = \sum_i w\Delta t_i. \tag{4.23}$$

The right-hand side formulations are small steps of the integration, which are used in the 4D-Var wind vector retrieval technique.

The wind field components and the liquid water content field are saved on 3D grids, representing the state of the fields at a reference time (for convenience $t = 0$). The 3D grids are used to simulate the measurements by using bilinear interpolation and the forward time operator described above. The 3D grid point values are stored in the parameter vector $\mathbf{K}$, which is used in the cost function.

Using 3D grids makes this approach versatile, and depending on the application, a degenerated grid can be used. For example, for a profiling radar the grid can be reduced to a vertical profile (just one point for all x and y-locations). Or in the case of a scanning radar with a fixed low antenna elevation looking angle, the 3D grid can be reduced to a horizontal 2D grid.

In the case of a $10 \times 10 \times 10$ field, the components of $\mathbf{K}$ are :

$$\mathbf{K_u} = (u_{0,0,0}, \cdots, u_{10,10,10})^T \tag{4.24}$$
$$\vdots \qquad \vdots \qquad \vdots$$
$$\mathbf{K_L} = (L_{0,0,0}, \cdots, L_{10,10,10})^T.$$

And the full parameter vector is:

$$\mathbf{K} = (\mathbf{K_u}, \mathbf{K_v}, \mathbf{K_w}, \mathbf{K_L}). \tag{4.25}$$

For the 4D-Var model, $\mathbf{P_r}$ is a projection operator and is representative for a mathematical procedure that integrates the grid parameters over the radar cell to obtain an estimated variable. The modeled Doppler mean velocity estimate $\hat{v}_r$, and the radar reflectivity estimate, $\hat{Z}$, are then calculated as:

$$\hat{v}_r(x, y, z, t) = \mathbf{P_r}(x, y, z, t)\mathbf{K}, \tag{4.26}$$
$$\hat{Z}(x, y, z, t) = \mathbf{P_Z}(x, y, z, t)\mathbf{K}, \tag{4.27}$$

where $\mathbf{P_Z}$ and $\mathbf{P_r}$ are the projection operators for the radar reflectivity and the Doppler velocity respectively.

In this work, the Zephyros tool is used to calculate radar observables from the parameters (Oude Nijhuis 2017), and thus takes care of the spatial interpolation and integration, and takes into account the radar characteristics. All the wind vector retrieval techniques are implemented in *Zephyros*, which is a tool for the development

of radar-based retrieval techniques of wind vectors and turbulence intensity, and can be downloaded from GitHub. A few more details regarding spatial interpolation and turbulence models are discussed later in chapter 5.

4D-Var with radial velocity measurements

The wind field is retrieved by minimization of a cost function χ^2. In the case that wind vectors are fitted from the radar Doppler velocities, the cost function is written as:

$$\chi^2_{v,r} = \sum_i \left(\frac{\mathbf{P_{r,i}K} - v_{r,i}}{\sigma_{v,r,i}} \right)^2 + (\mathbf{K} - \mathbf{K_p})^T \mathbf{S_p}^{-1} (\mathbf{K} - \mathbf{K_p}), \tag{4.28}$$

where $\sigma_{v,r,i}$ is the uncertainty of the Doppler velocity $v_{r,i}$ for the i-th measurement. The first term in the right side of 4.28 compares measured Doppler velocities to modeled velocities. The second term in the right side of 4.28 compares the parameters of the current state of the fit $\mathbf{K}$ with the prior parameters $\mathbf{K_p}$. The prior parameters $\mathbf{K_p}$ can come from other models/measurements/fitting routines to find a solution that matches with that, or they can be filled with some best guesses with large uncertainties forcing the solution to a realistic solution, or they can be completely ignored by setting the parameter uncertainties to infinity. In this cost function the parameters consist only of the wind field velocity components, which are used to estimate the radar line-of-sight velocities. In this equation, $\mathbf{S_p}$ is the error covariance matrix of the parameters. More details with regard to fitting via optimal estimation can be found in e.g. Rodgers (2000).

4D-Var with radar reflectivity measurements

Another approach to retrieve wind vectors from radar measurements, is to use the motion of the radar reflectivity pattern, which are representing the advection of rain cells. The concept behind it is that the wind vector field can be estimated from the motion of rain cells, which are measured as a radar reflectivity pattern. Here we also use 4D-Var to achieve this, where a series of radar reflectivity scans are fitted with a cost function χ^2_Z:

$$\chi^2_Z = \sum_i \left(\frac{\mathbf{P_{Z,i}K} - Z_i}{\sigma_{Z,i}} \right)^2 + (\mathbf{K} - \mathbf{K_p})^T \mathbf{S_p}^{-1} (\mathbf{K} - \mathbf{K_p}). \tag{4.29}$$

In Eq. 4.29, the first term of the right-hand side compares the measured radar reflectivities Z_i with the modeled radar reflectivities $\mathbf{P_{Z,i}K}$, and the second term compares the parameters with the prior parameters.

For this wind vector retrieval technique, the radar reflectivity is matched in the cost function by varying the total liquid water content $\mathbf{L}$. Note that the drop-size-distribution shape is irrelevant here, because only the radar reflectivity is used. The cost function compares thus the difference in the radar reflectivity $\mathbf{P_{Z,i}K} - Z_i$, with a given uncertainty in the radar reflectivity $\sigma_{Z,i}$ for each measurement i.

Further details

The prior error covariance matrices, $\mathbf{S}_*$, are calculated for grid point i and j by:

$$S_{*,i,j} = \sigma_{*,i}\sigma_{*,j}\exp\left(-\left(d_{i,j}/L_d\right)^2\right),\qquad(4.30)$$

where $d_{i,j}$ is the spatial distance between points i and j, $\sigma_{*,i}$ is the prior parameter error estimate at grid point i, and L_d is the correlation distance (see e.g. Rodgers 2000). The size of prior parameter error estimates $\sigma_{*,i}$ determines how much the prior parameters are taken into account in the optimal estimation procedure. The effect of the prior parameter errors can be well understood by considering some extreme values. In the case of very large prior parameter errors, the prior parameters are neglected, and only the measurements will be effectively used in the search routine. In the case of very small prior parameters errors, the measurements will be effectively ignored, and the search routine will converge to the prior parameters. In the 4D-Var retrieval technique, the concept is to achieve reliable wind vectors by having an optimal balance for a best fit to the local measurements and a best guess in the beginning.

A nice feature of the prior errors is that the outcome can be somewhat pushed in a certain direction by choosing some extreme values for the prior errors. In the 4D-Var implementation, it is also possible to fit the horizontal wind speed and horizontal wind direction as grid parameters (as an alternative to using u and v). By setting one prior error of these variables to very large and one to very small, the outcome can be controlled and pushed in a certain direction. With this trick, the "horizontal wind-direction" and the "horizontal wind speed" solutions are obtained.

The implementation is optimized by using sparse matrices in the calculations for the error covariance matrices in the cost function. Further, also optimized code for the minimization of cost functions is exploited (Davis 2006; Johnson 2017; Vlcek and Luksan 2006).

4.4. Uncertainty estimation

Here a method is given on how to estimate the radar measurement uncertainties, and from that the posterior parameter uncertainties. The posterior parameter uncertainties are important, if one is interested in the reliability of the retrieved wind vectors.

For retrieved wind vectors from radar Doppler measurements, the estimation of posterior errors is not trivial. There is abundant information in the radar Doppler measurements for the component of velocity in the radar line of sight, but there is little information on the component of velocity in the directions perpendicular to the radar line of sight. As a consequence, with modern weather radars that have a high spatial resolution, the retrieved wind vectors are not necessarily very accurate at the same high spatial resolution. The difficulty is that within a small volumetric area the measurements have approximately the same radar looking directions. The solution proposed here is then to give a fair estimate for the uncertainty in the retrieved wind vector.

The range dependence of the radar reflectivity uncertainty for volumetric scatterers, σ_Z, can be expressed as a function of range r:

$$\sigma_Z = \alpha_0 \left(\frac{r}{r_0}\right)^2, \tag{4.31}$$

given the uncertainty in radar reflectivity error α_0 at range r_0. Here attenuation effects are not taken into account, and the variables are on a linear scale (not on a logarithm scale). The uncertainty in the radar Doppler velocity is then estimated as (Doviak and Zrnić 1993):

$$\sigma_{v,r} = \sqrt{\frac{v_d^2}{L_p}\left[\frac{\sigma_{vn}}{4\sqrt{\pi}} + 2\sigma_{vn}^2\frac{\sigma_Z}{Z} + \frac{1}{12}\left(\frac{\sigma_Z}{Z}\right)^2\right]}, \tag{4.32}$$

$$\sigma_{vn} = \frac{\sigma_{sp}}{2v_{max}} \quad , \quad v_d = \frac{\lambda}{2L_pT_s} \quad , \tag{4.33}$$

where L_p is the number of pulses, T_s is the sampling time interval, v_d is the Doppler resolution, v_{max} is the maximum unambiguous Doppler velocity, σ_{sp} is the measured Doppler spectral width, and σ_{vn} is the normalized Doppler spectral width.

It would make sense to use this uncertainty in radar Doppler velocity $\sigma_{v,r}$ in a wind vector retrieval technique, and using measurements weighted as $1/\sigma_{v,r}^2$ (see Eq. 4.10 and Eq. 4.28). After all a larger weight should be given to measurements where the radar is more sensitive. However, typically the uncertainty in the radar Doppler velocity estimated with Eq. 4.32 is quite small compared to the radial velocity model error. This model error comes from the fact that in a small analysis volume there are a lot of radial velocity measurements with similar antenna looking directions. Using a high number of windfield grid points is not a real solution, as there is too little information on the velocity components perpendicular to the line-of-sight measurements. This solution would lead to a very good fit, but with random wind vectors.

A better approach is to allow for a small model error, but having a stable solution for the retrieved wind vectors. It is then important to estimate this model error, which is a measure of the difference between the fitted and measured radial velocities, without any constraints due to prior parameters. Alternatively speaking, the model error gives an estimate for how well the model can fit the measurements.

Here we give a general method for how to estimate a model error after minimization of a cost function where modeled measurements $\hat{y}_i$ have been compared to measurements y_i. In the wind vector retrieval technique, this is used to estimate a radial velocity model error. This estimated model error can then be taken into account for an accurate posterior error estimation of the retrieved wind vectors.

For each measurement y_i, a residual can be calculated as:

$$r_i = y_i - \hat{y}_i. \tag{4.34}$$

The residual uncertainty, $\sigma_{y,r,i}$, for measurement y can be written as:

$$\sigma_{y,r,i}^2 = \sigma_{y,o,i}^2 + \sigma_{y,m}^2, \tag{4.35}$$

where $\sigma_{y,o,i}$ is the observational error (e.g. 4.32), and $\sigma_{y,m}$ the model error, due to simplification and smoothing. The model error can then be estimated from the residuals as:

$$\sigma_{y,m}^2 = \sum_i w_{y,o,i} \max\left[0, (y_i - \hat{y}_i)^2 - \sigma_{y,o,i}^2\right] \quad \text{with} \quad w_{y,o,i} = \frac{1}{\sigma_{y,o,i}^2} / \sum_i \frac{1}{\sigma_{y,o,i}^2} \quad ,$$

(4.36)

where $w_{y,o,i}$ are the weights. The covariance matrix of the residual errors, $S_{r,y}$, which include both observational and modeling errors, is a diagonal matrix, and the elements are given by:

$$S_{r,y,ii} = \sigma_{y,r,i}^2.$$

(4.37)

The posterior parameter covariance matrix can then be computed from

$$\mathbf{S_p} = [\mathbf{J}^T \mathbf{S_{r,y}}^{-1} \mathbf{J} + \mathbf{S_a}]^{-1},$$

(4.38)

where $\mathbf{J}$ is the Jacobian matrix, with derivatives $J_{ij} = \partial \hat{y}_i / \partial p_j$, and the a prior covariance matrix is given by $\mathbf{S_a}$. The standard parameter errors are the square root diagonal elements of this matrix.

4.5. Case study

In this section, first a small overview is given of the case study details and the used implementations. Consequently, with 4D-Var the solution space of wind vectors is shown that is associated with measurements from a single scanning Doppler radar. Then an attempt is made to retrieve wind vectors from the motion of the radar reflectivity pattern. Finally, the retrieved wind vectors from different implementations are compared quantitatively in a novel way by measures for curl, divergence and standard deviation of the residuals.

For this case study, measurements from the IRCTR Drizzle RAdar (IDRA) (Figueras i Ventura 2009; Otto and Russchenberg 2010) are used. IDRA is a horizontal scanning X band radar (zero elevation looking angle), on top of a 200 m meteorological research mast, located at a meteorological supersite in Cabauw (Casso-Torralba et al. 2008; Ulden and Wieringa 1996). The IDRA radar makes a full horizontal scan about every minute.

IDRA measurements are used from June 21th 2012, from 18:30 UTC and onwards. On this day, a cold front was passing over that brings in the rain. Only 10% of the radar data is used, where in the range direction 9/10 measurements are skipped for processing. This data reduction allows for fast processing and thus more algorithm testing. The resulting range resolution is then 300 m, and the azimuthal resolution is 2.5 °.

All the implementations (wind vector retrieval technique + configuration) that are being tested in this case study are:

1. Linear wind model

2. 4D-Var simple

3. 4D-Var horizontal wind speed

4. 4D-Var horizontal wind direction

5. 4D-Var neutral

6. 4D-Var advection

For all of these implementations a grid box of 4 x 4 km^2 is used (analysis volumes for the linear wind model), except for the 4D-Var simple retrieval technique, where just one single point is used. In the application of these wind vector retrieval techniques, different time windows have been used for the data assimilation: either 1 or 5 minutes, where each minute contains about one radar scan.

4

Linear wind model implementation details
For the linear wind model implementation, the parameters $(u_0, u_x, u_z, v_0, v_y, v_z, u_y + v_x, w_0)$ are fitted via a least squares method for each analysis volume using Eq. 4.10. The radar measurement uncertainties (Eq. 4.32) are not taken into account, as the combination of fitting derivative components and uncertainties with radar-range dependencies lead to unstable fitting. To stabilize the linear wind model fit, extra Doppler measurements are added from outside the analysis volume, which are randomly selected. Increasing the number of these extra measurements, pushes the solution to a more homogeneous solution. And decreasing this number will push the solution towards unrealistic results. For the case studies, 50 extra Doppler measurements are added.

4D-Var implementation details
For the 4D-Var implementation, it is possible to use a prior wind field. This prior wind field is obtained, by applying the "4D-Var simple" retrieval technique, that fits just one wind vector to all the radar Doppler measurements. Consequently, the "4D-Var simple" solution is casted to a finer 2D grid, for a second minimization round to estimate the wind vectors, which results in the "4D-Var neutral" wind vector field solution.

To get an idea of all possible wind vector field solutions, the 4D-Var neutral wind vector retrieval technique is applied but with one essential difference. The difference is that extreme a priori errors are used that either fixes the horizontal wind direction or the horizontal wind speed. As a consequence, the solution that is obtained with the cost function has the fluctuations in the non-fixed parameter (either horizontal wind direction or horizontal wind speed). Two solutions are made in this manner. The "4D-Var horizontal speed" solution, where a large a priori horizontal speed error and a small a priori horizontal direction error is used. And the "4D-Var horizontal wind direction" solution, in which the roles of horizontal wind direction and horizontal wind speed are reversed. With these solutions, it is possible to get an impression of the solution space of wind vectors that is associated with the radar Doppler measurements.

Next to these implementations, a trial is made to retrieve wind vectors from the evolution of the radar reflectivity pattern during multiple scans, which is called the "4D-Var advection" solution.

First impression: a qualitative comparison

In Fig. 4.2, the retrieved wind vectors from the linear wind model, and from the 4D-Var neutral implementation are shown. At short distance from the radar the
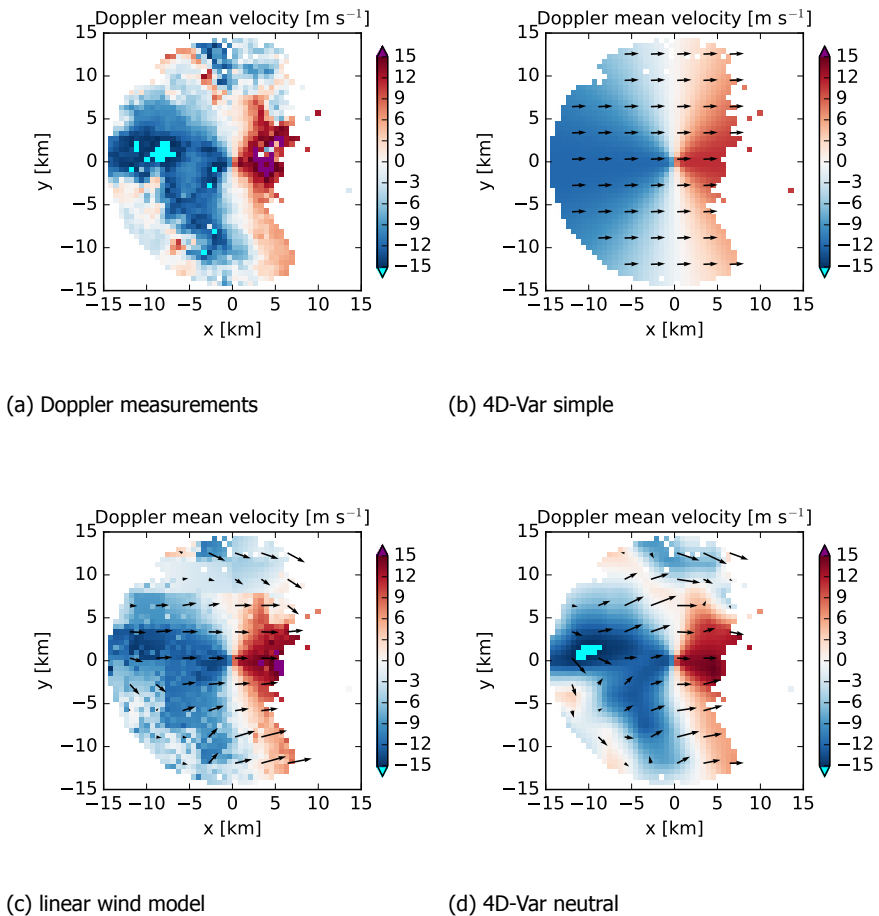

(a) Doppler measurements

(b) 4D-Var simple

(c) linear wind model

(d) 4D-Var neutral

Figure 4.2: Wind vectors retrieved from one scan from IDRA. In (a) the measured Doppler velocities are shown. Results for three wind vector retrieval techniques are shown, which are: (b) 4D-Var simple, (c) the linear wind model, and (d) the 4D-Var neutral. In these figures and all other figures in this work, a positive Doppler velocity is in the direction away from the radar location.

solutions are similar. At larger distance from the radar, there is more variation in

the retrieved wind vectors. Two artifacts can be recognized in the results from the linear wind mode, which are typical for retrieved wind vectors from radar Doppler measurements: (1) In the direction perpendicular to the radar beam the retrieved wind velocity becomes somewhat random (to fit the radar measurements), and (2) there are unrealistic jumps in the wind vector field, which can be associated with the edges of the analysis volumes in the linear wind model retrieval technique.
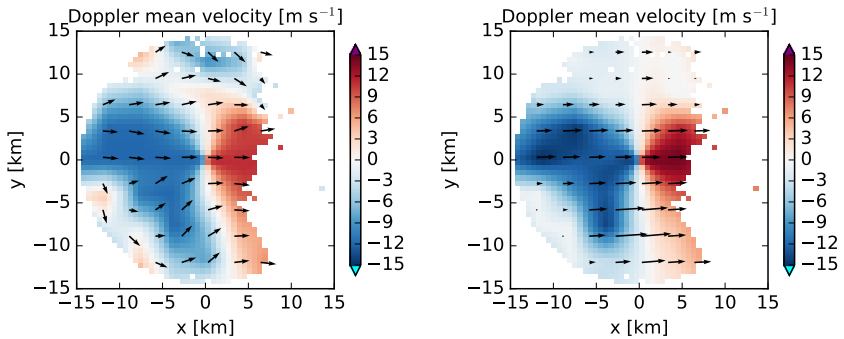
Solution space of wind vectors
In Fig. 4.3, wind vectors retrieved with the 4D-Var horizontal speed and the 4D-Var horizontal direction are shown. The wind vectors from the 4D-Var horizontal speed solution have almost no variation in the horizontal wind direction, and the wind vectors from the 4D-Var horizontal direction have almost no variation in the horizontal wind speed. This is what we were aiming for with these implementations. Despite that the retrieved wind vectors are different, the modeled Doppler velocities match the measured radar Doppler velocities. Therefore, the solution space of wind vectors is indeed demonstrated, for radar Doppler measurements from a single scanning Doppler radar.

The two solutions, with extreme settings in the prior errors, give thus an impression of all the possible solutions of wind vectors, that can be retrieved for the same radar Doppler measurements, from one scan from a horizontal scanning radar. Based on these images, an impression can be obtained on how reliable wind vector retrieval techniques are for a given dataset and a certain radar configuration. These images and this information can then be used to strategize about the best usage of radar measurements, and how to optimize the configuration of the wind vector retrieval technique.
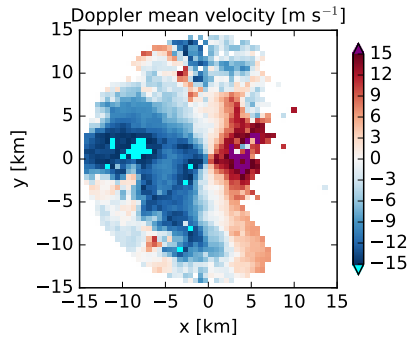
(a) Doppler measurements


(b) 4D-Var horizontal direction   (c) 4D-Var horizontal speed

Figure 4.3: Illustration of the solution space of wind vectors that is associated with single scanning Doppler radar measurements. In (a) the measured Doppler velocities are shown, and two solutions are shown that use one scan of IDRA Doppler measurements, which are: (b) the 4D-Var horizontal direction, and (c) the 4D-Var horizontal speed. Note that the radar reflectivity measurements for this study case is shown in Fig. 4.4.

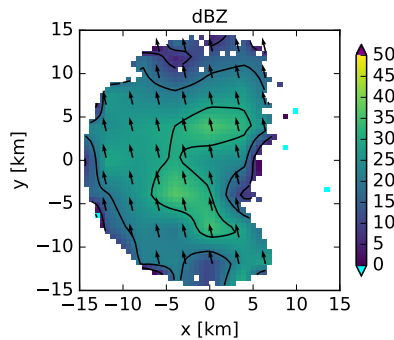**Wind vectors from the advection of radar reflectivity**

When one sees a pattern moving through a scanning radar, one might get the idea to use this as an estimator for wind vectors. This concept is the basis for the "4D-Var advection" implementation, which is an experimental variation of the 4D-Var retrieval technique.

Here we use 5 consequent scans from IDRA to estimate wind vectors from the moving radar reflectivity pattern. Two of such scans are shown in Fig. 4.4. Contours are drawn in this figure to show where the rain cells are located. It can be seen that the rain cells are moving in the northerly direction.
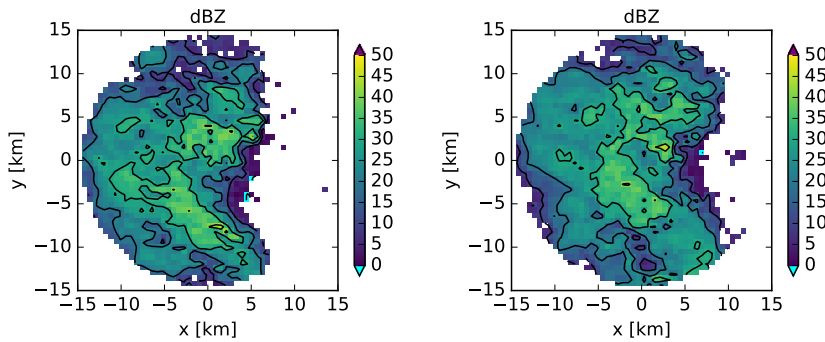
(a) Doppler measurements at 18:31   (b) Doppler measurements at 18:35

(c) 4D-Var advection

Figure 4.4: Illustration of wind vectors that are retrieved from the advection of a radar reflectivity pattern. In (a) the measured Doppler reflectivities are plotted at 18:31 and in (a) at 18:35. In (c) the fitted radar reflectivity pattern at 18:35 is shown, with the 4D-Var advection, including the estimated wind vectors.

The 4D-Var advection implementation is composed of two steps in which Eq. 4.29 is fitted via optimal estimation: (1) the radar reflectivity pattern is fitted and (2) both the reflectivity pattern and a wind vector are fitted. The wind advection vector is thus retrieved from matching a series of radar reflectivity patterns to a modeled radar reflectivity pattern that moves with the advection vector.

In contrast to the time it takes to find a solution for the cost function in the other 4D-Var retrieval techniques (a few minutes on a desktop computer), the 4D-Var advection retrieval technique takes much more time (about 10 minutes). This is likely caused by the fact that the optimization is less linear, as in the last step the reflectivity pattern and the motion are fitted simultaneous. This is consistent with the fact that the convergence towards a solution of a non-linear (cost) function takes more time. In this implementation, just one wind vector is retrieved and not a field of wind vectors. One wind vector is not a very impressive or realistic result, but it gives a first impression of this wind vector retrieval technique, and whether it can be expected to be promising in further developments.

The result for 4D-Var advection is shown in Fig. 4.4c. The most remarkable thing about the retrieved wind vector from the advection is that it has a different wind direction than all the other solutions, which are retrieved from the radar Doppler measurements (see Fig. 4.2). At first, this is quite a surprising result!

It can after all be explained. For this case study, shear in the vertical was observed by a balloon-borne sonde measurement of the wind profile from KNMI. Alternatively said: the wind direction at higher altitudes was different than close to the surface, which is not uncommon in the case of rain. Although the radar reflectivity and the radar Doppler measurements are coming from the same location, the reflectivity pattern of the scatterers can be perceived as a shadow of precipitating clouds at higher altitudes. The Doppler measurements are direct measurements at the location of the scatterers. It is thus due to an indirect effect - the falling nature of raindrops - that the motion of radar reflectivity measurements is related to higher altitudes than where the radar is actually measuring.

From this example, the idea of a superior wind vector retrieval technique by fitting both the radar reflectivity and radar Doppler velocity measurements can be directed towards the trash bin. It can be expected to be troublesome, due to the aforementioned reasons.

We can also see from this example, that when there is a large difference between the wind vectors estimated from radar reflectivity and from radar Doppler velocity measurements, it can be an indication of vertical wind shear. It can, however, be extremely difficult - if not impossible - to estimate the number for vertical wind shear, as it is unclear at what altitude the precipitating clouds are. More research is required on this topic, to unravel for which cases the 4D-Var advection wind vector retrieval technique can be useful.

Quantitative analysis of retrieved wind vectors
The larger the distance from the radar location, the more challenging the retrieval of wind vectors for a single scanning Doppler radar becomes. The reason is that for an analysis volume (or grid box) that is further away from the radar, the variation in

measurement antenna looking directions (azimuth and/or elevation angles) are less diverse. This means that the line-of-sight (LOS) directions are less diverse, and it is harder to correctly estimate the velocity component in the direction perpendicular to the radar antenna LOS.

Common approaches for the validation of retrieved wind vectors are to compare them with wind vectors from weather prediction models or from in situ measurements, or make a comparison of projected radial velocities with radars that are looking from a different direction. Such comparisons typically do a good job when a lot of averaging is involved, to overcome difficulties with differences in time and spatial resolution, and the location of the instruments. In this work some alternative methods are proposed that look at the retrieved wind vectors from a different side. The aim is then to assess the quality of the retrieved wind vector fluctuations at the high resolution of the modern weather radar (a typical resolution is 100 m).

To achieve a validation of the retrieved wind vectors, statistical measures are defined that are useful to identify unrealistic wind vectors. In this work, measures for the curl and divergence of the wind vector field are defined and calculated. Secondly, residual of radial Doppler velocities are calculated as a function of time, both during the measurements that were used in the optimization, as well as for some time after that. This will give an indication of how good the retrieved wind vectors are during the time the measurements were done, but also for some time after that. The latter gives an idea of the predictive value of the retrieved wind vectors.

The circulation per unit area C [m s^{-1}] is calculated for an enclosed circle as (e.g. Marsden and Tromba 2003):

$$C = \frac{1}{2\pi r} \oint \vec{v} \cdot dl \quad = \frac{1}{2\pi r} \sum_i \int u_i r \sin\alpha d\alpha + \int v_i r \cos\alpha d\alpha$$

$$= \frac{1}{2\pi} \sum_i [u_i \cos\alpha - v_i \sin\alpha]_{\alpha=\alpha_{i1}}^{\alpha_{i2}}. \qquad (4.39)$$

This quantity is a measure of how much the wind field is rotating. With regards to a scanning radar that retrieves wind vectors in the horizontal plane, the integration takes place over the radar antenna azimuth looking angle α. For each azimuth interval $[\alpha_1, \alpha_2]$, averaged u_i and v_i are used in the integral. Further note that the circulation per unit area is equal to the curl, according to Stokes theorem (e.g. Marsden and Tromba 2003).

Another similar quantity D [m s^{-1}] is formulated, which calculates the component of velocity normal to the path integral, which is calculated for an enclosed circle as:

$$D = \frac{1}{2\pi r} \oint_C \vec{v} \times dl \quad = \frac{1}{2\pi r} \sum_i \int u_i r \cos\alpha d\alpha + \int v_i r \sin\alpha d\alpha$$

$$= \frac{1}{2\pi} \sum_i [-u_i \sin\alpha + v_i \cos\alpha]_{\alpha=\alpha_{i1}}^{\alpha_{i2}}. \qquad (4.40)$$

Via the divergence theorem in the plane - another form of Green's theorem - the quantity D is equal to the average divergence of the enclosed circle (e.g. Marsden and Tromba 2003).

Now that we have these two measures, we can apply them to the retrieved wind vectors, which is demonstrated in Fig. 4.5. As a check, the 4D-Var simple retrieval
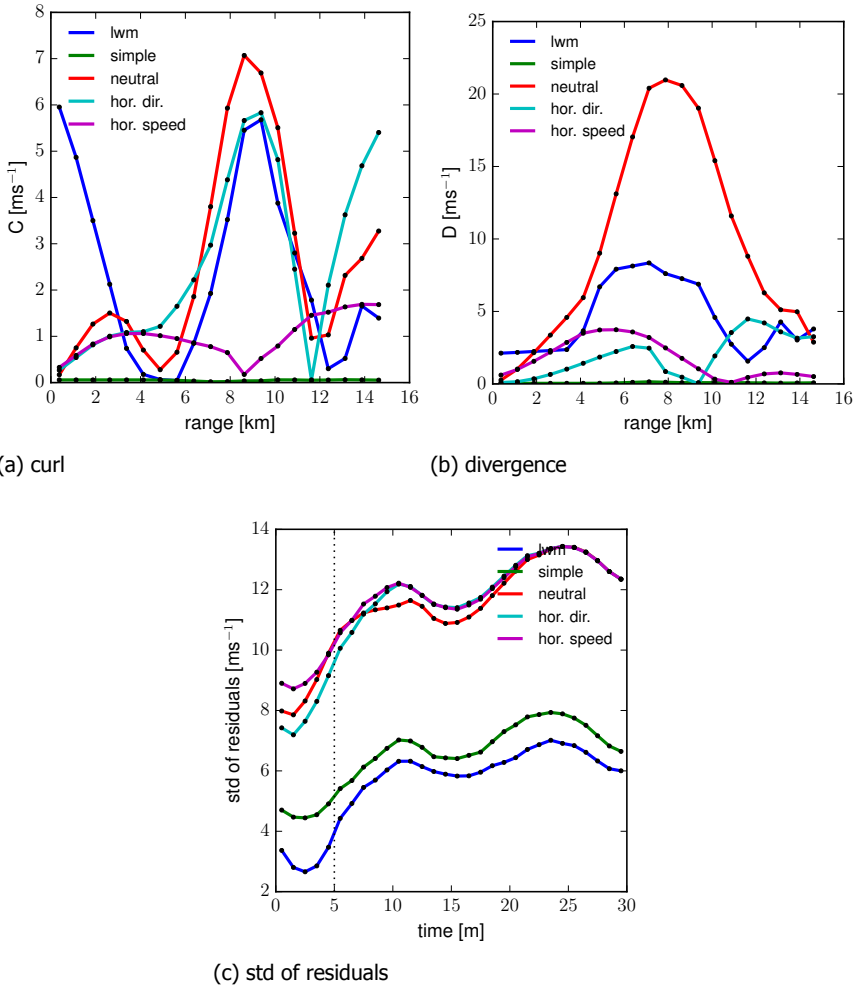

(a) curl

(b) divergence

(c) std of residuals

Figure 4.5: Quantitative analysis of the retrieved wind vectors for different implementations. In (a) a measure of curl, C, and (b) a measure of divergence, D, is calculated as a function of range. In (c) the standard deviation (std) of the residuals is calculated as a function of time. Until the dashed vertical line, the measurements are used in the optimization to fit the model parameters. After the dashed vertical line, the model is only used to predict the radar Doppler velocities. In the optimization, 5 minutes of IDRA Doppler measurements (approximately 5 horizontal scans) have been used.

technique, that retrieves just a single wind vector, gives zero values for the curl

and divergence, as expected. The other implementations for wind vector retrieval techniques, give some variations in the curl and divergence as a function of range. In particular deviating values in an ensemble of retrieved wind vector for the same radar measurements but for different retrieval techniques are interesting, as they can be used to assess the resulting wind vectors.

In Fig. 4.5, some unrealistic features of the retrieved wind vectors can be related to the implementation: (1) a high curl for the linear wind model at short distance from the radar, possibly due to separately retrieved wind vectors in several analysis volumes, and (2) a high curl for the 4D-Var direction at large distance, because the wind vector solution is forced in the direction perpendicular to the radar line of sight. Overall, only the 4D-Var simple and 4D-Var horizontal speed have zero or low values for the curl and divergence, and might thus be preferred over the others. Further investigation with in situ measurements at several distances from the radar are required to verify this. It is thus demonstrated here that by using measures for curl and divergence as a function of radar range, some unrealistically retrieved wind fields can be identified and marked as unreliable.

In physics, a very general principle with measurement results is that they should not depend on the parameters of the measurements. For example: if an elephant's mass measurement is 7341 kg in Paris, it should have the same mass measurement in Amsterdam. Regarding wind vector retrieval techniques, the wind vector measurement should not depend on the radar location. Alternatively stated: the retrieved wind vector for the same point in space and time should be the same if the radar would be moved to another location. With regards to our example we can state that: in the case of homogeneous terrain - which is the case for IDRA - we can expect a long-term average negligible range-dependence for radar-based retrieved wind vectors.

In Fig. 4.5c, the standard deviation (std) of residuals of radar Doppler velocities is plotted as a function of time. The residual is the modeled radar Doppler velocity minus the measured radar Doppler velocity. The lower the std of residuals, the better the model is able to represent the measurements. This figure shows that the linear wind model is the best with regard to reducing the difference between the model and the measurements. This is most likely due to the fact that the linear wind model has the most free parameters to fit to the solution (8 parameters for the linear wind model - u_0, u_x, etc. - for an analysis volume of 4 x 4 km, and just 2 parameters for the 4D-Var model - u, v grid point for each 4 x 4 km.). Somewhat surprising is that the advanced 4D-Var implementations give higher values than the 4D-Var simple implementation. It might be related to fitting a continuous wind field, the grid box size and/or the time allowed for the optimization routine for fitting the solution. More research is required to find out these details.

4.6. Conclusions

In this chapter, from simulations of the raindrop inertia effect, it is concluded that in most cases the influence of measuring from raindrops as tracers for the air motion can be neglected in radar-based wind vector retrieval techniques. Only for some special weather conditions, such as very strong shear in combination with large raindrops, a substantial deviation between air and raindrop velocity can be expected. In this work - which is not aimed at such special weather conditions - no additional effort is made to account for raindrop inertia in wind vector retrieval techniques.

A novel approach is proposed for the retrieval of the local wind vector field, with radar Doppler measurements. It is based on four-dimensional variational analysis (4D-Var) and the model of the wind field as an advected field. Several implementations of the 4D-Var wind vector retrieval technique, and a state-of-the-art reference technique, the linear wind model, are applied to radar measurements from IDRA. From a qualitative analysis, the linear wind model appears somewhat problematic, as there exist unrealistic jumps in the retrieved wind vectors near the edges of the analysis volumes, and the wind vector directions seem somewhat arbitrary at large distance from the radar. With the 4D-Var wind vector retrieval technique, this is solved, as all measurements are used simultaneously to estimate wind vector fields, and the solution is more continuous and appears to be more reliable. By choosing extreme settings in 4D-Var, the solution space of wind vectors can be demonstrated, which gives an impression of all the possible wind vector field solutions that are associated with the radar Doppler measurements.

Alternative approaches to in situ validation for the quantitative validation of radar-based retrieved wind vectors are proposed. They can be useful to check if the retrieved wind field fluctuations at the high resolution of modern radar are realistic. Measures for curl and divergence as a function of range have been used, to identify issues with the retrieved wind vectors and some unrealistic retrieved wind fields were identified. In addition, the standard deviation of residuals was calculated as a function of time, to compare how well the radar Doppler measurements are fitted and predicted. Further research is, however, required in combination with in situ measurements at multiple locations, to find out the most optimal retrieval settings for the 4D-Var wind vector retrieval technique.

The wind vector retrieval techniques that were applied here required typically a few minutes of processing time on a desktop computer to find an optimal solution. Therefore, they can be used in real-time applications. Depending on the application and the used computational resources, the performance can be enhanced by using less or more measurements, and/or a more finer/coarser grid at which the wind vectors are resolved.

5

Model-based estimation of turbulence intensity

In this chapter, the emphasis is on the application of raindrop-backscattering radar-based turbulence intensity retrieval techniques to relatively small scales. More specifically, we are looking here at the correct estimation of turbulence intensity from radar observations at the scale of the radar resolution volume of modern weather radars with a high spatial resolution of about 30 m or even less. At these small scales, the information of the raindrop size distribution (DSD) and turbulence intensity are mixed in the radar observables. Therefore, an accurate estimation of the rain DSD, and accounting for influence of raindrop inertia become crucial to estimate turbulence intensity. Different approaches are taken in this chapter on how to optimize the estimation of turbulence intensity from radar measurements during rain at these small scales, and it is investigated what the limits are of the state-of-the-art radar-based turbulence intensity retrieval techniques.

"Dreaming occurs in all ages, and there have always been people who could make dreams come true, as long as they obey the laws of science and laws of physics." - Gerard 't Hooft (translated from the book *Planetenbiljart*).

5.1. Introduction

In the state-of-the-art literature, turbulence is typically modeled in radar observables as an additional Doppler spectrum width term, or by smoothening and widening the spectrum via a convolution process (Borque et al. 2016; Bouniol et al. 2004; Doviak and Zrnić 1993; Kollias and Albrecht 2000; Shupe et al. 2012). There has been only little research to challenge these state-of-the-art approaches.

An alternative approach takes the influence of raindrop inertia into account, and can be found in the work by Yanovsky et al. (2003, 2015). In the work of Yanovksy, a raindrop is either a perfect tracer of the turbulent motion, or not involved in the turbulent motions at all for a given turbulent length scale and an equivolumetric raindrop size, A drawback of the model from Yanovsky is that it has heuristic parameters (L_{th} and V_w), which are difficult to estimate, and make it difficult - if not impossible - to develop this model further. Therefore, it is proposed to use a different and novel approach to account for the influence of raindrop inertia.

In chapter 2, inertial parameters were formulated based on the equations of motion for raindrops. With these parameters, a raindrop-inertia-correction model was formulated, which also includes tuning parameters that can be used to adapt the model to simulations of falling raindrops. This raindrop-inertia-correction model will be used in this chapter to estimate turbulence intensity from radar measurements.

The state-of-the-art models for turbulence in the calculation of radar observables are not perfect. Next to that the influence of inertia is often ignored, there are some features from turbulence unexplored in the modeling of radar observables. Here we note the two most important that are treated in this chapter:

1. the turbulence intensity has an effect on the ensemble of orientations of the scatterers and

2. there can exist a dependence between polarimetric radar observables and turbulence intensity.

These points are not considered in the literature with regard to radar-based turbulence intensity retrieval techniques to our knowledge. It is not hard to imagine, that the ensemble distribution of particle orientations will be different for calm and turbulent conditions. We can state some expectations as:

- For turbulent conditions, it can be expected that the particles are oriented in a more random fashion.

- For calm conditions, it can be expected that the particles are oriented in a more aligned and organized manner.

As a consequence of these two expectations, it can and it should thus be expected that the polarimetric radar observables depend on turbulence intensity.

A novel approach is proposed for how to apply non-stochastic turbulence in radar observables simulations. This novel approach is the so-called "ensemble of isotropic vectors" model, which has a solution for how to take the variation of an ensemble particle orientations into account for a given turbulence intensity. The

defining parameter for this turbulence model, is the turbulence broadening with the raindrop inertia effect included ($\zeta_I \sigma_T$), which depends on the turbulence intensity ϵ, the radar resolution volume parameters, and the raindrop size diameter.

To apply this novel model in radar-based turbulence retrieval techniques via optimal estimation, it is necessary to use a radar forward model to simulate radar observables. A radar forward model is a procedure that calculates radar observables, e.g. radar reflectivity Z, starting from physical model variables, such as the raindrop size distribution (DSD). Optimal estimation is the minimization of a cost function where simulated measurements are compared to real measurements to obtain the best fitting physical parameters, such as the turbulence intensity. A radar forward model in combination with optimal estimation is thus an advanced tool to accurately retrieve model parameters. A drawback is that modeling adds a lot of complexity, and a strategy has to be developed to constrain the solution space. For the estimation of rain and cloud parameters, such as the raindrop size distribution and turbulence intensity, there exist a few of such radar forward models (e.g. Donovan et al. 2008; Haynes et al. 2007; Ryzhkov et al. 2010; Voors et al. 2007). In this work, where the development and comparison of turbulence models in a radar forward model is crucial, it was found most practical to start from scratch, and a new program for optimal estimation with a radar forward model was created.

The structure of this chapter is as follows. First, the model-based calculation of radar observables is explained in detail with the so-called "radar forward model". Secondly, an overview is given of turbulence models that are used for the calculation of radar observables. A comparison is made between radar observables from stochastic turbulence models, and from a novel non-stochastic turbulence model (the "ensemble of isotropic vectors" model) with a few simulations. In addition, simulations are performed to get a qualitative picture of the influence of radar instrument parameters on the quality of radar-based estimated turbulence intensities. Consequently, a case study is made where Doppler radar data from TARA (Heijnen et al. 2000) is used to estimate turbulence intensity profiles during rain. In this case study, a correction is applied for the influence of raindrop inertia, which demonstrates the current potential and limitations of EDR estimation at the small resolution scale of a modern Doppler radar. In the end, the conclusions are drawn.

5.2. The radar forward model

A radar forward model is a procedure that calculates radar observables, e.g. the radar reflectivity factor Z [mm^6 m^{-3}], and takes physical model (field) variables as input, e.g. the raindrop size distribution (DSD), and next to that the radar instrument parameters, e.g. the radar beamwidth. Once the radar forward model is there, it can be used in optimal estimation where differences between the actual radar measurements and simulated measurements from the forward model can be minimized to estimate optimal physical model parameters. This concept of model-based optimal estimation via a radar forward model is demonstrated in Fig. 5.1. The essence is that differences are minimized, both for the physical parameters: a prior state vector is compared to a state vector; and for the measurements: actual radar measurements are compared with the model measurements from the radar

forward model. Note that Fig. 5.1 is for demonstration purposes only, as the complete lists of instrument features, physical fitting parameters, and radar observables are rather long.
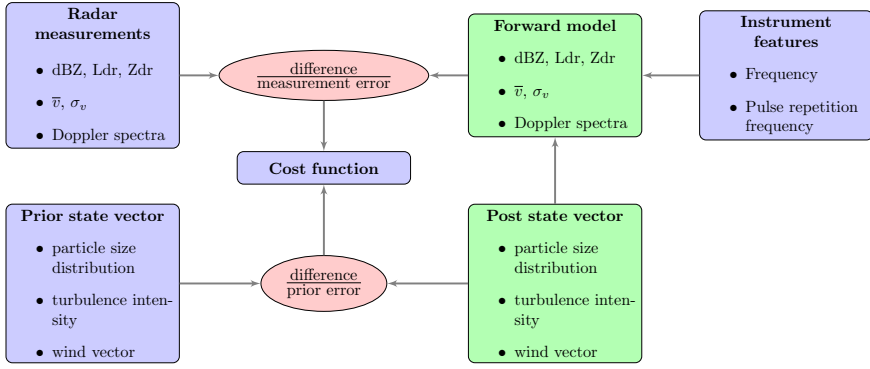

Figure 5.1: **Demonstration of the usage of a radar forward model in optimal estimation.**

Now we give the essential details with regards to the calculation of radar observables in a radar forward model.

The essential equation in the radar forward model is the weather radar equation, which states how much power is received by the radar antenna due to the backscattering of radar signals by meteorological targets such as raindrops. The weather radar equation can be written as (e.g. Doviak and Zrnić 1993):

$$< P_*(r_0) > = \frac{C_r}{r_0^2}\eta_*,\qquad(5.1)$$

where $< P_* >$ [W] is the expected received power, C_r is a radar constant, r_0 [m] is the range at the resolution volume center, and η_* [m² m⁻³] is the radar reflectivity, where the index $*$ is hh, hv, vh or vv to indicate the sending and receiving polarization state respectively.

The physical variables (turbulence, wind vectors, rain intensity) can vary within the scale of the radar resolution volume. Therefore, spatial integration of the physical variables becomes important, and the weather radar equation can be written in the following form to account for the power distribution for a specific radar resolution cell (adapted from Eq. 5.40 in Bringi and Chandrasekar 2001):

$$< P_*(r_0) > = C_r' \int_0^\pi \int_0^{2\pi} \int_0^\infty f(\theta_B,\phi_B,r,r_0)\eta_*(\theta_B,\phi_B,r)d\theta_B d\phi_B dr,\qquad(5.2)$$

where the integral is over radar range r, and radar BEAM coordinates θ_B and ϕ_B (see Appendix A). Further, C_r' is another radar constant, and f is a function that accounts for range weighting and a radar power pattern function.

When the assumption is made that the radar power is distributed with a Gaussian beam shape, and a range-dependence of r^{-2}, the function f can be written with

independent functions f_{θ_B} and f_r:

$$f(\theta_B, \phi_B, r) = f_{\theta_B}(\theta_B) f_r(r, r_0). \tag{5.3}$$

Note that Eq. 5.3 assumes a symmetrical pencil-like antenna power pattern, and therefore, this function has no dependence on the radar beam azimuth ϕ_B.

Consequently, the spatial area of the integral over the radar cell in Eq. 5.2 is divided into a finite number of smaller areas, the so-called subvolumes. By assuming a constant radar reflectivity for each subvolume $\eta_{*,i}$, the integral can be approximated as:

$$< P_*(r_0) >= C_r' \sum_i \left[\int \int \int f_{\theta_B}(\theta_B) f_r(r, r_0) d\theta_B d\phi_B dr \right] \eta_{*,i}, \tag{5.4}$$

where the summation is over subvolumes, and the integrals are over the space of each subvolume.

By choosing the subvolumes in such a way that the weight due to f is constant, the integral factor can be integrated into the radar constant. Eventually, this means that by choosing subvolumes with equal weight due to f, the weather radar equation that accounts for subvolumes can be written in a convenient way as:

$$< P_*(r_0) >= \frac{C_r}{r_0^2} \frac{1}{n} \sum_i \eta_{*,i}, \tag{5.5}$$

where n is the number of subvolumes. So in the end, Eq. 5.5 greatly simplifies the spatial integration of physical variables in the radar forward model to account for the radar antenna power pattern.

When a raindrop-size distribution is used in the radar forward model, the summation is expressed as a sum over a finite number of raindrop sizes in the following way:

$$< P_*(r_0) >= \frac{C_r}{r_0^2} \frac{1}{n} \sum_i \sum_j \eta_{*,i,j}, \tag{5.6}$$

where $\eta_{*,i,j}$ is the radar reflectivity for subvolume i and raindrop size j, and n is (still) the number of subvolumes.

The division of the radar resolution volume into subvolumes is convenient in the radar BEAM coordinates. To apply spatial integration of atmospheric physical variables, the BEAM coordinates have to be translated into the coordinates at which the atmospheric physical variables are stored. In this work, grids are used in ENU coordinates, and hence the BEAM coordinates are transformed to ENU coordinates. All the relevant coordinate transformations are given in appendix A.

An example of a hypothetical application can be as follows. A vertical profile of turbulence intensity is fitted with a vertically profiling radar. The physical parameter space is a vertical profile of EDR with a 100 m resolution in the ENU coordinates to match the radar resolution of 100 m range resolution in radar BEAM coordinates. Consequently, a turbulence intensity profile can be fitted to the radar measurements. From this simple example, it is thus clear that for each radar instrument

and application, the fitting parameters and ENU grid dimensions and resolutions have to be carefully chosen.

In the weather radar equation (Eq. 5.1), the radar reflectivity, η_* [m^2 m^{-3}], is defined as (Bringi and Chandrasekar 2001):

$$\eta_* = \int \sigma_*(D_e)N(D_e)dD_e, \qquad (5.7)$$

where σ_* [m^2] is the radar cross section (RCS) for a rain/cloud drop and $N(D_e)$ [m^{-3}] is the drop size distribution (DSD) with equivolumetric diameter D_e [mm]. Note that η_* is defined as a measure per unit volume.

radar reflectivity	$<\eta_*> = \sum_i \dfrac{\eta_{*,i}}{n}$
reflectivity factor	$<Z_*> = 10 \cdot \log_{10}(\dfrac{\lambda^4 <\eta_*>}{\pi^5 |K_w|^2})$
Doppler velocity	$<v_{*,D}> = \sum_i \dfrac{\eta_{*,i}}{n} v_{D,i}/<\eta_*>$
Doppler spectral width	$<\sigma^2_{v,*,D}> = \sum_i \dfrac{\eta_{*,i}}{n}\left(v_{D,i}-<v_{*,D}>\right)^2/<\eta_*>$
differential reflectivity	$<Z_{DR}> = 10 \cdot \log_{10}(<\eta_{hh}>/<\eta_{vv}>)$

Table 5.1: List of radar observables and their calculations. For the radar reflectivity $<\eta_*>$ the summation is over all particles and subvolumes (see Eqs. 5.5 and 5.6). Here K_W is the dielectric factor of water, and $v_{D,i}$ is the Doppler velocity of a particle. More details on radar observables can be found in textbooks, such as Bringi and Chandrasekar (2001) or Doviak and Zrnić (1993).

A list of commonly used radar observables is given in Tab. 5.1. These radar observables are relevant for different applications, such as rainfall estimation (e.g. based on $<Z_*>$), wind vector estimation ($<v_{*,D}>$), effective raindrop size estimation ($<Z_{DR}>$), and turbulence intensity estimation ($<\sigma^2_{v,*,D}>$).

Doppler spectral density bin	$<\eta_{*,1,2}> = \sum_{i,v_1<v_{D,i}<v_2} \dfrac{\eta_{*,i}}{n}/(v_2 - v_1)$
spectral differential reflectivity bin	$<Z_{DR,1,2}> = 10 \cdot \log_{10}(<\eta_{hh,1,2}>/<\eta_{vv,1,2}>)$

Table 5.2: Radar Doppler spectra calculations. The Doppler spectrum consists of velocity bins, for which the formulas are given here. For each velocity bin the radar observable is calculated, where subscripts 1 and 2 indicate the part of the velocity spectrum that is used in the calculation. Scaling with the velocity interval width then leads to the Doppler spectral density.

Next to the common radar observables, the radar Doppler spectra can be measured and modeled, with the difference that the common radar observables are separated into velocity bins. These definitions are given in Tab. 5.2. In this work, the Doppler spectrum is scaled by the inverse of the interval length $(v_2 - v_1)^{-1}$. Therefore, it is called the Doppler spectral density, which is convenient as it makes

Doppler spectra comparable, regardless of the number and widths of intervals. Also, the spectra can be used in retrieval techniques, such as a retrieval technique for the raindrop size distribution (e.g. Unal 2015).

For the cross sections σ_* in Eq. 5.7, calculations from Mishchenko (2000) or De Wolf et al. (1990) are used. Cross sections from Mishchenko (2000) have the advantage that they do not apply the Rayleigh assumption, and in the calculations the full polarimetric amplitude matrix for non-spherical particles is obtained. This means that there is the possibility to calculate the co-polar and cross-polar correlation coefficients. For most applications, usage of the full polarimetric amplitude matrix is unnecessary and the Rayleigh approximation can be used. In that case, the faster calculations from De Wolf et al. (1990) are preferred.

The radar forward model that is used here, and which was developed in this work, is implemented in the "Zephyros" software package (Zephyros is a Greek wind God). This software package can be used for the simulation of radar observables, and the development of radar-based retrieval techniques. This software package can be found on GitHub, and is written mostly in C, partly in FORTRAN, and has interfaces to *Python* and *Matlab*.

5

5.3. Turbulence models

In radar forward models, turbulence models are used to account for the influence of turbulent motion of particles on the radar observables. The most common approach to do this, is to enlarge the Doppler spectral width, and/or to convolute the Doppler velocity spectra to enlarge the spectrum width (Borque et al. 2016; Bouniol et al. 2004; Doviak and Zrnić 1993; Kollias and Albrecht 2000; Shupe et al. 2012). There has been done little research effort to challenge this common approach.

An alternative to this approach, is to use a stochastic turbulent wind vector field to simulate the radar observables. A stochastic approach can not be used in a retrieval technique, as it would lead to unstable results in a fitting algorithm. But such an approach can be helpful to develop more advanced parameterized turbulence models for the radar forward model. In contrast to a stochastic approach, the non-stochastic turbulence model always has the same outcome for the same turbulence intensity, but the result is artificial and not very realistic.

For a retrieval technique, a non-stochastic turbulence model has to be used, because otherwise the fitting algorithm becomes unstable. Therefore, the challenge is to develop a non-stochastic turbulence model that can be used to model radar observables (Z, Z_{DR}, etc.), which has the same dependencies on turbulence intensity as the stochastic turbulence model.

In this section, first a few stochastic turbulence models are used to simulate radar observables. Consequently, a novel implementation is developed that is capable of reproducing radar observable dependencies on turbulence intensity.
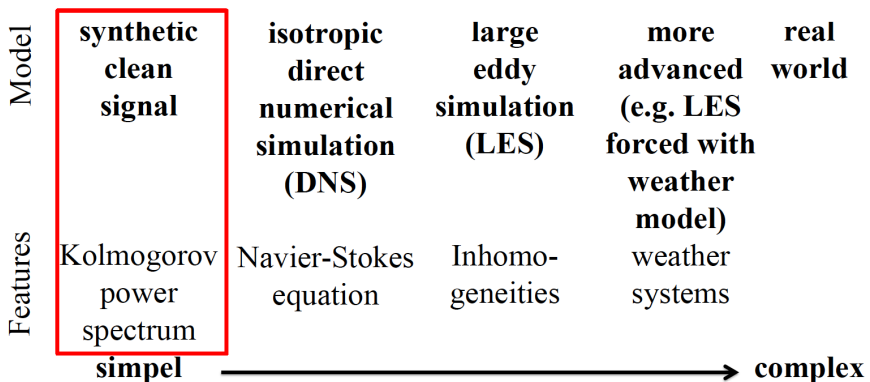
5.3.1. Stochastic turbulence models

Figure 5.2: Schematic overview of turbulence models with increasing complexity.

A schematic overview of stochastic turbulence models, with increasing complexity, is given in Fig. 5.2. In this work, the most basic turbulence models are used, the so-called homogeneous isotropic turbulence (HIT) models, which are based on the Kolmogorov -5/3 power law. The HIT models are convenient to use, because:

1. They are very fast in comparison to numerical models that solve the Navier-

Stokes equations, such as direct numerical simulation (DNS) or large eddy simulation (LES). Therefore, numerous realizations and experiments can be made.

2. They produce wind fields that satisfy the Kolmogorov power law at all locations in the field (homogeneous), and are similar for different directions (isotropic).

The last reason is important for simulation of radar-based EDR retrieval technique results, because a discrepancy between the input parameters for the simulation and the simulated retrieved parameters, such as EDR, can then be more easily explained. The simplicity of these models enhances the possibility to trace artifacts that appear in the resulting retrieved values of turbulence intensity. With more complex turbulence models (e.g. DNS/LES), the intermittency of turbulence intensity complicates this possibility to trace artifacts due to the radar measurement principles.

There are some differences in the available HIT models. The resulting turbulent wind vector produced by the different models are shown in Fig. 5.3. The considered HIT models and their abbreviations used here in further discussions include: Mann (1998) (MA98), Careta and Sagues (1993) (CA93), Pinsky and Khain (2006) (PI06), and Oude Nijhuis et al. (2014b) (CTM14). The most notable difference in the resulting turbulent wind vectors is the dimensionality, which is 3D for MA98, 2D for CA93/PI06, and 1D for CTM14.

One of the preferred models is MA98, because it simulates all three dimensions. By using MA98, any confusion with the simulation results due to the orientation of the radar with respect to the wind field is avoided. However, the simulation of three dimensions is consuming a lot of memory, and as a result the numerically resolved spatial scales are limited. In some specific cases with a specific research question, another model can then be preferred. For example, when the goal is to study phenomena in just one dimension with a wide range of spatial scales. In such a case, computational efficiency limits the usage of 3D HIT models with a broad domain of resolved spatial scales, and a 1D-HIT-model becomes useful.

The stochastic turbulence models produce wind fields, from which the appearance of turbulence in radar observables can be computed. In addition, the inertia effect can be accounted for using the methods proposed in Ch. 2. This is achieved by calculation of the inertial velocity term for an ensemble of particles, as a function of turbulence intensity with different values, and placed at different locations in the radar resolution volume. The additional velocity difference due to relaxation, $\vec{v}_p'$, is found by solving the equations of motion over its backward trajectory. The details for the calculation of a backward trajectory, and the estimation of the additional velocity due to relaxation can be found in chapter 2.

5.3.2. Non-stochastic turbulence models

Here two non-stochastic approaches are explained to simulate turbulence in radar observables. The first approach, which is the state-of-the-art (e.g. Doviak and Zrnić 1993), can be characterized as "smoothing/smearing" the radar spectrum with a turbulence term. The second approach, which is a novel approach developed in
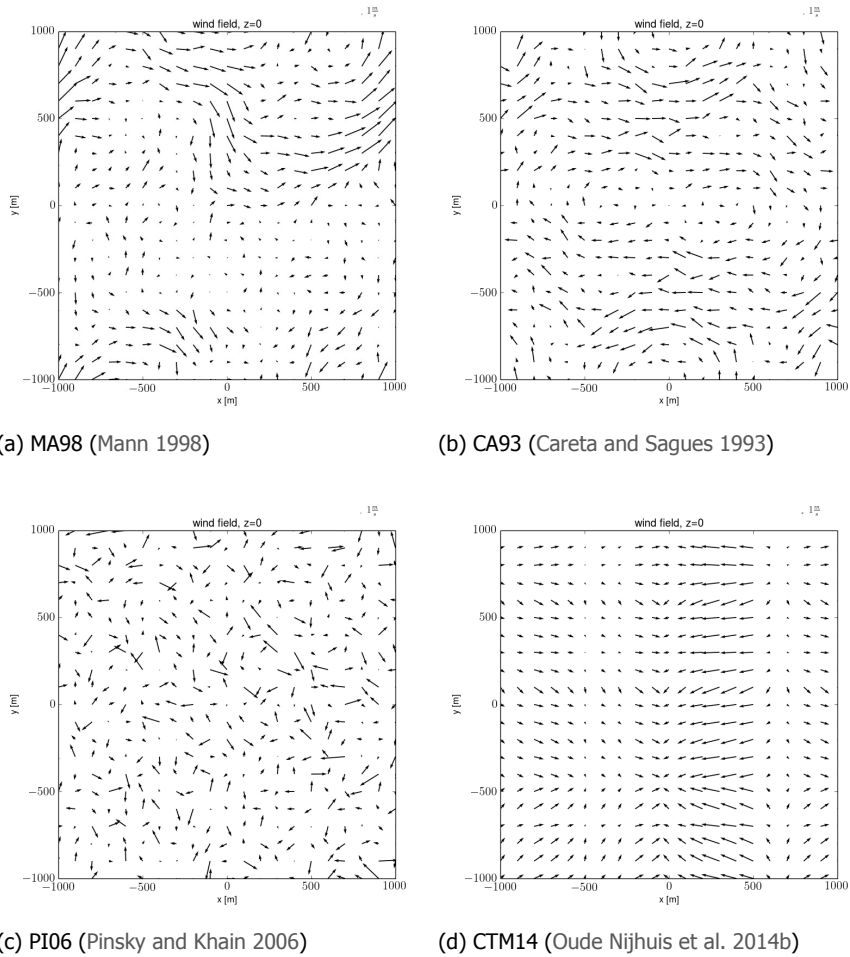
(a) MA98 (Mann 1998)

(b) CA93 (Careta and Sagues 1993)

(c) PI06 (Pinsky and Khain 2006)

(d) CTM14 (Oude Nijhuis et al. 2014b)

Figure 5.3: **Stochastic turbulence models**. Results are plotted for different implementations of HIT turbulence models. (a) MA98 from Mann (1998): A 3D wind field is made via a spectral tensor. Typically used in wind engineering. (b) CA93 from Careta and Sagues (1993): A divergence free 2D wind field is created via transformation from an auxiliary random scalar. Used in studies of diffusion processes. (c) PI06 from Pinsky and Khain (2006): A 2D windfield is obtained that obeys the continuity equation. Used for simulation of droplet tracks. (d) CTM14 from Oude Nijhuis et al. (2014b): A 1D windfield is produced with a large dynamic range (mm-km scale). Used for turbulence intensity retrieval technique studies. All these stochastic turbulence models have a periodic domain and do not simulate boundary layers.

this work, takes into account the orientation of particles.

Common approach

A common way how turbulence is modeled in radar observables is by adding a turbulence spectral width term to the radar Doppler spectral width, and with regard to

the Doppler spectra by a convolution, which results in smoothening and broadening of the radar Doppler spectra. For the Doppler spectral width, such a calculation can be formulated as, with regard to the formulated forward model in section 5.2:

$$< \sigma^2_{v,*,D} >= \sum_i \frac{\eta_{*,i}}{n} \left[\zeta^2_{I,i} \sigma^2_T + \left(v_{D,i} - < v_{*,D} > \right)^2 \right] / < \eta_* > , \qquad (5.8)$$

where $\zeta_{I,i}$ is the inertia correction for particle i, and σ_T is the turbulence spectral width without inertia correction. The addition of the inertia correction term, $\zeta_{I,i}$, is a novelty and generalization in this work, with respect to the state-of-the-art. In the case that $\zeta_i = 1$, there is no correction.

The radar Doppler turbulence spectral width for air motions without the influence of raindrop inertia σ_T can be calculated as:

$$\sigma^2_T = \frac{C \epsilon^{2/3}}{4\pi} I, \qquad (5.9)$$

where C is a Kolmogorov constant, ϵ the energy dissipation rate, and I is an integral for which we refer to White et al. (1999). The integral I takes the radar instrument characteristics into account.

The radar reflectivity for a velocity bin is calculated as:

$$< \eta_{*,1,2} >= \sum_{i,v_1 < v_{D,i} < v_2} \frac{\eta_{*,i}}{n} f(D_i, v_1, v_2)/(v_2 - v_1), \qquad (5.10)$$

where $f(D_i, v_1, v_2)$ is the fraction of Doppler velocities that are between v_1 and v_2 (see also Tab. 5.2). Note that the combination of velocity bins make up the spectrum. To include turbulence in the spectrum, the assumption is made that for each particle with a certain non-turbulent velocity, a turbulent velocity can be added that has the characteristic of a normal distribution with a zero mean and a standard deviation that is related to the turbulence intensity. The function $f(D_i, v_1, v_2)$ can then be calculated with the cumulative normal distribution function $F(x|\mu, \sigma)$ with mean $\mu = v_{D,i}$ and standard deviation $\sigma = \zeta_{I,i}\sigma_T$ as:

$$f(D_i, v_1, v_2) = F(v_2|v_{D,i}, \zeta_{I,i}\sigma_T) - F(v_1|v_{D,i}, \zeta_{I,i}\sigma_T). \qquad (5.11)$$

An advantage of this formulation is that the fall velocity and cross section are still in symbolic form. They are not convoluted by integrals, which would limit the choice of cross section and/or terminal fall velocity calculations. Therefore, any cross section implementation can be used here, such as the Mie cross sections from Mishchenko (2000).

Ensemble of isotropic vectors approach
In the "ensemble of isotropic vectors" approach, for each particle, an ensemble of velocity vectors is used. A vector $\vec{v}_{p,*}$ is calculated as:

$$\vec{v}_{p,*} = \vec{v}_t + \vec{v}_a + \vec{v}_{T,*}. \qquad (5.12)$$

This ensemble of 3D unit directions covers all possible directions. For each unit vector $\hat{k}_*$, a turbulence velocity vector $\vec{v}_{T,*}$ is calculated:

$$v_{T,*} = \zeta_I \sigma_T \sqrt{3} \hat{k}_*. \tag{5.13}$$

In this model, the Doppler spectral width is increased by $\zeta_I \sigma_T$, which is consistent with the state-of-the-art approach that adds a turbulence term to the Doppler spectral width. The difference with the state-of-the-art broadening calculations is that the particle orientation variation, caused by turbulence, is taken into account. The assumption made here is that the particle symmetry axis (/minor axis) is always parallel to the particle velocity vector ($v_{p,*}$). This methodology is demonstrated in Fig. 5.4. Additionally, this method implicitly models the raindrop canting angle

5
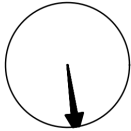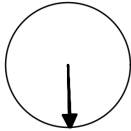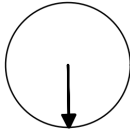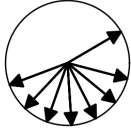
	0.1 mm	1.0 mm	5.0 mm
light turbulence, $\zeta_I \sigma_T = 0.1$ ms^{-1}.			
heavy turbulence, $\zeta_I \sigma_T = 2.0$ ms^{-1}.			

Figure 5.4: **Illustration of the ensemble of isotropic vectors approach**. In this 2D illustration (in reality 3D) an ensemble of particle orientations, representative for raindrops, is shown as a function of turbulence intensity and drop size. The relative sizes of the terminal fall velocity, air velocity and turbulence velocity determine the variation of orientations, and therefore, the polarimetric characteristics in the radar observables.

distribution. This is achieved because in the model each particle has an exactly defined orientation.

Although the ensemble of turbulence vectors ($\vec{v}_{T,*}$) covers all directions, the resulting ensemble of particle orientation vectors can either cover some segment of directions, or have a very specific direction, depending on the relative size of the terms for terminal fall velocity, wind velocity and turbulence velocity. This is illustrated in Fig. 5.4.

Now that we have a new model for non-stochastic turbulence, the next challenge is to examine whether it is reliable, by doing simulations. This is part of the next sections and future research. A further extension of the "ensemble of isotropic vectors" approach is the usage of different magnitudes of the turbulence vector $\vec{v}_{T,*}$, such that it can represent a distribution of kinetic energy.

5.4. **Simulations**

Given the radar forward model and a specific implementation of turbulence, we can get an idea how radar observables are influenced by turbulence. The main reason to do this is to learn from these simulations, and come up with recommendations on how to optimize turbulence intensity retrieval techniques. More specifically, we desire to have a tool to analyze the influence of turbulence intensity on radar observables, and see if the results depend on the specific HIT model that is used. Further, we would like to see whether it is possible to simulate the stochastic features of turbulence with a non-stochastic turbulence model that can be used in turbulence retrieval techniques. Essentially, we are thus looking for a non-stochastic model of turbulence in a radar forward model that is the best in simulating radar observations.

Here we use the novel non-stochastic turbulence model that was introduced in the section before, the ensemble of isotropic vectors approach, and try to validate this model by comparing features in the radar observables with a few stochastic turbulence models. Also, the implicitly produced canting angles are compared for the different turbulence models. In addition, a few simulations are performed to qualitatively optimize turbulence intensity retrieval technique parameters.

5.4.1. **Turbulence in scanning radar observables**

Simulation details

Here we explore how turbulence looks in the radar mean Doppler velocities and radar Doppler spectral widths for a scanning radar for different turbulence wind field simulations, both stochastic and non-stochastic.. The details of the simulations are as follows: The radar frequency used is S-Band (3.298 GHz), a liquid water content is used of 1 g m^{-3}, and a raindrop size distribution with gamma distribution parameters of $\mu = 5$ and $D_0 = 2$ mm. The radar resolution parameters are of a hypothetical radar, with a full width halve maximum (FWHM) radar beamwidth of 2.1 °, and a range resolution of 30 m. In the simulations, a radar antenna elevation angle of 0° has been used to avoid the additional terms due to raindrop terminal fall velocities.

It is convenient to start with relatively simple simulations, which will become more complex in the following parts. Regarding mean Doppler velocity and Doppler spectral width, a non-zero elevation looking angle of the radar antenna would lead to contributions from raindrop terminal fall velocities, which make the results harder to interpret. The simulated mean Doppler velocity and Doppler spectral width for a elevation looking angle of 0 ° are not so sensitive to the radar frequency or raindrop size distribution parameters. Therefore, these simulations are representative for many scanning radars, having other frequencies or other raindrop size distributions.

In the simulations, no noise is added to the simulations, as it could be confused with the influence of turbulence. The influence of raindrop inertia is not taken into account in the simulations here yet. The turbulence wind fields have been used that were described in the previous section (see Fig. 5.3).

Results

In Fig. 5.5 the turbulence signal is shown in the Doppler velocities, and in Fig. 5.6 the Doppler spectral widths, for different turbulence implementations. They demonstrate how turbulence looks like in radar observables.

There are some differences in radar observables for the different HIT models, which can be attributed to their implementations. For example, CTM14 simulates a 3D turbulent wind velocity in one dimension, which results in an artificial similarity for the non-simulated direction. Although CA93 and PI06 are 2D simulations, it is impossible to see this in the simulated scanning radar observables. The non-stochastic turbulence model (PA15) is clearly different in the resulting radar observables from the others. This non-stochastic turbulence model gives a zero Doppler mean velocity, and a smooth field in the Doppler spectral width. The non-stochastic turbulence model has thus no features of turbulence intermittency (random irregularities). So, by interpreting the resulting figures quantitatively, it is concluded that the implementation of Mann (1998) is preferred for stochastic turbulence simulations, as it simulates a wind field in all three dimensions, which is the most realistic.
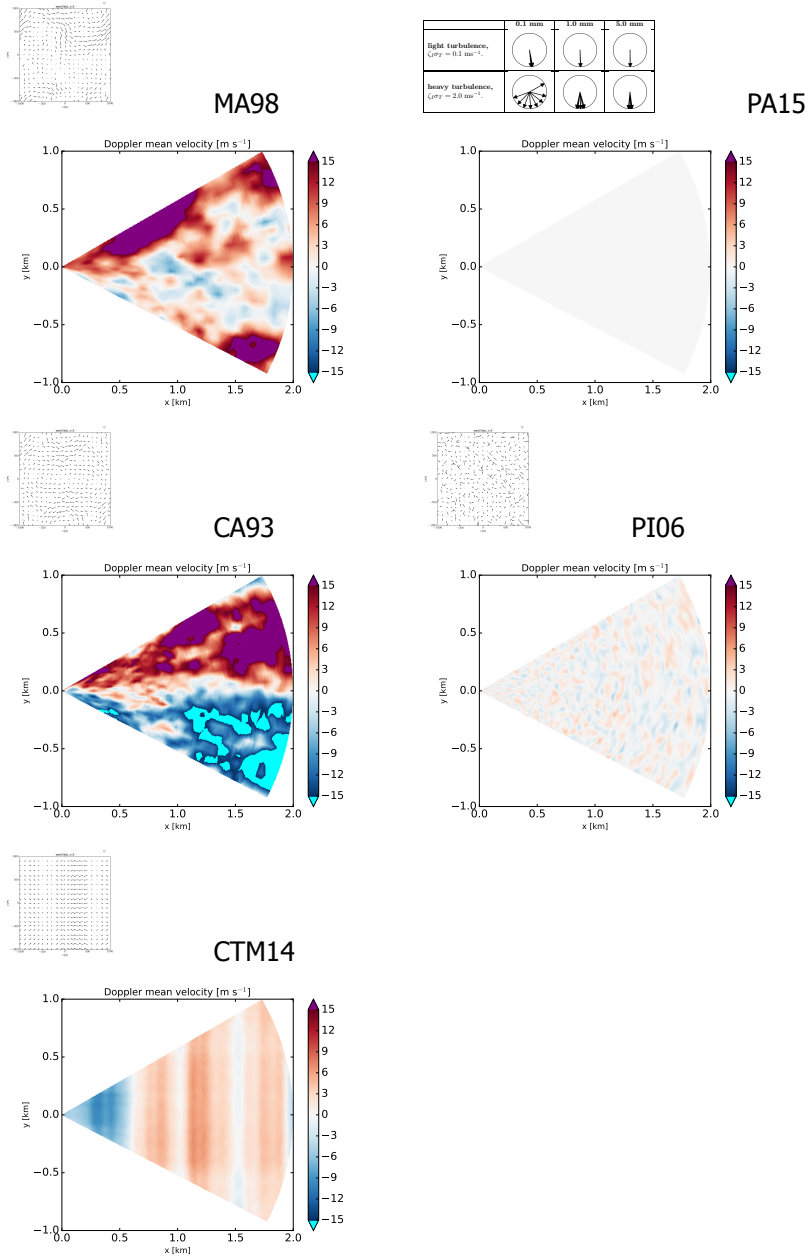
5

Figure 5.5: **Horizontal scanning radar simulations.** Doppler velocities are plotted for a radar that scans in the xy-plane (radar antenna elevation looking angle is 0 °), for different turbulence implementations in the radar forward model. The turbulence intensity (EDR) is 0.1 m² s⁻³. The abbreviations refer to the turbulence model that is used (see Fig. 5.3, PA15 refers to the "ensemble of isotropic vectors" model).
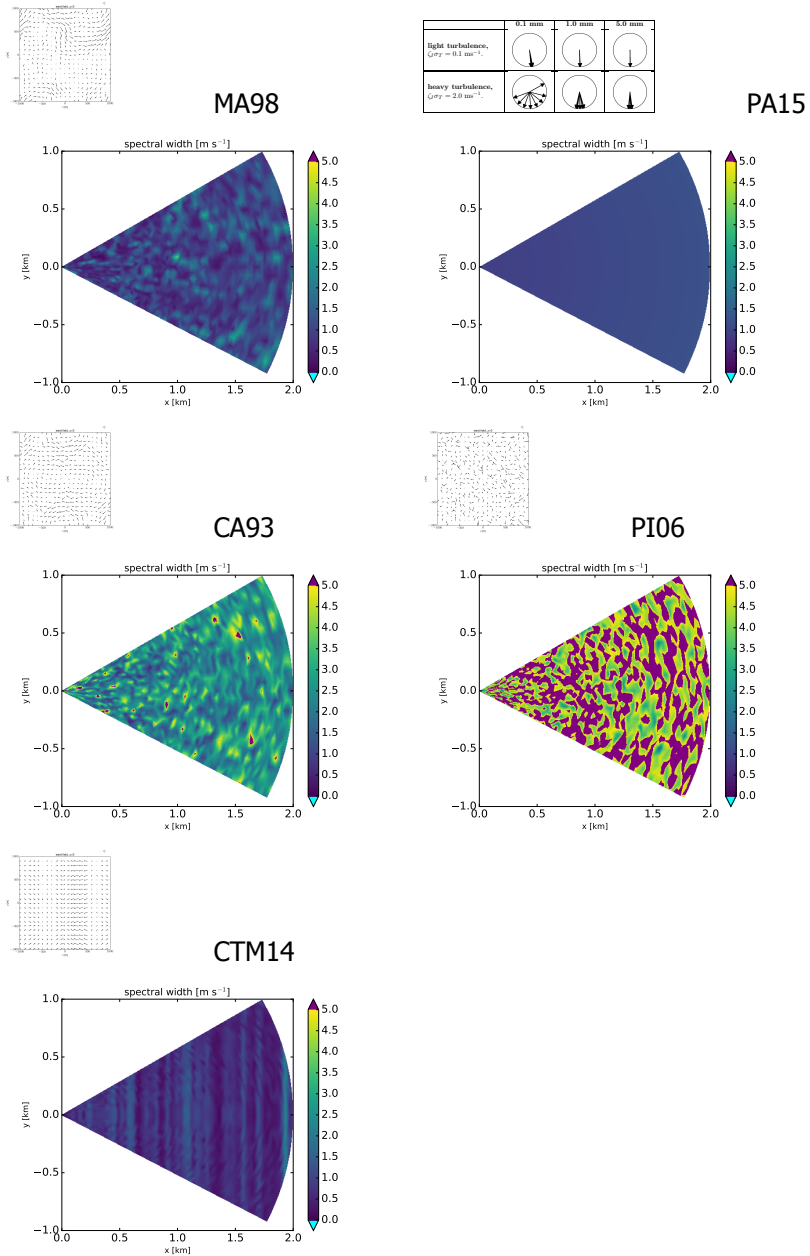
Figure 5.6: **Horizontal scanning radar simulations.** The Doppler spectral widths are plotted for a radar that scans in the xy-plane (radar antenna elevation looking angle is 0 °), for different turbulence implementations in the radar forward model. The turbulence intensity (EDR) is 0.1 m² s⁻³. The abbreviations refer to the turbulence model that is used (see Fig. 5.3, PA15 refers to the "ensemble of isotropic vectors" model).

5.4.2. **Turbulence in polarimetric radar observables**
Simulation details
For the simulation of turbulence in polarimetric radar observables, an antenna radar elevation looking angle of 45 ° is used. This is necessary for the radar to be sensitive to the particle orientations. For the radar instrument details, the features of TARA are used (Heijnen et al. 2000), which are: an S-band radar frequency (3.298 GHz), a full width halve maximum (FWHM) radar beamwidth of 2.1 °, and a range resolution of 30 m. Further, a liquid water content is used of 1 g m^{-3}, and raindrop size distribution with gamma distribution parameters of $\mu = 5$ and $D_0 = 2$ mm.

In these simulations, the emphasis is on the dependencies of radar observables to the turbulence intensity, which can be useful in model-based parameter estimation of EDR. In the simulations the symmetry axis (/minor axis) of the raindrops is oriented parallel to the direction of their velocity, which is the sum of the terminal fall velocity and the simulated turbulent wind velocity.

Sensitivity of polarimetric radar observables to turbulence intensity

5

Results
In Fig. 5.7 the simulated polarimetric radar observables are shown for different turbulence intensities. As expected, the Doppler spectral width increases with larger EDR. However, for the stochastic turbulence model there is some variation in the results, which is most likely due to turbulence intermittency.

For the polarimetric radar observable Z_{dr}, only a very weak dependence on turbulence intensity is found, which is only present for strong turbulence (EDR values larger than 10^{-2} m^2 s^{-3}). The dependence of Z_{dr} on the median raindrop size is much stronger (Brandes et al. 2004), in comparison to the dependence of Z_{dr} on turbulence intensity shown here. It can thus be expected that it is difficult to estimate turbulence intensity from Z_{dr}. With regard to quantitative precipitation estimation (QPE) based on Z_{dr}, it can be expected that a bias can be expected in the case of strong turbulence.

For L_{dr} a nice linear relation is demonstrated with the simulations, and could thus be very useful as an estimator for turbulence. However, a problem is that the demonstrated values are below the level of what a radar can typically measure (approximately -30 dB), and would thus require a very sensitive radar (read: very costly).

From these simulations, we can derive that the polarimetric radar observables Z_{dr} and L_{dr} are not useful for radar-based turbulence estimation. With regards to improvement of radar-based estimation of raindrop size distributions or QPE (e.g. Kowalewski and Peters 2010; Zhang et al. 2001), there is potential to take the uncertainty that turbulence creates in polarimetric radar observables into account. For example by exploiting that the radar observable Z_{dr} is likely to be more accurate at locations with low turbulence intensity.

With these simulations, it is shown that the ensemble of isotropic vectors approach produces qualitatively the same dependencies of radar observables for tur-
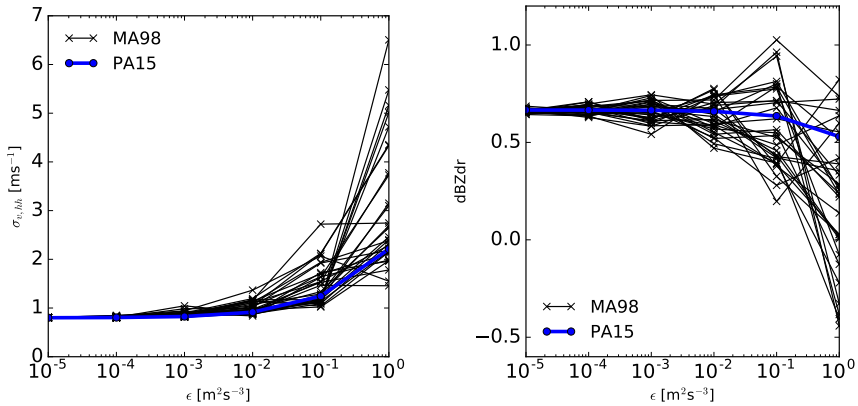
(a) Doppler spectral width

(b) dBZdr
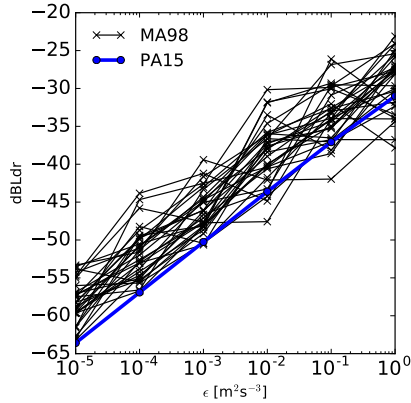
(c) dBLdr

Figure 5.7: **Sensitivity of polarimetric radar observables to turbulence intensity** for a non-stochastic, ensemble of isotropic vectors approach (blue line), and a stochastic approach (Mann 1998) (black lines) in the radar forward model. The radar measure with an elevation looking angle of 45 °, and the turbulence intensity (EDR) is varied in these simulations. Shown are: (a) the Doppler spectral width [m s^{-1}], (b) Z_{dr} [dB], and (c) L_{dr} [dB] as a function of the energy dissipation rate (EDR). In these simulations, $\mu = 5$, $D_0 = 2$ mm, and the inertia correction is not applied ($\zeta = 1$).

bulence intensity as stochastic turbulence implementations. However, more research is required to demonstrate that this can be useful in radar-based turbulence intensity estimation, because there are uncertainties due to the turbulence nature. Further, the sensitivity of Z_{dr} to turbulence intensity is too weak in comparison to the sensitivity of Z_{dr} with raindrop size distribution parameters. For L_{dr} the sensitivity to turbulence intensity is too weak to measure.

Canting angles
The polarization scattering properties of active radar signals in a medium with scattering particles are determined by the particle shapes and their orientations (e.g. Beard et al. 2010; Beard and Jameson 1983). With regard to precipitation, this is quantified by the canting angle, which is the orientation of a particle with respect to a reference orientation. Raindrops are normally expected to fall with their flat bottom towards the surface (as a pancake), and in this case the raindrop symmetry axis and the vertical direction are aligned. In the case of shear or turbulence, the canting angle can be changed, and can thus also alter the polarization properties of the backscattered radar signals. Here we give an impression of how turbulence intensity influences the canting angles of raindrops for the described turbulence models. It is in particular interesting to see how canting angles are modeled in the novel turbulence model, the ensemble of isotropic vectors approach.

In this work the canting angle is defined as the angle between the symmetry (/minor) axis of a raindrop and the vertical direction $\hat{e}_z$:

$$\beta = \cos^{-1} \frac{\vec{v}_p \cdot \hat{e}_z}{|\vec{v}_p||\hat{e}_z|},\tag{5.14}$$

where $\vec{v}_p$ is the particle velocity (see Eq. 5.12), which is assumed to be aligned with the spheroid vertical symmetry axis. For an ensemble of particles, the canting angle spread is calculated as the standard deviation of β:

$$\sigma_\beta = \text{STD}(\beta).\tag{5.15}$$

Note that σ_β is independent with respect to the reference orientation.

Here we are mostly interested in the canting angle spread, because this variable is influenced by the turbulence intensity. The value of σ_β is determined by the relative size of turbulence velocities, which have random orientations, in comparison to the terminal fall velocity, which has a fixed orientation and depends on the equivolumetric drop size. It can be expected that for calm conditions, the raindrop orientations have little variation and have a low value σ_β. For more turbulent conditions, it is expected that σ_β is higher due to more spread in the particle orientations. To make fair comparisons, it has to be asserted that the canting angle spread is independent of other particle variables or radar instrument parameters, such as the particle shape, the particle size, or the radar antenna orientation.

Results
In Fig. 5.8 the canting angle spread is shown for the novel non-stochastic turbulence model (the ensemble of isotropic vectors approach) and for the stochastic turbulence model from Mann (1998). For reference, the canting angle spread is also shown for 2-D video disdrometer (2DVD) measurements. In all the figures, the canting angle spread σ_β is plotted as a function of equivolumetric drop size diameter, which asserts that this parameter is independent of the particle size. For the raindrops, it is assumed that the shape is always a spheroid, determined by the equivolumetric drop size, where in this work the relation is used from Beard
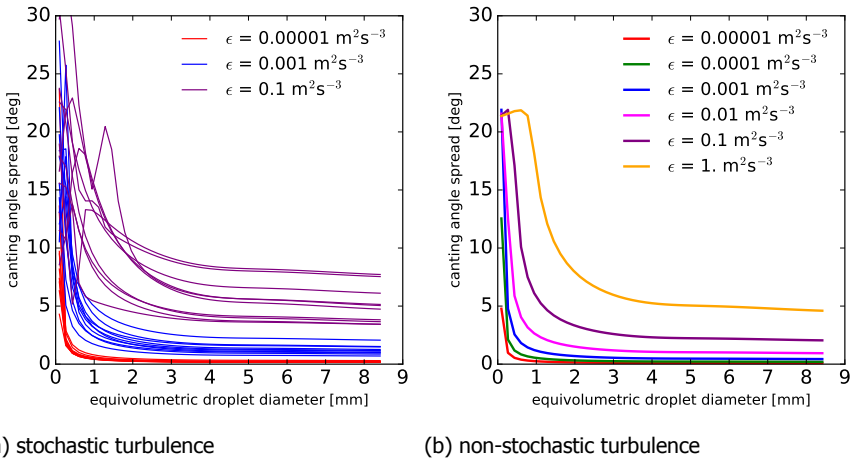
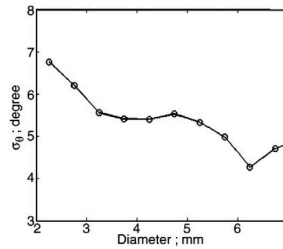(a) stochastic turbulence

(b) non-stochastic turbulence

Fig. 24. Standard deviation (σ_θ) of θ versus drop size (D_{eq}) from the 80-m fall bridge experiment. The size intervals are from 2 to 7 mm with 0.5 mm step. The last data point represents those drops greater than 7 mm. Note that in calm conditions prevalent during the experiment, the large drops are more stably oriented (smaller σ_θ) than small drops (larger σ_θ). The 95% confidence interval of σ_θ is estimated to be <0.3° for the range of diameters considered.

(c) in-situ data

Figure 5.8: **Canting angle spread** for (a) a stochastic turbulence model from Mann (1998), (b) a novel non-stochastic turbulence model (ensemble of isotropic vectors approach), and (c) from in situ data. The bottom figure is adapted from Beard et al. (2010). In these figures inertia is not included ($\zeta = 1$).

and Chuang (1987). In the simulations, as well as the measurements, the canting angle spread decreases for large equivolumetric drop sizes. This is as expected, as the terminal fall velocity will be larger, which can be interpreted as a more vertically preferential particle orientation. For the stochastic turbulence model, a few realizations are shown for the same turbulence intensity, which demonstrate the variability in the results due to the stochastic nature of turbulence. For the non-stochastic turbulence model, quite similar results are found, which demonstrates that the model is consistent with the stochastic model.

Also, the measurements from the literature are consistent with the turbulence models, although the turbulence intensity was not measured. From in situ obser-

vations of canting angle spread (Fig. 5.8c) and using a qualitative comparison with the other figures (Fig. 5.8a and (b)), we can estimate that the turbulence intensity was around $\epsilon = 0.1$ m^2 s^{-3} for the 2DVD measurements (inertia effect not considered). This result is promising, because it demonstrate that the novel model for turbulence can be useful in further applications.

What do these new results imply? In most of the state-of-the-art implementations of turbulence in radar observables that use the broadening/smoothing approach, there is no dependency between the orientations of particles and turbulence intensity (e.g. Doviak and Zrnić 1993). By the development of models for polarimetric radar observables, that include a dependency on turbulence intensity, retrieval techniques of turbulence intensity but also other parameters such as rainfall rate might become more accurate. The simulations have shown that it possible to include turbulence intensity in a novel manner with the ensemble of isotropic vectors approach. In particular, a comparison of the canting angle spread of models with measurements can be useful in further research for the validation and the development of radar forward models. It could be interesting to perform the 2DVD measurements again, but with inclusion of in situ turbulence intensity measurements. It would also be interesting to make comparisons with older work from (e.g. Beard and Jameson 1983), which claims to have found consistency of theoretical and measurements of rather small canting angle spreads of about $2\,^\circ$ due to turbulence.

5.4.3. Optimization of retrieval technique parameters

Here we use relatively simple experiments to formulate recommendations for turbulence intensity retrieval techniques. An essential problem with turbulence intensity retrieval techniques is that there is no reference to true EDR. Therefore, it makes sense to simulate EDR retrieval techniques, and study the influence of radar instrument parameters and retrieval technique settings on the retrieved EDR values. The goal is to give a qualitative picture of optimal parameters for retrieval techniques, by applying EDR retrieval techniques to simulated turbulent wind vector fields, and estimate the bias in retrieved EDR values for radar and sonic anemometers,

The bias and precision of retrieved EDR values from the simulated measurements are studied to synthesize recommendations for EDR retrieval techniques. In this small theoretical study, a turbulence wind field is created by using the cascade turbulence model (Oude Nijhuis et al. 2014b). In the cascade turbulence model, 3D turbulent wind vectors are simulated along one dimension, given a prescribed turbulence intensity (EDR), and $l_{max,sim}$, the maximum length scale of the inertial range. The advantage of this relatively simple turbulence model is that a wide range of spatial scales can be resolved (details in Oude Nijhuis et al. (2014b) and section 5.3.1). A disadvantage is that the simulation experiments are limited to just one dimension. The simulated wind field fluctuations are in the horizontal direction. This allows to use the vertical wind velocity variance (VWVV) technique (see section 3.2) for retrieving EDR, or more advanced techniques that use the second-order structure function, or the power spectrum.

Four experiments are conducted that will give an idea of the influence of mea-

suring with a certain configuration using either a sonic anemometer or a radar instrument. The first two experiments consider EDR retrieval techniques, without considering the instrument measurement principles. They are thus representative for potential issues of sonic anemometers and Doppler radars. In the first experiment the influence of the number of samples used in the retrieval technique is simulated. In the second experiment, the influence of not measuring in the inertial range is simulated. Then, some specific features of the radar instruments are studied. In the third experiment, the influence of spatial averaging due to the radar beamwidth and a cloud structure is studied. And in the fourth experiment, the influence of noise is simulated. In these experiments, the influence of measuring from raindrops is not considered (raindrop terminal fall velocity, raindrop inertia), and can be found in other sections of this work.

Experiment 1: influence of the number of samples
 In this experiment the number of samples is varied for different EDR retrieval tech-
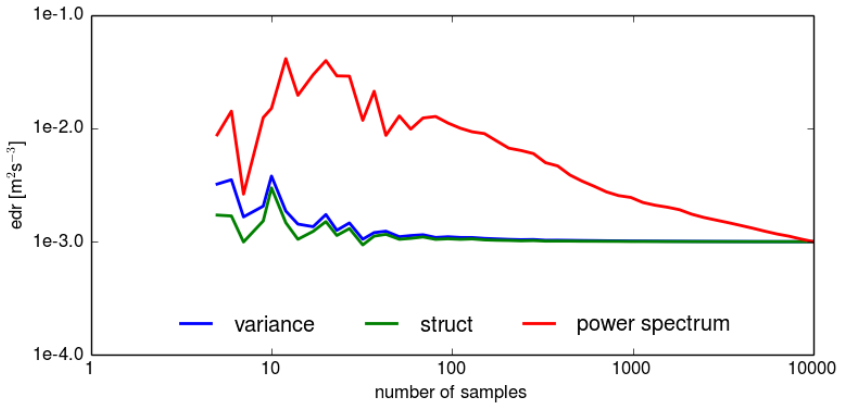

Figure 5.9: **Experiment 1: influence of the number of samples** N**.** A series of vertical velocities from a sonic anemometer is simulated with the cascade turbulence model (Oude Nijhuis et al. 2014b). The EDR values are retrieved from the vertical velocity variance. The number of samples, N, is varied, which can lead to a bias in measured EDR in case of too few samples.

niques. In Fig. 5.9 the result of the first experiment is shown. The total sampling time for the vertical velocities is 10 minutes, and the number of samples is varied, while keeping the time intervals the same. The true EDR value is 10^{-3} m^2 s^{-3}, and is obtained when sufficient samples are taken for all retrieval techniques. When the number of samples is too low, e.g. $N = 5$, a bias is obtained in the retrieved EDR value. When the number of samples is sufficient, $N > 50$, there are no biases in the variance technique (VVWV) and the structure function technique (SSF). This is different for the power spectrum EDR retrieval technique, which has a positive bias, and needs much more samples to achieve consistency with the other retrieval techniques.

Experiment 2: measuring outside the inertial range
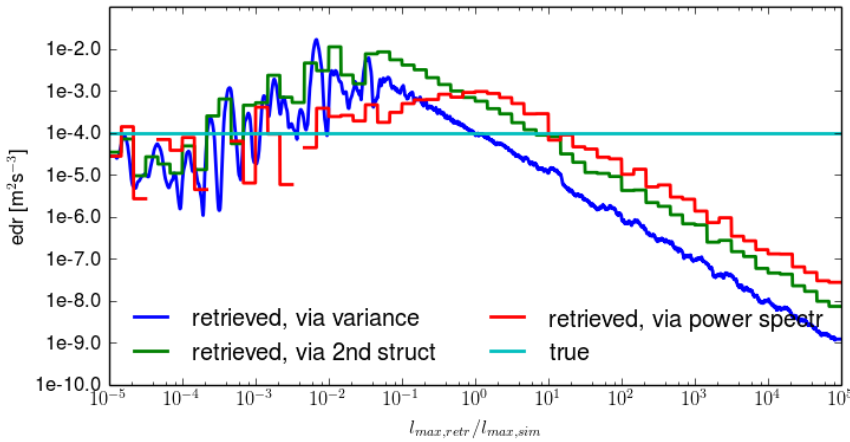 A problem with EDR retrieval techniques is that it is usually unknown whether

Figure 5.10: **Experiment 2: measuring outside the inertial range.** A series of vertical velocities from a sonic anemometer is simulated with the cascade turbulence model (Oude Nijhuis et al. 2014b). The EDR values are retrieved from the vertical velocity variance. In this experiment vertical velocity measurements are simulated outside and inside the inertial range.

the measurements are performed in the inertial range of the turbulence energy spectrum, i.e. whether the Kolmogorov -5/3 power law applies to the measured velocities. Therefore, in this experiment such a mismatch is created artificially.

In Fig. 5.10 the result of this experiment is shown, where there is a mismatch of the maximum length scale of the inertial range between the simulation and retrieval. In this experiment there are 100 samples, the total sampling time interval is 10 minutes, and the horizontal wind speed is 10 m s^{-1}. There is no noise added to the measurements, or spatial averaging applied to the simulated measured velocities. The inertial range is modified, by varying the maximum spatial scale in the inertial range l_{max} (see Fig. 3.2, $l_{max} = \lambda_{max}$). In this experiment, there is a mismatch between the maximum spatial scale of the inertial range in the retrieval $l_{max,retr}$, and the maximum spatial scale of the inertial range in the simulation $l_{max,sim}$. If $l_{max,retr} > l_{max,sim}$, the measurements are performed outside the inertial range. And if $l_{max,sim} < l_{max,retr}$, the measurements are inside the inertial range. The fraction $l_{max,retr}/l_{max,sim}$ is plotted on the x-axis, so on the left side the measurements are inside the inertial range, and on the right side the measurements are outside the inertial range.

A somewhat surprising result is that the different EDR retrieval techniques are almost always consistent (except for a small bias), even when the measurements are performed outside the inertial range. Therefore, consistency of retrieved EDR values, retrieved with different retrieval techniques does not prove that the measurements are in the inertial range. What we can learn from these simulations, is that another method is required to validate if the velocity measurements are in the

inertial range of the turbulence energy spectrum. For example by calculation of the power spectrum of wind speeds (see e.g. 3.8).

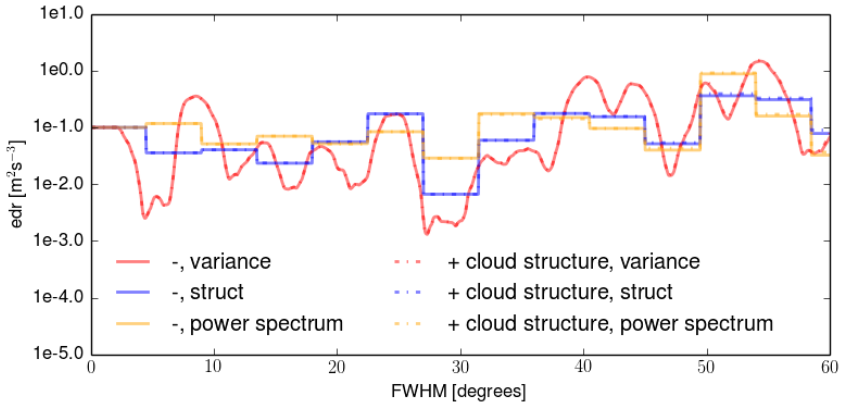**Experiment 3: influence of spatial averaging**

Figure 5.11: **Experiment 3: influence of spatial averaging.** A series of vertical velocities measured with a radar is simulated with the cascade turbulence model (Oude Nijhuis et al. 2014b). The EDR values are retrieved from the vertical velocity variance. A cloud structure (Hogan and Kew 2005) is added in the simulations, and the radar beamwidth is varied in the simulations.

In the third experiment, the influence of spatial averaging is considered. This can be relevant when the radar cells are only partially filled, due to inhomogeneous rain fields. In Fig. 5.11, the result of the third experiment is shown, which demonstrates the dependence of retrieved EDR values on spatial averaging and data gaps. The number of samples used was 100, the total sampling time was 10 minutes, and the horizontal wind speed was 10 m s^{-1}. Note that the spatial scale and the time scale are linked via the Taylor hypothesis of frozen turbulence (see e.g. (Taylor 1938), or discussion in Chapter 3). In the simulations no noise is added and the radar beamwidth full width halve maximum (FWHM) is varied, which is then plotted on the x-axis. The reference true value for EDR is 0.1 m^2 s^{-3}. In this experiment a modeled stratocumulus cloud from Hogan and Kew (2005) is used (or not) in the simulations, which gives some variation in reflectivity and some data gaps. It is found that EDR values for all retrieval techniques are rather well retrieved, and the cloud structure or the weighting of the radar power pattern does not raise any concerns with these retrieval techniques. This result might depend on the fact that no noise was added, and that the total sampling scale was much larger than the radar resolution volume.

Further research is required to validate these findings. It would be interesting to see how the radar beamwidth influences EDR retrieval techniques that are applied on the small resolution volume scale. Next to that, a few alternative cloud simulations are necessary to validate the influence of data gaps due to different

cloud types. Also, note that the used cloud model from Hogan and Kew (2005) is not very representative for the radar, as it simulated stratocumulus clouds, for which many radars are not sensitive. On the other hand, it can be expected that rain from stratocumulus clouds has a similar spatial structure, but this has to be further investigated.

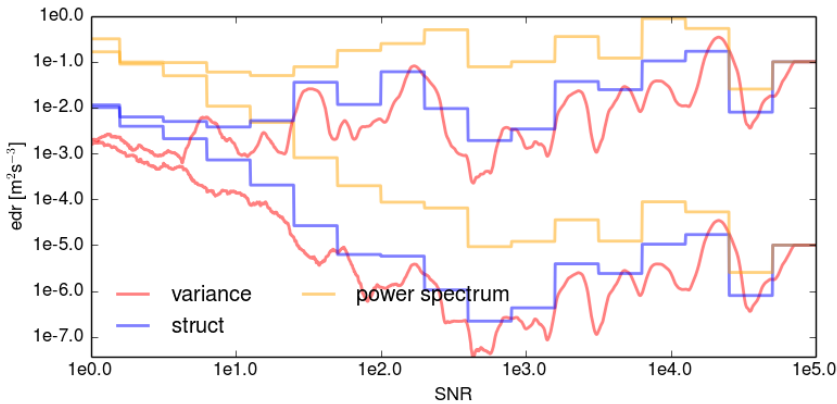**Experiment 4: influence of noise**

Figure 5.12: **Experiment 4: influence of noise.** A series of vertical velocities measured with a radar is simulated with the cascade turbulence model (Oude Nijhuis et al. 2014b). The EDR values are retrieved from the vertical velocity variance. In these experiments noise is added to the measurements and the signal-to-noise-ratio (SNR) is varied. In the right side there is mostly a turbulence signal (almost no noise), and in the left side there is mostly a noise signal (almost no turbulence signal).

In the last experiment, the influence of noise in the radar measurements is considered with regard to measuring EDR. In Fig. 5.12 the result of the fourth experiment is shown. In this experiment, noise with different levels of intensity is added to the radar measurements. The number of measured Doppler velocity samples used is 100, and the total sampling time interval is 10 minutes. The results have been performed for two EDR truth values of 10^{-1} and 10^{-5} m^2 s^{-3}. In the figure, the signal-to-noise ratio (SNR) is varied on the x-axis. This means that on the left side the measurements consist mostly of noise, and on the right side the measurements consist mostly of the turbulence signal. The result is as expected: the EDR is well retrieved for sufficient SNR (> 1e2 = 20 dB), or it is compromised in the limit of low SNR (< 1e1 = 10 dB). There is an exception for the power spectrum retrieval technique, where a much higher SNR is required of 1e3 = 30 dB.

Discussion of the experiments
We have seen that due to turbulence intermittency random discrepancies can exist in retrieved EDR values of up to 100%. For common EDR retrieval techniques (VWVV, SSF) 50 samples should be sufficient. When there is consistency of retrieved

EDR values from different retrieval techniques, it has not been proven that the measurements are in the inertial range of the turbulence energy spectrum. This means that for an accurate estimation of EDR, always some means are necessary to estimate the wind speed power spectrum. From the available methods, the power spectrum is most challenging, because for consistency a high SNR is required and a high number of samples.

In general, a qualitative picture has been given for the sensitivity of some essential parameters in turbulence intensity retrieval techniques, which can be used to enhance them. Further research is required to test the retrieval techniques for other cloud types, and also for other total sampling times.

5.5. Application to the TARA radar

Here turbulence intensity profiles are estimated from radar Doppler measurements during rain at relatively small spatial scales from the TARA radar (Heijnen et al. 2000), including a correction for the raindrop inertia effect. In a case study, TARA measurements were used during the ACCEPT campaign, with a radar antenna elevation looking angle of 45 °. The research question that is addressed here is:

- Can we accurately measure EDR from this FMCW precipitation profiling Doppler radar during rain at the radar resolution volume scale?

To answer this question, the following steps are taken:

1. estimation of the raindrop size distribution (DSD),

2. application of the raindrop-inertia-correction model,

3. estimation of turbulence intensity (EDR), and

4. validation of the results with EDR values from in situ sonic anemometer measurements.

The instruments that have been used are shown in Fig. 5.13, which consist of the TARA radar, the sonic anemometer for in situ EDR validation (see Chapter 3 for details), and the Parsivel sensor (Tokay et al. 2014) that can measure the drop size distribution locally.

A major challenge is how to obtain an accurate estimation of the DSD, which can be based on the radar measurements, or can be based on the in situ ground-level measurements. Note that the DSD estimation is not the major challenge addressed in this work, and simply state-of-the-art works have been used for this. In Tab. 5.3, two commonly used radar-based DSD techniques are given, that use either only the reflectivity (Marshall and Palmer 1948), or both reflectivity and differential reflectivity (Brandes et al. 2004). Typically, these radar-based rain DSD retrieval methods are applied via analytical relations, e.g. a Z-R relation. In this work the methods of (Marshall and Palmer 1948) and (Brandes et al. 2004) have been applied via an routine were the fit parameters are obtained via a fit of the modeled reflectivity (and differential reflectivity) to the measured radar observables (see Fig. 5.1 for details).
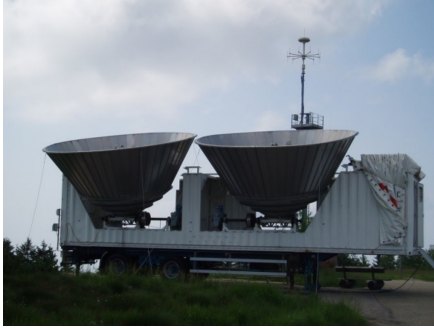
(a) TARA radar   (b) Parsivel sensor

(c) Sonic anemometer

Figure 5.13: **Instruments used for this case study:** (a) the TARA FMCW precipitation profiling S-band Doppler radar (Heijnen et al. 2000; Unal et al. 2012), (b) a Parsivel sensor, located at ground level during the ACCEPT measurement campaign, providing in situ DSD measurements (Tokay et al. 2014), and (c) Gill R3-100 sonic anemometers, attached to levers from the meteorological 200 m research tower in Cabauw at several altitudes (Ulden and Wieringa 1996).

	fitted	model
A. Marshall-Palmer	L	$D_0 = 1.639 L^{0.25}$, $\mu = 0$
B. Constraint-gamma	L, D_0	$\mu = 6.084 D_0^2 - 29.85 D_0 + 34.64$

Table 5.3: **Two radar-based retrieval techniques of gamma drop size distribution (DSD) parameters**. In A. the rain water content L [mg m^{-3}] is fitted from the radar reflectivity, with the model from Marshall and Palmer (1948). In B. also the gamma distribution parameter D_0 is fitted from the differential reflectivity, via the model adopted from Brandes et al. (2004).

Please note that the resulting rain DSDs are not any different than the ones that would be obtained with the analytical relations. However, in optimal estimation techniques, it is common to fit and use physical parameters, which are independent from the radar measurements, and it is convenient that the radar forward model takes into account the instrument features. As an example to illustrate why optimal estimation is better to use: in the literature there exist relations to estimate the rain DSD from Z_{dr} for a *horizontally* scanning radar, but such a relation will be erroneous when the radar antenna elevation looking angle is changed. When a radar forward

model is correctly used, such an error would not be easily made.

In addition, two alternatives for the DSD estimation are used which are: in situ ground-level measurements from a Parsivel sensor; and a novel radar-based DSD retrieval technique that uses the Doppler spectrum (Unal 2015).
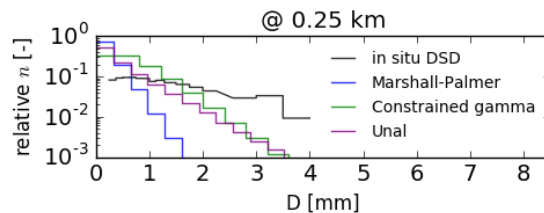
Retrieved rain DSDs
In Fig. 5.14, the retrieved rain DSDs are shown. For the DSD model from Mar-
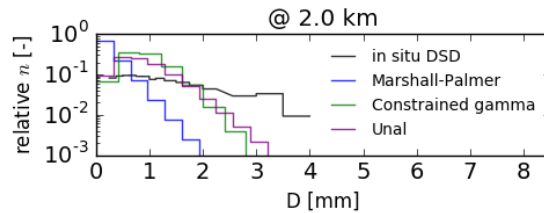
(a)
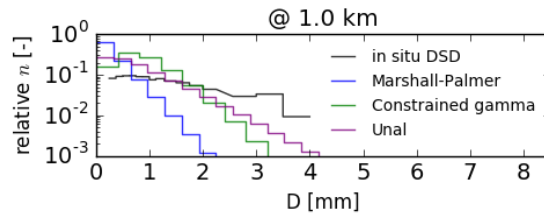
(b)

(c)

Figure 5.14: **Estimated drop size distributions.** On the y-axis the relative drop size number densities are plotted against drop size intervals on the x-axis for three different altitudes.

shall and Palmer (1948), the largest number concentration is given to the smallest droplets. For the other two radar-based DSD estimations, a slightly larger number concentration is given to larger drops. However, none of the retrieved DSD reflect the in situ DSD estimation, which has a rather flat distribution.

It can thus be concluded that for this case study (and thus for this specific time), based on a comparison of estimated DSDs, the radar-based retrieved DSDs are not

consistent and biased towards smaller droplets.

We further stress here that the measured in-situ DSDs were obtained with 30 seconds of temporal integration. It is part of further research, to extend this comparison to more case studies, and to redo this comparison with more spatial and temporal averaging to overcome issues with measurement representativeness, and thus gain more confidence in such comparisons.
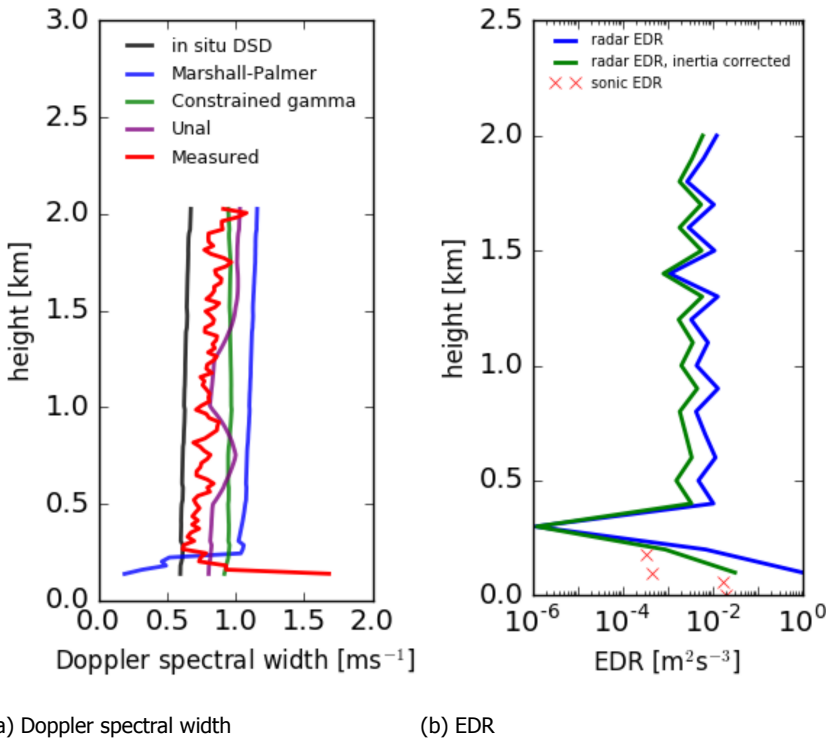

(a) Doppler spectral width   (b) EDR

Figure 5.15: **Retrieved profiles**. (a) Doppler spectral width profiles, due to raindrop terminal fall velocities, calculated with the estimated raindrop size distributions (DSDs), without turbulence. (b) With in situ ground-level DSD, the EDR is estimated, including a correction for raindrop inertia. In addition, EDR values estimated from sonic anemometers have been plotted (red crosses, STWSV retrieval technique, details in Chapter 3).

In the next step, given the rain DSD, the Doppler spectral width due to raindrop terminal fall velocities is calculated. This is shown in Fig. 5.15a.

Note the problem here: If the modeled terminal fall velocity Doppler spectral width is already larger than the measured Doppler spectral width, there is no turbulence spectral width to estimate (turbulence intensity can not be negative!). Therefore, the turbulence intensity can not be estimated for this case study. Therefore, it can be concluded that the state-of-the-art radar-based DSD retrievals - that were

applied in this case study - are not accurate enough to correctly estimate turbulence intensity. A solution to this problem requires a more accurate estimation of the rain DSD, which is outside of the scope of this work.

Retrieved EDR from the Doppler spectral width
Since there are problems with sufficient accurate radar-based estimation of the radar Doppler spectral width for this case study, a simple workaround solution is used to estimate EDR from the Doppler spectral width, just for illustration purposes. The solution is to use the ground-level in situ DSD for the estimation of the turbulence spectral width. It can be expected that this approach may be problematic in further applications, because the in situ ground-level estimated DSD may not be representative for the higher altitudes, and often such measurements are not available. The resulting estimated EDR, both with and without raindrop inertia correction, is shown in Fig. 5.15. The application of the raindrop inertia correction, based on Chapter 2, is thus finally demonstrated.

Obviously, more research effort is needed to further improve the accuracy of EDR estimation at the scale of the radar resolution volume, and in particular with regard to the modeled radar Doppler spectral width due to raindrop terminal fall velocities.

5.6. **Conclusions**

In this chapter, a novel model for turbulence in radar forward models is proposed: the ensemble of isotropic vectors approach. This model takes the orientations of particles into account as a function of turbulence intensity. The novel non-stochastic turbulence model implicitly produces a relation between turbulence intensity and particle orientations, the particle canting angles. A novel feature of this approach is that the polarimetric radar observables, Z_{DR} and L_{DR}, then also depend on turbulence intensity, although a direct usage of such a connection is limited due to various reasons. This novel model is promising for future applications of more accurate radar-based retrievals of turbulence intensity and drop size distributions. Additional observations of simultaneous raindrop particle orientations and turbulence intensity are, however, necessary to further validate and develop this model.

A qualitative picture was given with simulated theoretical experiments for optimal parameters of turbulence intensity retrieval techniques, such as the number of samples that should be used. The results of these experiments can be used to apply EDR retrieval techniques in the most optimal way.

In a case study, it was found that the radar-based retrieved DSDs are not yet accurate enough for the estimation of the radar Doppler spectral width component of raindrop terminal fall velocities. The estimated terminal fall velocity Doppler spectral width was larger than the measured radar Doppler spectral width. Therefore, the turbulence intensity was too small to measure or, only with in situ rain DSD estimates, the turbulence intensity profile could be estimated. EDR profiles were retrieved from the profiling radar, given the in situ DSD, for which it was possible to demonstrate the raindrop inertia correction.

Further research is recommended for the improvement of radar-based rain DSDs, and accurate estimation of the radar Doppler spectral width. In particular[1], it has been recognized that the following topics are interesting to consider in more depth. (*) The relation between the raindrop terminal fall speed and turbulence intensity (e.g. Bringi et al. 2018; Stout et al. 1995). This should be considered, as measurements suggest that there is a "slowing down" of the terminal fall speed for a raindrop with the same equivolumetric drop size for larger turbulence intensities. This has not been considered in this work (or many other works). (*) Consideration of application and testing of this study with more sensitive radars and studies with regard to raindrop canting angles (e.g. Bringi et al. 2008, 2011). (*) The consideration of other scattering calculations for asymmetrical raindrops (e.g. Manić et al. 2018).

---

[1]after a global review of this chapter and an extensive discussion with Merhala Thurai and Viswanathan Bringi

6

Application at an airport

In this chapter, retrieval techniques for wind vectors and turbulence intensities are applied to a fast scanning X-band radar and a scanning Doppler lidar, to demonstrate their application at an airport. This can be seen as an extension of the work from the previous chapters to a practical application. The radar measurement used in this chapter, were taken during the Ultra-Fast Observations (UFO) project trials at the Toulouse-Blagnac airport. In the UFO project, sensors have been developed that satisfy all the requirements for current standard operations for monitoring wind hazards at airports as well as for future advanced dynamic separation concepts. This chapter will show some of the UFO project results, which consider the application of EDR and wind vector retrieval techniques to a fast scanning X-band radar and a scanning Doppler lidar at an airport.

"Transformation to an eco-effective vision doesn't happen all at once, and it requires plenty of trial and error - and time, effort, money, and creativity expended in many directions." - Cradle to Cradle: Remaking the Way We Make Things.

6.1. Introduction

The UltraFast wind sensOrs (UFO) project, `http://www.ufo-wind-sensors.eu/`, explored the future of sensors for monitoring wind hazards at airports. In situ, profiling and scanning sensors were developed and used for the retrieval of wind vectors and turbulence intensity, during trials at Toulouse-Blagnac airport, see Fig. 6.1. The results of the UFO project are published in a *Bulletin of the American Meteorological Society* (BAMS) scientific journal article Oude Nijhuis et al. (2018b), and in this chapter the relevant results with regard to wind and turbulence intensity retrieval techniques are given.

Figure 6.1: Impression of the UFO trials at Toulouse-Blagnac airport. In the middle there is the 1.5 μm scanning lidar from Leosphere, and on the right there is the solid-state X-band radar from Thales.

6

A scanning 1.5 micron coherent Doppler lidar, and a solid state X-Band Doppler radar have been developed in the UFO project, with improved update rates, spatial resolution and coverage. In addition, Mode-S data downlinks have been collected for data analysis. The lidar and radar are complementary, to be able to measure during both clear air and rainy conditions.

For the implementation of advanced dynamic separation concepts in modern aviation, accurate and frequent wind and turbulent intensity observations are needed in specific areas, such as the aircraft approach and takeoff paths. Current standards for monitoring wind hazards at airports - low level windshear alert system (LLWAS) and in situ sonic anemometer wind measurements - are limited for this purpose, as they represent surface measurements, which are lacking representativity for the whole airspace (e.g. Wieringa 1980). To achieve accurate wind information at higher altitudes, measurements along the aircraft's approach and takeoff paths are required. Another purpose of the added measurements is to improve weather forecasts, which require more observations for assimilation to do so (Illingworth et al. 2015).

In this chapter, a demonstration is given of what can be obtained with the combination of a modern scanning Doppler lidar and a modern scanning Doppler radar at an airport. The contents are on a lower level of detail with regard to the previous dissertation chapters, and the details of the retrieval techniques themselves can also be found there. First, the retrieved wind vectors are shown and discussed. Then the retrieved turbulence fields are presented. And finally, the conclusions are drawn.

6.2. **Wind vectors**

With a lidar or radar the line-of-sight (LOS) velocity v_r is measured, using the Doppler-induced frequency shift on the backscattered signal, and is expressed by (e.g. Doviak and Zrnić 1993, or chapter 4):

$$v_r = u \cos \gamma' \sin \alpha + v \cos \gamma' \cos \alpha + w \sin \gamma', \tag{6.1}$$

where γ' is the radar looking elevation angle, α is the azimuth looking angle, and (u, v, w) are the wind-components in a Cartesian ENU coordinate system (see appendix A). Consequently, wind vectors can be reconstructed by model-based parameter estimation.

For the radar, Eq. 6.1 applies, but more challenges in the wind vector retrieval technique arise, because, for example, rain/cloud drop motions differ from air motions. A classical approach to retrieve 3D wind vectors from a scanning radar is to use the linear wind model, in combination with a least squares fit (e.g. Doviak and Zrnić 1993, or chapter 4). A more advanced proposed method is to use a radar forward model, in combination with an optimal estimation procedure (chapter 4). When the measured Doppler velocities are assimilated for a longer period of time, and the forward model accounts for variations in time, we can refer to this as a four-dimensional variational analysis (4D-Var) technique. With the 4D-Var technique a cost function χ is minimized, to obtain a wind field on a grid (chapter 4):

$$\chi_{v,r}^2 = \sum_i \left(\frac{\mathbf{P_{r,i}K} - v_{r,i}}{\sigma_{v,r,i}} \right)^2 + (\mathbf{K_{v,r}} - \mathbf{K_{v,r,p}})^T \mathbf{S_{v,r,p}}^{-1} (\mathbf{K_{v,r}} - \mathbf{K_{v,r,p}}),$$

$$\tag{6.2}$$

where the first term is concerned with the measurements, and the second term is concerned with the parameters. The first term compares modeled with measured Doppler velocities, where $\mathbf{K}$ is a vector containing the model parameters that are fitted, $\mathbf{P_{r,i}}$ is an operator to estimate the measured radar Doppler velocity for measurement i, which is calculated as $\hat{v}_{r,i} = \mathbf{P_{r,i}K}$, $v_{r,i}$ is the measured Doppler velocity, and $\sigma_{v,r,i}$ is the uncertainty of the measured Doppler velocity. The second term compares prior parameters with the parameters that are being fitted, where $\mathbf{K_{v,r}}$ contains the parameters that are being fitted, $\mathbf{K_{v,r,p}}$ contains the prior parameters, and $\mathbf{S_{v,r,p}}$ is the error covariance matrix of the parameters. More details on the wind vector retrieval techniques can be found in chapter 4.

In Tab. 6.1 some advanced processing features of the 4D-Var wind vector retrieval technique are listed. The 4D-Var retrieval technique has a clear advantage, as it can show the solution space of wind vectors that is associated with the radar measurements, which is not possible with the linear wind model approach. Further, it has an advantage regarding the use of a priori information. The 4D-Var wind retrieval technique is a rather general technique, and can be applied to remote radar or lidar Doppler measurements, for different scenarios and settings. From a comparison of different techniques, it is found that a 4D-Var wind vector retrieval technique, based on an optimal estimation procedure, is most optimal for

6

Linear wind model	4D-Var
- Measurements processed for each analysis volume - Discontinuities at edges of each analysis volumes - Spurious results at large distance - Unclear how small-scale wind variations are resolved. - Time variation not included	- Measurements processed for a single or multiple scans at once - Coherent and smooth full solution - Use of a priori information at large distance - Possibility to show solution space by choosing extreme parameters - Geostrophic advection of fluctuations can be included

Table 6.1: A list of some advanced processing features with regard to using 4D-Var to retrieve wind vectors with a radar during the rain in comparison to a commonly used wind retrieval technique, the linear wind model.

the single scanning Doppler radar for the retrieval of wind vectors, in particular at large range (Chapter 4).

In Fig. 6.2 the result of wind vector scans is shown, where both the scanning lidar and the scanning radar are working simultaneously to get a display of wind speed and wind direction in the vicinity of the airport. The scanning lidar measurements are fitted here with the linear wind model with the parameters $(u_0, u_x, u_z, v_0, v_y, v_z, u_y + v_x, w_0)$ with analysis volumes of 4 x 4 km. The scanning radar measurements are fitted here with the 4D-Var wind vector retrieval technique, with a grid resolution of 4 x 4 km. Note that in Fig. 6.2 the altitudes of the measurements are shown with circles in the background. In Fig. 6.2a retrieved wind vectors are shown for lidar in the atmospheric boundary layer (ABL). Close to the surface, where the lidar instrument was measuring, the wind field is rather homogeneous and no strong winds were measured. As there was light rain during these measurements, the lidar was not able to measure beyond 5 km due to attenuation. The observation of wind vectors and turbulence beyond 5 km were obtained from the scanning X-band radar, which is shown in Fig. 6.2b. At the higher altitudes (> 500 m), stronger wind was measured with values of up to 8-9 m s^{-1}. These wind maps help to improve the awareness of hazardous wind at the airport.

6.3. Turbulence intensities

The most basic EDR retrieval uses the variance of radar/lidar Doppler velocities as input (Bouniol et al. 2004; Brewster and Zrnić 1986; O'Connor et al. 2010; Yanovsky et al. 2005). More advanced EDR retrieval techniques, rely on processing of the power spectrum of velocities, or structure functions of velocities (Frehlich et al. 1998; Pope 2000; Siebert et al. 2006). By using the hypothesis of Taylor of "frozen" turbulence (Taylor 1938), the EDR retrievals can also be applied in the time

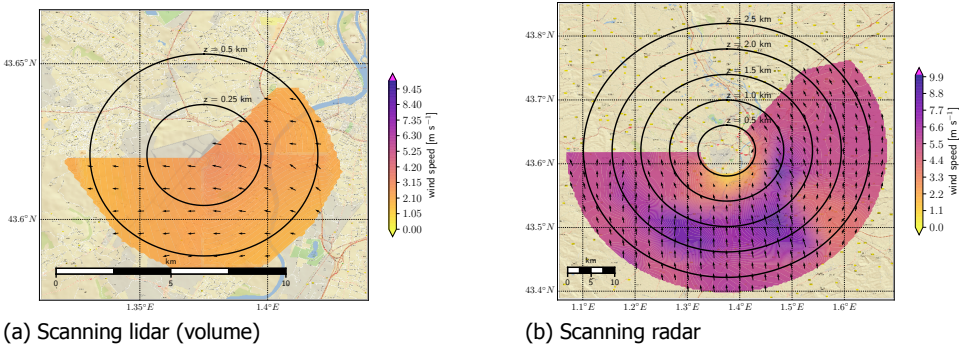(a) Scanning lidar (volume)   (b) Scanning radar

Figure 6.2: Retrieved wind vectors during the Toulouse trials on 1412 UTC 24 April 2014 from (a) the scanning Doppler lidar, and from (b) the scanning Doppler radar. In the background the wind speed is plotted in color contours, and the wind direction is shown with arrows on top. The altitudes of the measurements are shown with circles in the background.

domain. A practical advantage of using EDR, is that just one parameter is sufficient to connect atmospheric energy transfer to wake vortex lifetime and wind hazards. It should be noted that it becomes challenging when there are differences in retrieved EDR values, which can be attributed to the used measurement principles, the retrieval technique and/or the sampling scale that is applied. For more details, see chapter 3.

The scanning X-Band radar is able to provide EDR retrievals in rainy/cloudy conditions, but the retrieval techniques are more challenging than for lidar or in situ measurements, as raindrops are not perfect tracers of the air. Based on the radar specifications and scanning strategy, the most optimal manner of remotely retrieving EDR during rain, was determined to be at a low elevation angle, and by using a series of Doppler velocities in a single line of sight, and by applying the most basic EDR retrieval, the variance method. An overview of the applied EDR retrievals, based on the variance of wind velocities, the power spectrum of wind speeds, or structure functions of wind speeds can be found in Chapter 3.

The difficulty with retrieval techniques of turbulence intensity in the atmosphere, is that there are many parameters that can be chosen. For the radar the retrieved variable that is linked most directly to the velocity variations in the atmosphere are the radar mean Doppler velocity and the radar Doppler spectral width. Other variables would be possible, such as variations in temperature, humidity or potentially even radar reflectivity. Having chosen the parameter that is going to be used, the sampling scale at which the energy dissipation rate (EDR) is retrieved becomes important. Often it is not the case that just one single parameter, the energy dissipation rate, is sufficient to describe the turbulence intensity because of the following reasons: 1) small-scale turbulence exists because the measurements are in the wake of a building; or 2) energy is transported in the atmosphere, resulting in more energy dissipation within small areas, such as the surface boundary

layer. In addition, problems with the measurement can exist when the radar is used, because the scatterers themselves (e.g. raindrops) are not perfect tracers of the air. From these notions, the following recommendations for EDR retrieval techniques are formulated, when applied to the radar during rain:

- The sampling scale at which the EDR retrieval is applied should be sufficiently large, such that it can be assumed that the variance of velocities is not influenced by the inertia effect of the scatterers. This is typically more than ~30 m (Chapter 2).

- When different results of EDR retrievals are compared, it has to be assured that only the sampling scale, the retrieval technique or the instrument is changed and not simultaneous.

- For radar measurements from raindrops, using the horizontal direction is more convenient than the vertical. For the vertical direction, an additional corrections has to be made for the terminal fall velocity of the scatterers. In addition, atmospheric structure is more relevant for the vertical direction, which can complicate the EDR retrieval.

Based on this, we can recommend the application of raindrop-backscattering radar-based turbulence intensity retrieval techniques in the following way:

- Use the radar at a low elevation angle and use a series of Doppler velocities from a single line of sight.

- Check the data quality, by looking at the signal to noise ratio (SNR), and the amount of data available in a single line of sight.

A simple analytic formulation to obtain a value for EDR is:

$$\epsilon = \left(\frac{3}{2} C_* \left[\kappa_1^{-2/3} - \kappa_2^{-2/3} \right] \right)^{-3/2} \sigma_T^3. \tag{6.3}$$

where C_* is a Kolmogorov constant, κ are wavenumbers related to the minimal and maximal spatial sampling scales, and σ_T^2 is the variance of radar mean Doppler velocities along the line of sight. Details of how to use this for getting an EDR value is described in Chapter 3 (WSV technique), except that here we apply this technique in the radar line of sight to the line-of-sight radar Doppler velocity measurements.

In Fig. 6.3 the retrieved EDR intensity maps are shown, which can help to enhance the awareness of hazards due to turbulence (e.g. Chan 2011). For the scanning Doppler lidar and the scanning Doppler radar, the variance of measured Doppler mean velocities in the line of sight is used to estimate EDR (Eq. 6.3). Please note that the altitudes of these measurements are shown with circles in the background. An example of a lidar EDR map is shown in Fig. 6.3a. In the vicinity of the airport (< 5 km) and low altitudes (< 500 m), low to moderate turbulence levels are found in this case. With the scanning X-band radar, the measurements are complemented, which is shown in Fig. 6.3b. Some small peak EDR values
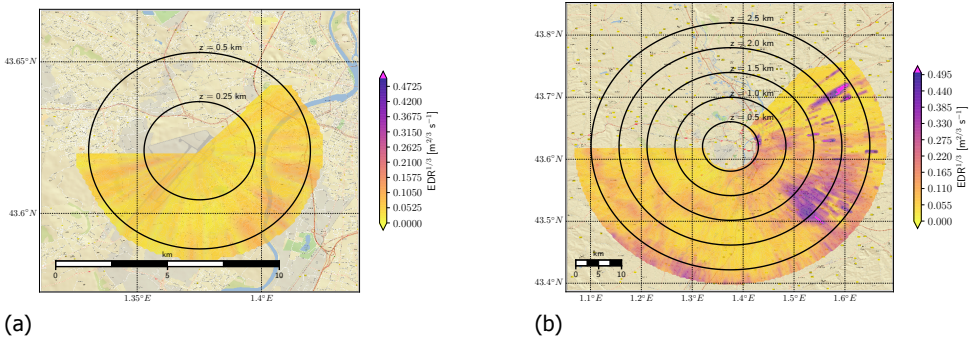
Figure 6.3: Retrieved EDR values during the Toulouse trials on 1412 UTC 24 April 2014 from (a) the scanning Doppler lidar, and from (b) the scanning Doppler radar. EDR values are shown in color contours. The altitudes of the measurements are shown with circles in the background.

observed by the radar likely indicate wake turbulence from buildings, or aircraft wake turbulence, or other small-scale turbulence phenomena. In addition to that, there are large sections with higher EDR values, in this case predominantly in the easterly direction with regard to the airport. The scanning UFO sensors can thus also improve the awareness of hazards due to turbulence, where the scanning X-band radar complements the scanning lidar measurements that are attenuated due to the raindrops.

Although almost identical EDR retrieval techniques have been applied and validated with in situ measurements (e.g. O'Connor et al. 2010; Siebert et al. 2006), it is, nevertheless, desired in future operational applications that the retrieved EDR values from the new types of instruments (scanning lidar and scanning radars) will be further validated and compared to in situ EDR measurements.

6.4. Conclusions

Wind vectors and turbulence intensities have been retrieved from a modern scanning Doppler lidar and a modern scanning X-band radar, to demonstrate the application of EDR retrieval techniques, during trials at the Toulouse-Blagnac airport, within the UFO project. It is expected that such modern scanning Doppler instruments will be widely used at airports in the future to enhance the awareness of wind hazards.

Some recommendations have been defined on how to apply wind vector and EDR retrieval techniques. For a wind retrieval technique, 4D-Var is recommended, as there are advanced processing features, such as the inclusion of prior errors, and the possibility to show the solution space of wind vectors that is associated with the radar Doppler measurements.

For turbulence intensity retrieval techniques applied at airports, it is recommended that the total sample scale is larger than 30 m, to avoid the influence of drop-size-distribution-dependent (DSD) raindrop-inertia corrections. In addition, a low radar-antenna elevation looking angle is recommended, which also avoids the influence of DSD-dependent-terminal-fall-velocity corrections. The DSD dependencies were avoided, as it requires very accurate estimation of the DSD.

With these recommendations, wind vectors and turbulence intensities were successfully retrieved, and the added value of an X-band radar at airports is demonstrated. It is suggested to support long-term measurements at airports, with in situ measurements for validation, to further develop, validate and optimize the retrieval techniques.

7

Conclusions and recommendations

In this work, wind vector and turbulence intensity retrieval techniques for raindrop Doppler radar measurements have been adapted and assessed regarding their accuracy, and when necessary further developed. The problems that have been tackled are:

- The correction for the influence of raindrop inertia in radar-based turbulence intensity retrieval techniques;

- The validation of state-of-the-art velocity-based EDR retrieval techniques, when they are applied to raindrop-backscattering radar measurements;

- Improvement of scanning Doppler radar wind vector retrieval techniques;

- The application of raindrop inertia correction in a radar forward model for improved estimation of EDR; and

- The application of this work to demonstrate the retrieval of EDR and wind vectors at Toulouse-Blagnac airport from scanning X-band radar measurements.

The first problem taken was to estimate the influence of measuring turbulence intensity from imperfect tracers (read: raindrops) with a radar. The raindrop motion can be calculated as an integral of acting forces over its trajectory, which are air friction, gravity and buoyancy. The calculation of such an integral is far too complex in the application of turbulence intensity retrieval techniques, and therefore, simplifications are necessary. Nowadays, well-validated formulas exist for the raindrop terminal fall velocity, based on a balance between the forces acting on a droplet. In this work this theoretical framework has been used when considering an imbalance of forces acting on a raindrop. By starting from the equations of motion and the 'sudden jump' case, inertial parameters were defined with which the

influence of raindrop inertia can be quantified. They resulted in formulas for inertial distance and inertial time for each raindrop size, with different formulations for the x/y-direction and z-direction. These formulas are essential for the development of models that account for the influence of raindrop inertia. A new inertia correction model is proposed, which can be applied to radar-based turbulence intensity retrieval techniques. This model is based on a correction for turbulence scales, given the radar sampling space parameters, raindrop inertial distance and model tuning parameters. Consequently, tuning parameters were estimated for typical raindrop sizes, from turbulent wind velocity field simulations. From the simulations, it was derived that for large total sampling scales ($\gg$ 30 m), the influence of raindrop inertia on radar-based retrieved turbulence intensity becomes negligible. For total sampling scales comparable to or smaller than 30 m, the application of the raindrop-inertia-correction model is suggested. For small radar total sampling scales ($<$ 10 m) and large raindrops (e.g. 4 mm), the application of a turbulence retrieval technique is limited, because the uncertainty in the turbulence intensity correction for the influence of raindrop inertia becomes very large.

In the second problem, energy dissipation rate (EDR) - a measure of turbulence intensity - retrieval techniques are applied to radar measurements during rain. Their accuracy is assessed and estimated. A correction for the influence of raindrop inertia is not taken into account here for two reasons: (1) it can be expected that it is negligible when a large total sampling scale is used, and (2) it is assumed that often a good estimation of the DSD is not available. Two case studies and massive data analysis are applied to a defined set of EDR retrieval techniques that cover commonly used EDR retrieval techniques. To reduce the influence of raindrop inertia, the application of terminal fall velocity corrections was studied and different total sampling scales are used in the techniques. For the TARA radar, it was shown that the best validation results are achieved by using the full 3D wind vector in an EDR retrieval technique with a total sampling time of 10 minutes, which was called the wind speed variance (WSV) EDR retrieval technique. For retrieval techniques that rely on terminal fall velocity corrections, and thus rely on accurate estimation of the DSD, the retrieved EDR values are compromised by errors. Although incorrect estimation of DSD parameters can be easily proven by comparison of the 10 min. averaged radar corrected vertical air velocity with in situ measurements, it remains a challenge to estimate the rain DSD sufficiently accurate for dynamical corrections in turbulence retrieval techniques during the rain with the radar antenna looking vertically. Next to that, it was shown that EDR retrieval techniques have some challenges in their application: the Kolmogorov model is not always applicable, which becomes clear when the same EDR retrieval is applied to in situ measurements to small and large scales, or when averaged spectra of 3D wind speeds are analyzed. A massive data analysis confirmed that the conclusions for the two case studies are also valid for rainy weather in the Netherlands.

In the application of turbulence retrieval techniques to the radar during rain, it is recommended that the concept of EDR is applied cautiously, because of complex estimation errors. It is suggested to always estimate a minimal retrievable EDR, give uncertainty estimates for the retrieved EDR value, and provide the sampling

details of the EDR retrieval technique. In the end, it is then possible to retrieve EDR from the radar measurement during rain, by using the radar measurements in the most optimal way.

The third problem was the improvement of single Doppler radar-based wind vector retrieval techniques. Regarding the influence of raindrop inertia on raindrop-backscattering radar-based wind vector retrieval techniques, it was concluded from a few simulations that only for very special weather conditions a substantial bias - if not corrected for - can be expected. As this work is not aimed at such special weather conditions, the raindrop inertia is not accounted for in wind vector retrieval techniques in this work. Problems with the linear wind model - a state-of-the-art wind vector retrieval technique - that have been identified from a case study are that: (1) the retrieved wind vectors have jumps near the analysis volume edges, and (2) at large distance the retrieved wind vectors become arbitrary and spurious. A new wind vector retrieval technique has been developed and implemented, the so-called four-dimensional variational analysis (4D-Var) wind vector retrieval technique, that provides a more coherent and realistic wind field. With 4D-Var it is possible to show the solution space of wind vectors, which is associated with the radar Doppler measurements. The solution space was demonstrated by two special implementations: the "4D-Var horizontal direction" and the "4D-Var horizontal speed" that give an impression of all possible solutions. By a lack of sufficient in situ wind vector measurements, alternative approaches for quantitative validation of radar-based retrieved wind vectors are proposed. Measures for curl and divergence have been used to identify issues. Such issues are, for example, artificial features in the retrieved wind vector field, related to the implementation and its configuration settings. More research is required, which includes a validation with in situ measurements at multiple locations with respect to the radar to find the most optimal settings for the wind vector retrieval techniques.

The fourth problem is the application of raindrop-backscattering radar-based turbulence intensity retrieval techniques to small scales, in particular the radar resolution volume of modern radars with a high spatial resolution. A non-stochastic turbulence implementation has been developed, the so-called "ensemble of isotropic vectors" approach, which can be used in radar forward models. It has the same dependencies of turbulence intensity in radar observables as stochastic turbulence implementations. A novel feature of this approach is that the polarimetric radar observables, Z_{DR} and L_{DR}, then also depend on turbulence intensity, although a direct usage of such a connection is limited due to various reasons. Further, this model implicitly reproduces the canting angle distribution, which is potentially interesting for further validation studies. This model is also promising for future applications of radar-based retrieval techniques of turbulence intensity and drop size distributions that require a better accuracy for EDR estimation than the state-of-the-art.

In a case study, it was found that the radar-based retrieved DSDs are not yet accurate enough for the estimation of the radar Doppler spectral width component of raindrop terminal fall velocities. The turbulence intensity was too small to measure or, only with in situ ground-level rain DSD estimates, the turbulence intensity profile could be estimated. Turbulence intensity profiles were retrieved from the profiling

radar, given the ground-level in situ DSD, for which it was possible to demonstrate the raindrop inertia correction. Further research is recommended for the improvement of radar-based rain DSDs to allow for a more accurate model estimation of the radar Doppler spectral width.

In the state-of-the-art literature, turbulence and raindrop size distributions are almost never considered together in radar-based retrieval techniques. A good example is a recent article from Beard et al. (2010), which gives an overview of rain DSD retrieval techniques from polarimetric radar measurements, but turbulence is not discussed at all. It is suggested to conduct new experiments regarding raindrop shape, axis ratios and canting angles, but then in combination with in situ turbulence measurements. For example by combining 2-D video disdrometers and sonic anemometers at the same measurement site. Such new experiments will allow for that the influence of turbulence and rain DSD can be studied more independently. The obtained data will also be essential for the validation of new radar forward models, such as the ones that were proposed in this work.

In the last chapter, wind vectors and turbulence intensities were retrieved with modern scanning Doppler instruments at an airport. This was done during trials at the Toulouse-Blagnac airport, within the UFO project. It is expected that such modern scanning Doppler instruments, both lidar and radar, will be widely used at airports in the future. For a wind vector retrieval technique, 4D-Var is recommended, as it has several advanced processing features, and therefore, it gives more control and versatility in the solutions. For turbulence intensity retrieval techniques applied to Doppler radar measurements during rain at airports, it is recommended to avoid corrections for raindrop inertia, as it requires an accurate estimation of the raindrop size distribution. This can be achieved by assuring that the total sampling scale is larger than 30 m, and by using a low radar antenna elevation looking angle. In addition, it is suggested to support long-term Doppler radar measurements at airports, with in situ measurements for validation, to further develop and optimize the retrieval techniques.

References

Atlas, D., R. C. Srivastava, and R. S. Sekhon, 1973: Doppler radar characteristics of precipitation at vertical incidence. *Rev. Geophys. Sp. Phys.*

Barbaresco, F., P. Brovelli, P. Currier, O. Garouste, M. Klein, and P. Juge, 2012: Radar Sensors for Wind & Wake-Vortex Monitoring on Airport : First results of SESAR P12 . 2 . 2 XP0 trials campaign at Paris CDG Airport. *ERAD2012*.

Barbaresco, F., and Coauthors, 2013: Wake vortex detection, prediction and decision support tools in SESAR program. *2013 IEEE/AIAA 32nd Digit. Avion. Syst. Conf.*, 6B1–1–6B1–15.

Beard, K. V., V. N. Bringi, and M. Thurai, 2010: A new understanding of raindrop shape. *Atmos. Res.*

Beard, K. V., and C. Chuang, 1987: A New Model for the Equilibrium Shape of Raindrops. *J. Atmos. Sci.*, **44 (11)**, 1509–1524.

Beard, K. V., and A. R. Jameson, 1983: Raindrop Canting. *J. Atmos. Sci.*, **40 (2)**, 448–454.

Boeing, 2013: Statistical Summary of Commercial Jet Airplane Accidents Worldwide Operations 1959-2012. Tech. rep., Aviation Safety Boeing Commercial Airplanes, Seattle.

Bohne, A. R., 1982: Radar Detection of Turbulence in Precipitation Environments. *J. Atmos. Sci.*, **39 (8)**, 1819–1837.

Borque, P., E. Luke, and P. Kollias, 2016: On the unified estimation of turbulence eddy dissipation rate using Doppler cloud radars and lidars. *J. Geophys. Res. Atmos.*, **121 (10)**, 5972–5989.

Bouniol, D., A. Illingworth, and R. Hogan, 2004: Deriving turbulent kinetic energy dissipation rate within clouds using ground based radar. *Third Eur. Conf. Radar Meteorol.*, 281–285.

Bousquet, O., and M. Chong, 1998: A Multiple-Doppler Synthesis and Continuity Adjustment Technique (MUSCAT) to Recover Wind Components from Doppler Radar Measurements. *J. Atmos. Ocean. Technol.*, **15 (2)**, 343–359.

Bouttier, F., and G. Kelly, 2003: Observing-system experiments in the ECMWF 4D-Var data assimilation system. *Q. J. R. Meteorol. Soc.*

Brandes, E. A., G. Zhang, and J. Vivekanandan, 2003: An evaluation of a drop distribution based rainfall estimator. *J. Appl. Meteor.*

Brandes, E. A., G. Zhang, and J. Vivekanandan, 2004: Comparison of Polarimetric Radar Drop Size Distribution Retrieval Algorithms. *J. Atmos. Ocean. Technol.*, **21 (4)**, 584–598.

Brewster, K. A., and D. S. Zrnić, 1986: Comparison of Eddy Dissipation Rates from Spatial Spectra of Doppler Velocities and Doppler Spectrum Widths. *J. Atmos. Ocean. Technol.*, **3 (3)**, 440–452.

Bringi, V., M. Thurai, and D. Baumgardner, 2018: Raindrop fall velocities from an optical array probe and 2-D video disdrometer. *Atmos. Meas. Tech.*, **11 (3)**, 1377–1384.

Bringi, V., M. Thurai, and D. Brunkow, 2008: Measurements and inferences of raindrop canting angles. *Electron. Lett.*, **44 (24)**, 1425–1426.

Bringi, V. N., and V. Chandrasekar, 2001: *Polarimetric Doppler Weather Radar*. Cambridge University Press, 636 pp.

Bringi, V. N., R. Hoferer, D. A. Brunkow, R. Schwerdtfeger, V. Chandrasekar, S. A. Rutledge, J. George, and P. C. Kennedy, 2011: Design and Performance Characteristics of the New 8.5-m Dual-Offset Gregorian Antenna for the CSU-CHILL Radar. *J. Atmos. Ocean. Technol.*, **28 (7)**, 907–920.

Brost, R. A., J. C. Wyngaard, and D. H. Lenschow, 1982: Marine Stratocumulus Layers. Part II: Turbulence Budgets. *J. Atmos. Sci.*, **39 (4)**, 818–836.

Brown, R. A., and V. T. Wood, 2007: *A guide for interpreting Doppler velocity patterns: northern hemisphere edition*. NOAA/National Severe Storms Laboratory.

Bryant, G. W., and K. A. Browning, 1975: Multi-level measurements of turbulence over the sea during the passage of a frontal zone. *Q. J. R. Meteorol. Soc.*, **101 (427)**, 35–54.

Careta, A., and F. Sagues, 1993: Stochastic generation of homogeneous isotropic turbulence with well-defined spectra. *Phys. Rev. E.*

Casso-Torralba, P., J. V. G. de Arellano, F. Bosveld, M. R. Soler, A. Vermeulen, C. Werner, and E. Moors, 2008: Diurnal and vertical variability of the sensible heat and carbon dioxide budgets in the atmospheric surface layer. *J. Geophys. Res. Atmos.*, **113 (12)**.

Caughey, S. J., J. C. Wyngaard, and J. C. Kaimal, 1979: Turbulence in the Evolving Stable Boundary Layer. *J. Atmos. Sci.*, **36 (6)**, 1041–1052.

Chan, P. W., 2011: Generation of an eddy dissipation rate map at the Hong Kong International Airport based on Doppler lidar data. *J. Atmos. Ocean. Technol.*, **28 (1)**, 37–49.

Chong, M., and S. Cosma, 2000: A Formulation of the Continuity Equation of MUS-CAT for either Flat or Complex Terrain. *J. Atmos. Ocean. Technol.*, **17 (11)**, 1556–1565.

Chong, M., and J. Testud, 1983: Three-Dimensional Wind Field Analysis from Dual-Doppler Radar Data. Part III: The Boundary Condition: An Optimum Determination Based on a Variational Concept. *J. Clim. Appl. Meteorol.*, **22 (7)**, 1227–1241.

Chong, M., and Coauthors, 2000: Real–Time Wind Synthesis from Doppler Radar Observations during the Mesoscale Alpine Programme. *Bull. Am. Meteorol. Soc.*, **81 (12)**, 2953–2962.

Davis, T. A., 2006: *Direct Methods for Sparse Linear Systems*. Society for Industrial & Applied Mathematics,U.S.

De Wolf, D. A., H. W. J. Russchenberg, and L. P. Ligthart, 1990: Effective permittivity of and scattering from wet snow and ice droplets at weather radar wavelengths. *IEE Trans. antennas Propag.*

Dolfi-Bouteyre, A., and Coauthors, 2009: Aircraft Wake Vortex Study and Characterization with 1.5 μm Fiber Doppler Lidar. *AerospaceLab*, 1–13.

Donovan, D. P., R. H. Voors, G. J. van Zadelhoff, J. R. Acarreta, D. S. SL, R. de Poniente, and T. Cantos, 2008: ECSIM Models and Algorithms Document. Tech. rep., Royal Netherlands Meteorological Institute (KNMI).

Doviak, R. J., D. S. Zrnic, and D. S. Sirmans, 1979: Doppler weather radar. *Proc. IEEE*, **67 (11)**, 1522–1553.

Doviak, R. J., and D. S. Zrnić, 1993: *Doppler radar and weather observations*. 2nd ed., Academic Press, San Diego.

Doxiadēs, A. K., C. H. Papadimitriou, A. Papadatos, and A. Di Donna, 2009: *Logicomix : an epic search for truth*. Bloomsbury, New York.

Fabry, F., 2010: Radial velocity measurement simulations: common errors, approximations, or omissions and their impact on estimation accuracy. *ERAD2010*.

Fang, M., B. A. Albrecht, V. P. Ghate, and P. Kollias, 2014: Turbulence in Continental Stratocumulus, Part I: External Forcings and Turbulence Structures. *Boundary-Layer Meteorol.*, **150 (3)**, 341–360.

Figueras i Ventura, J., 2009: *Design of a High Resolution X-band Doppler Polarimetric Weather Radar, PhD thesis, TU-Delft*. TU-Delft, Delft.

Frech, M., 2007: Estimating the turbulent energy dissipation rate in an airport environment. *Boundary-Layer Meteorol.*, **123 (3)**, 385–393.

Frehlich, R., S. M. Hannon, and S. W. Henderson, 1998: Coherent Doppler Lidar Measurements of Wind Field Statistics. *Boundary-Layer Meteorol.*, **86 (2)**, 233–256.

Friedrich, K., and M. Hagen, 2004: Evaluation of Wind Vectors Measured by a Bistatic Doppler Radar Network. *J. Atmos. Ocean. Technol.*, **21 (12)**, 1840–1854.

Frisch, A. S., and R. G. Strauch, 1976: Doppler Radar Measurements of Turbulent Kinetic Energy Dissipation Rates in a Northeastern Colorado Convective Storm. *J. Appl. Meteorol.*, **15 (9)**, 1012–1017.

Gao, J., M. Xue, K. Brewster, and K. K. Droegemeier, 2004: A Three-Dimensional Variational Data Analysis Method with Recursive Filter for Doppler Radars. *J. Atmos. Ocean. Technol.*, **21 (3)**, 457–469.

Gao, J., M. Xue, A. Shapiro, and K. K. Droegemeier, 1999: A Variational Method for the Analysis of Three-Dimensional Wind Fields from Two Doppler Radars. *Mon. Weather Rev.*, **127 (9)**, 2128–2142.

Gao, J., M. Xue, A. Shapiro, Q. Xu, and K. K. Droegemeier, 2001: Three-Dimensional Simple Adjoint Velocity Retrievals from Single-Doppler Radar. *J. Atmos. Ocean. Technol.*, **18 (1)**, 26–38.

Gerz, T., F. Holzäpfel, W. Bryant, F. Köpp, M. Frech, A. Tafferner, and G. Winckelmans, 2005: Research towards a wake-vortex advisory system for optimal aircraft spacing. *Comptes Rendus Phys.*, **6 (4-5)**, 501–523.

Gossard, E. E., 1990: Radar Research on the Atmospheric Boundary Layer. *Radar Meteorol.*, D. Atlas, Ed., American Meteorological Society, Boston, MA, 477–527.

Haynes, J. M., Z. Luo, G. L. Stephens, R. T. Marchand, and A. Bodas-Salcedo, 2007: A Multipurpose Radar Simulation Package: QuickBeam. *Bull. Am. Meteorol. Soc.*, **88 (11)**, 1723–1727.

Heijnen, S., L. Ligthart, and H. Russchenberg, 2000: First measurements with TARA; An S-Band transportable atmospheric radar. *Phys. Chem. Earth, Part B Hydrol. Ocean. Atmos.*, **25 (10-12)**, 995–998.

Hocking, W., 1986: Observation and measurement of turbulence in the middle atmosphere with a VHF radar. *J. Atmos. Terr. Phys.*, **48 (7)**, 655–670.

Hoerl, R. W., R. D. Snee, and R. D. De Veaux, 2014: Applying statistical thinking to 'Big Data' problems. *Comput. Stat.*

Hogan, R. J., and S. F. Kew, 2005: A 3D stochastic cloud model for investigating the radiative properties of inhomogeneous cirrus clouds. *Q. J. R. Meteorol. Soc.*

Holton, J. R., 2001: *An introduction to dynamic meteorology*. Academic Press.

Holzäpfel, F., 2006: Probabilistic Two-Phase Aircraft Wake-Vortex Model: Further Development and Assessment. *J. Aircr.*, **43 (3)**, 700–708.

ICAO, 2007a: Annex 3 to the Convention on International Civil Aviation. Tech. rep., International Civil Aviation Organization.

ICAO, 2007b: Procedures for air navigation services - Air traffic management. Tech. Rep. Doc 4444 AMT/501, International Civil Aviation Organization.

Illingworth, A. J., D. Cimini, C. Gaffard, M. Haeffelin, V. Lehmann, U. Löhnert, E. J. O'Connor, and D. Ruffieux, 2015: Exploiting Existing Ground-Based Remote Sensing Networks to Improve High-Resolution Weather Forecasts. *Bull. Am. Meteorol. Soc.*, **96 (12)**, 2107–2125.

Johnson, S. G., 2017: The NLopt nonlinear-optimization package. GitHub, [Available online at http://ab-initio.mit.edu/nlopt].

Kaimal, J. C., J. C. Wyngaard, D. A. Haugen, O. R. Coté, Y. Izumi, S. J. Caughey, and C. J. Readings, 1976: Turbulence Structure in the Convective Boundary Layer. *J. Atmos. Sci.*, **33 (11)**, 2152–2169.

Katul, G. G., 1994: A model for sensible heat flux probability density function for near-neutral and slightly-stable atmospheric flows. *Boundary-Layer Meteorol.*, **71 (1)**, 1–20.

Kettenring, J. R., 2009: Massive datasets. *Wiley Interdiscip. Rev. Comput. Stat.*, **1 (1)**, 25–32.

Khvorostyanov, V. I., and J. A. Curry, 2005: Fall Velocities of Hydrometeors in the Atmosphere: Refinements to a Continuous Analytical Power Law. *J. Atmos. Sci.*, **62 (12)**, 4343–4357.

Klazura, G. E., and D. A. Imy, 1993: A Description of the Initial Set of Analysis Products Available from the NEXRAD WSR-88D System. *Bull. Am. Meteorol. Soc.*, **74 (7)**, 1293–1311.

Kollias, P., and B. Albrecht, 2000: The turbulence structure in a continental stratocumulus cloud from millimeter-wavelength radar observations. *J. Atmos. Sci.*, **57 (8)**, 2417–2434.

Kollias, P., B. A. Albrecht, R. Lhermitte, and A. Savtchenko, 2001: Radar Observations of Updrafts, Downdrafts, and Turbulence in Fair-Weather Cumuli. *J. Atmos. Sci.*, **58 (13)**, 1750–1766.

Kolmogorov, A., 1941: Dissipation of Energy in Locally Isotropic Turbulence. *Akad. Nauk SSSR Dokl.*, **32**, 16.

Kolmogorov, A. N., 1991: Dissipation of Energy in the Locally Isotropic Turbulence. *Proc. R. Soc. A Math. Phys. Eng. Sci.*, **434 (1890)**, 15–17.

Kongara, S., R. Calhoun, A. Choukulkar, and M.-O. Boldi, 2012: Velocity retrieval for coherent Doppler lidar. *Int. J. Remote Sens.*, **33 (11)**, 3596–3613.

Kopken, C., G. Kelly, and J. Thepaut, 2003: Assimilation of Meteosat radiance data within the 4D-Var system at ECMWF: Assimilation experiments and forecast impact. *Q. J. R. Meteorol. Soc.*

Kowalewski, S., and G. Peters, 2010: Analysis of Z–R Relations Based on LDR Signatures within the Melting Layer. *J. Atmos. Ocean. Technol.*, **27 (9)**, 1555–1561.

Krasnov, O. A., L. P. Ligthart, Z. Li, P. Lys, and F. van der Zwan, 2008: The PARSAX - full polarimetric FMCW radar with dual-orthogonal signals. *2008 Eur. Radar Conf.*, IEEE, 84–87.

Krishnamurthy, R., A. Choukulkar, R. Calhoun, J. Fine, A. Oliver, and K. Barr, 2013: Coherent Doppler lidar for wind farm characterization. *Wind Energy*, **16 (2)**, 189–206.

Lamer, K., and P. Kollias, 2015: Observations of fair-weather cumuli over land: Dynamical factors controlling cloud size and cover. *Geophys. Res. Lett.*, **42 (20)**, 8693–8701.

Lemone, M. A., and W. T. Pennell, 1979: A Comparison of Turbulence Measurements from Aircraft. *J. Appl. Meteorol.*, **19 (12)**, 1420–1437.

Liu, X., P. K. Bhartia, K. Chance, R. J. Spurr, and T. P. Kurosu, 2010: Ozone profile retrievals from the ozone monitoring instrument. *Atmos. Chem. Phys.*, **10 (5)**, 2521–2537.

MacCready, P. B. J., 1964: Standardization of Gustiness Values from Aircraft. *J. Appl. Meteorol.*, **3**, 439–449.

Manić, S. B., M. Thurai, V. N. Bringi, and B. M. Notaroš, 2018: Scattering Calculations for Asymmetric Raindrops during a Line Convection Event: Comparison with Radar Measurements. *J. Atmos. Ocean. Technol.*, **35 (6)**, 1169–1180.

Mann, J., 1998: Wind field simulation. *Probabilistic Eng. Mech.*, **13 (4)**, 269–282.

Mardia, K. V., and P. E. Jupp, 1999: *Directional Statistics*. 2nd ed., Academic Press, London, 456 pp.

Marsden, J. E., and A. Tromba, 2003: *Vector calculus*. Macmillan.

Marshall, J. S., and W. M. K. Palmer, 1948: the Distribution of Raindrops With Size. *J. Meteorol.*, **5 (4)**, 165–166.

Mather, G., 2009: *Foundations of sensation and perception*. Second edi ed., Psychology Press, Hove, East Sussex, UK.

Meagher, J. P., and Z. S. Haddad, 2006: To What Extent Can Raindrop Size Be Determined by a Multiple-Frequency Radar? *J. Appl. Meteorol. Climatol.*, **45 (4)**, 529–536.

Mishchenko, M., L. Travis, and A. Lacis, 2002: *Scattering, Absorption, and Emission of Light by Small Particles*. Cambridge University Press.

Mishchenko, M. I., 2000: Calculation of the Amplitude Matrix for a Nonspherical Particle in a Fixed Orientation. *Appl. Opt.*, **39 (6)**.

Nastrom, G. D., 1997: Doppler radar spectral width broadening due to beamwidth and wind shear. *Ann. Geophys.*, **15 (6)**, 786–796.

Nastrom, G. D., and F. D. Eaton, 1997: Turbulence eddy dissipation rates from radar observations at 5-20 km at White Sands Missile Range, New Mexico. *J. Geophys. Res. Atmos.*, **102 (D16)**, 19 495–19 505.

Nicholls, S., 1978: Measurements of turbulence by an instrumented aircraft in a convective atmospheric boundary layer over the sea. *Q. J. R. Meteorol. Soc.*, **104 (441)**, 653–676.

Nucciarone, J. J., and G. S. Young, 1991: Aircraft Measurements of Turbulence Spectra in the Marine Stratocumulus-topped Boundary Layer. *J. Atmos. Sci.*, **48 (22)**, 2382–2392.

O'Connor, E. J., A. J. Illingworth, I. M. Brooks, C. D. Westbrook, R. J. Hogan, F. Davies, and B. J. Brooks, 2010: A Method for Estimating the Turbulent Kinetic Energy Dissipation Rate from a Vertically Pointing Doppler Lidar, and Independent Evaluation from Balloon-Borne In Situ Measurements. *J. Atmos. Ocean. Technol.*, **27 (10)**, 1652–1664.

Otto, T., and H. W. J. Russchenberg, 2010: High-resolution polarimetric X-band weather radar observations at the Cabauw Experimental Site for Atmospheric Research. *Geosci. data J.*

Oude Nijhuis, A. C. P., 2016: CEWE. GitHub, [Available online at https://github.com/albertoudenijhuis/cewe].

Oude Nijhuis, A. C. P., 2017: Zephyros: software package for the development of radar based wind vector and turbulence intensity retrieval techniques. GitHub, [Available online at https://github.com/albertoudenijhuis/zephyros0.4].

Oude Nijhuis, A. C. P., O. A. Krasnov, A. G. Yarovoy, C. M. H. Unal, and H. W. J. Russchenberg, 2016a: Implementation of wind vector and turbulence intensity retrievals: Application to fast scanning X-band radar. *2016 IEEE Metrol. Aerosp.*, Florence, 113–117.

Oude Nijhuis, A. C. P., C. M. H. Unal, O. A. Krasnov, H. W. J. Russchenberg, and A. G. Yarovoy, 2014a: Outlook for a new wind field retrieval technique: The 4D-Var wind retrieval. *Int. Radar Conf.*, 1–6.

Oude Nijhuis, A. C. P., C. M. H. Unal, O. A. Krasnov, H. W. J. Russchenberg, and A. G. Yarovoy, 2014b: Simulation of atmospheric turbulence: Fractal turbulence (Poster). *21st Symp. Bound. Layers Turbul.*

Oude Nijhuis, A. C. P., C. M. H. Unal, O. A. Krasnov, H. W. J. Russchenberg, and A. G. Yarovoy, 2018a: Velocity-based EDR retrieval techniques applied to Doppler radar measurements from rain: Two case studies (under review). *J. Atmos. Ocean. Technol.*, **- (-)**, –.

Oude Nijhuis, A. C. P., F. J. Yanovsky, O. Krasnov, C. M. H. Unal, H. W. J. Russchenberg, and A. G. Yarovoy, 2016b: Assessment of the rain drop inertia effect for radar-based turbulence intensity retrievals. *Int. J. Microw. Wirel. Technol.*, **8 (6)**, 835–844.

Oude Nijhuis, A. C. P., and Coauthors, 2018b: Wind hazard and turbulence monitoring at airports with lidar, radar and Mode-S downlinks: The UFO Project. *Bull. Am. Meteorol. Soc.*, **99 (11)**, 2275–2293.

Petty, G. W., 2006: *A First Course in Atmospheric Radiation (2nd Ed.)*. 2nd ed., Sundog Publishing, Madison, WI, 472 pp.

Pinsky, M., and A. Khain, 2006: A model of a homogeneous isotropic turbulent flow and its application for the simulation of cloud drop tracks. *Geophys. Astrophys. Fluid Dyn.*

Piper, M., and J. K. Lundquist, 2004: Surface Layer Turbulence Measurements during a Frontal Passage. *J. Atmos. Sci.*, **61 (14)**, 1768–1780.

Pope, S. B., 2000: *Turbulent Flows*. Cambridge University Press, New York, 801 pp.

Pozar, D. M., 2009: *Microwave engineering*. John Wiley & Sons.

Rees, W. G., 2012: *Physical Principles of Remote Sensing*. 3rd ed., Cambridge University Press, Cambridge.

Richards, M., J. Scheer, and W. Holm, 2010: *Principles of Modern Radar: Basic Principles*. SciTech Publishing, Chelsea, MI.

Rodgers, C. D., 2000: *Inverse methods for atmospheric sounding - Theory and practive, vol. 2 of Atmospheric, Oceanic and Planetary Physics, World Scientific, Singapore*.

Rogers, R. R., and B. R. Tripp, 1964: Some Radar Measurements of Turbulence in Snow. *J. Appl. Meteor.*, **3 (5)**, 603–610.

Röhner, L., and K. Träumner, 2013: Aspects of Convective Boundary Layer Turbulence Measured by a Dual-Doppler Lidar System. *J. Atmos. Ocean. Technol.*, **30 (9)**, 2132–2142.

Ryzhkov, A., M. Pinsky, A. Pokrovsky, and A. Khain, 2010: Polarimetric Radar Observation Operator for a Cloud Model with Spectral Microphysics. *J. Appl. Meteorol. Climatol.*, **50 (4)**, 873–894.

Satoh, S., and J. Wurman, 2003: Accuracy of Wind Fields Observed by a Bistatic Doppler Radar Network. *J. Atmos. Ocean. Technol.*, **20 (8)**, 1077–1091.

Shupe, M. D., I. M. Brooks, and G. Canut, 2012: Evaluation of turbulent dissipation rate retrievals from Doppler Cloud Radar. *Atmos. Meas. Tech.*, **5 (6)**, 1375–1385.

Siebert, H., K. Lehmann, and M. Wendisch, 2006: Observations of Small-Scale Turbulence and Energy Dissipation Rates in the Cloudy Boundary Layer. *J. Atmos. Sci.*, **63 (5)**, 1451–1466.

Stout, J. E., S. P. Arya, and E. L. Genikhovich, 1995: The Effect of Nonlinear Drag on the Motion and Settling Velocity of Heavy Particles. *J. Atmos. Sci.*, **52 (22)**, 3836–3848.

Sutton, O. G., 1953: *Micrometeorology: a study of physical processes in the lowest layers of the earth's atmosphere*. McGraw-Hill, New York.

Takis, K., M. Philip, and J. W, 2014: In situ disdrometer calibration using multiple DSD moments. *Acta Geophys.*, **62**, 1450.

Taylor, G. I., 1938: The Spectrum of Turbulence. *Proc. R. Soc. Lond. A. Math. Phys. Sci.*, **164 (919)**, 476–490.

Taylor, J. R., 1997: *An introduction to error analysis: The study of uncertainties in physical measurements, second edition*. University Science Books, Sausalito, California.

Thiermann, V., and H. Grassl, 1992: The measurement of turbulent surface-layer fluxes by use of bichromatic scintillation. *Boundary-Layer Meteorol.*, **58 (4)**, 367–389.

Tokay, A., D. B. Wolff, and W. A. Petersen, 2014: Evaluation of the New Version of the Laser-Optical Disdrometer, OTT Parsivel2. *J. Atmos. Ocean. Technol.*, **31 (6)**, 1276–1288.

Ulden, A. P., and J. Wieringa, 1996: Atmospheric boundary layer research at Cabauw. *Boundary-Layer Meteorol.*, **78 (1-2)**, 39–69.

Unal, C., 2015: High-resolution raindrop size distribution retrieval based on the Doppler spectrum in the case of slant profiling radar. *J. Atmos. Ocean. Technol.*, **32 (6)**, 1191–1208.

Unal, C., Y. Dufournet, T. Otto, and H. Russchenberg, 2012: The new real-time measurement capabilities of the profiling TARA radar. *Seventh Eur. Conf. radar Meteorol. Hydrol.*

Unal, C. M. H., and D. N. Moisseev, 2004: Combined Doppler and polarimetric radar measurements: Correction for spectrum aliasing and nonsimultaneous polarimetric measurements. *J. Atmos. Ocean. Technol.*, **21 (3)**, 443–456.

Ventura, J. F. I., and H. W. J. Russchenberg, 2006: IDRA: IRCTR Drizzle Radar. *2006 Eur. Radar Conf.*, 174–177.

Vlcek, J., and L. Luksan, 2006: Shifted limited-memory variable metric methods for large-scale unconstrained minimization. *J. Comput. Appl. Math.*

Voors, R., and Coauthors, 2007: ECSIM: the simulator framework for EarthCARE. *Sensors, Syst. Next-Generation Satell. XI*, Vol. 6744, 11.

Wagner, R., and M. Courtney, 2014: Scanning LIDAR Verification Study - DTU Report. Tech. rep., Technical University of Denmark.

White, A. B., R. J. Lataitis, and R. S. Lawrence, 1999: Space and Time Filtering of Remotely Sensed Velocity Turbulence. *J. Atmos. Ocean. Technol.*, **16 (12)**, 1967–1972.

Wieringa, J., 1980: Representativeness of wind observations at airports. *Bull. Am. Meteorol. Soc.*, **61 (9)**, 962–971.

Wilson, R., 2004: Turbulent diffusivity in the free atmosphere inferred from MST radar measurements: a review. *Ann. Geophys.*, **22 (11)**, 3869–3887.

Yanovsky, F., 1996: Simulation study of 10 GHz radar backscattering from clouds, and solution of the inverse problem of atmospheric turbulence measurements. *3rd Int. Conf. Comput. Electromagn. (CEM 96)*, IEE, Vol. 1996, 188–193.

Yanovsky, F., I. Prokopenko, K. Prokopenko, H. Russchenberg, and L. Ligthart, 2002: Radar estimation of turbulence eddy dissipation rate in rain. *IEEE Int. Geosci. Remote Sens. Symp.*, IEEE, Vol. 1, 63–65.

Yanovsky, F., H. Russchenberg, and C. Unal, 2005: Retrieval of information about turbulence in rain by using Doppler-polarimetric Radar. *IEEE Trans. Microw. Theory Tech.*, **53 (2)**, 444–450.

Yanovsky, F. J., 2002: Doppler-polarimetric retrieval of rain rate and turbulence intensity in precipitation. *Proc. Int. Conf. Math. Methods Electromagn. Theory, MMET '02*, Kiev, Vol. 1, 281–286.

Yanovsky, F. J., H. W. J. Russchenberg, and C. M. H. Unal, 2003: Doppler-polarimetric radar observations of turbulence in rain. Tech. rep., IRCTR, Delft.

Yanovsky, F. J., D. M. Turenko, A. C. P. Oude Nijhuis, O. A. Krasnov, and A. G. Yarovoy, 2015: A new model for retrieving information about turbulence intensity from radar signal. *2015 Signal Process. Symp.*, IEEE, 1–6.

Zhang, G., J. Vivekanandan, and E. Brandes, 2001: A method for estimating rain rate and drop size distribution from polarimetric radar measurements. *IEEE Trans. Geosci. Remote Sens.*, **39 (4)**, 830–841.

Zhou, M. Y., D. H. Lenschow, B. B. Stankov, J. C. Kaimal, and J. E. Gaynor, 1985: Wave and Turbulence Structure in a Shallow Baroclinic Convective Boundary Layer and Overlying Inversion. *J. Atmos. Sci.*, **42 (1)**, 47–57.

Acknowledgments

First, I would like to thank all the members of my doctoral committee for validating my research work. A large gratitude goes to my supervisory team consisting of my promotors Alexander Yarovoy and Herman Russchenberg, copromotor Oleg Krasnov, and supervisor Christine Unal. They have given me the opportunity to conduct this PhD research. I am thankful for their encouragement, patience and guidance. By having four supervisors, I have been in a privileged position as a PhD researcher to receive abundant feedback from different perspectives, which helped to improve my work significantly.

I am grateful to the EU FP7 program, the UltraFast Observations (UFO) project, which supported my research. By sharing knowledge with many colleagues from different research institutes and companies in this European project, the scientific level of my work was elevated. In particular collaboration with Ludovic Thobois (Leosphere), Frederic Barbaresco (Thales Air Systems), Siebren De Haan (Royal Netherlands Meteorological Institute, KNMI), Agnes Dolfi-Bouteyre (ONERA), Dmitry Kovalev (Université catholique de Louvain, UCL), Danielle Vanhoenacker-Janvier (UCL) and Richard Wilson (Université Pierre et Marie Curie, UPMC) was special for me as it has given me the opportunity to assemble the UFO project results in a scientific journal article for the Bulletin of the American Meteorological Society (BAMS).

I would like to convey my thanks to colleagues and friends from the MS3 group: Alexey Narykov, Alvaro Blanco Campo, Arun Muraleedharan, Dario Petri, Dinh Tran, Dmytro Penkin, Esther de Klerk, Etienne Goossens, Faruk Uysal, Fotios Katsilieris, Francesco Belfiori, Francois le Chevalier, Fred van der Zwan, Hans Driessen, Inna Ivashko, Jan Puskely, Jianping Wang, Minke van der Put, Nikita Petrov, Nikola Bogdanovic, Pascal Aubry, Rossiza Gourova, Sharef Neemat, Shenario Amaldoss, Shilong Sun, Shravan Shirodkar, Stefano Medagli, Takuya Sakamoto, Teun de Groot, Xuan Wang, Yanki Aslan and Yuan He. They have all played different roles, varying from a supporting or a critical colleague, which lead to the success of my PhD. Also, without them the office life would have been rather gaunt.

I would also like to show my gratitude to colleagues and friends from the ATMOS group: Dimitra Mamali, Edouard Martins, Harm Jonker, Igor Stepanov, Jiapeng Yin, Julien Chimot, Marc Schleiss, Lukas Pfitzenmaier, Ricardo Reinoso Rondinel, Tim Vlemmix, Yann Dufournet and Yunlong Li. Thank you for your support and helpful feedback on my work!

In particular I would like to thank Felix Yanovsky with whom I have had many discussions on my work. Thanks to his support, I was able to get acquainted with the state-of-the-art in a fast way. Due to Fred Bosveld, I was able to use and comprehend the sonic anemometer data from the Cabauw research site for in situ validation of turbulence intensity from the TARA radar. It has to be said that observatories with long-term data records are struggling to survive politically

A

Coordinate systems

In this appendix the equations for coordinate system transformations are provided. For radar and lidar simulation, five coordinate systems are relevant in this work. The following abbreviations are used for them: WGS84, ECEF, ENU, AZEL and BEAM. A short overview is given below, and after that the details of the coordinate transformations are given. Only the essential parameters and equations are given, and for more information we refer to the literature on coordinate systems. For a large part, this information has been adapted from *Wikipedia*, see `http://en.wikipedia.org/wiki/Geographic_coordinate_conversion`.

- **WGS84**: The World Geodetic System (WGS) is a standard for use in cartography, geodesy, and navigation. It comprises a standard coordinate system for the Earth, a standard spheroidal reference surface (the datum or reference ellipsoid) for raw altitude data, and a gravitational equipotential surface (the geoid) that defines the nominal sea level. The position of an object is described by the geodetic coordinates that are latitude ϕ, longitude λ and height h.

- **ECEF**: The Earth-Centered Earth-Fixed coordinate system, also known as the Earth Centered Rotational (ECR) coordinate system, is a Cartesian coordinate system and is sometimes known as a "conventional terrestrial" system. It represents positions as (X, Y, Z) coordinates. The point (0,0,0) is defined as the center of mass of the Earth, hence the name "Earth-Centered´´.

- **ENU**: This is the local East, North, Up (ENU) coordinate system. In many targeting and tracking applications, the ENU Cartesian coordinate system is far more intuitive and practical than ECEF or Geodetic coordinates. The local ENU coordinates are formed from a plane tangent to the Earth's surface that is fixed to a specific location. Therefore, it is known as a "local tangent" or "local geodetic" plane coordinate system. By convention the east axis is labeled x, the north y and the up z.

143

- **AZEL**: This is the AZimuth-ELevation coordinate system, also known as the radar instrument coordinates or the horizontal coordinate system, which consists of the instrument antenna looking angles. The coordinates for a point in space are the azimuth angle α, the elevation angle γ and the range r. The elevation is the angle of the antenna looking direction with regards to the surface, and the azimuth angle is the angle between the antenna looking direction and the north. The azimuth is then positively increasing for the east, the south and the west, respectively.

- **BEAM**: This is the radar beam coordinate system, which describes points in space with regards to a given reference radar antenna looking direction. The beam coordinates are the offset angle θ (with regards to the center beam), the azimuth angle ϕ, and the range r. It is thus a spherical coordinate system, where $\theta = 0$ for the center of the beam, and for increasing θ the points in space go away from the radar beam center. This coordinates system is in particular useful for spatial integrations, such as integration over a radar antenna power distribution pattern.

A.1. WGS84

The World Geodetic System (WGS) is a standard for use in cartography, geodesy, and navigation. It comprises a standard coordinate system for the Earth, a standard spheroidal reference surface (the datum or reference ellipsoid) for raw altitude data, and a gravitational equipotential surface (the geoid) that defines the nominal sea level. The position of an object is described by the geodetic coordinates that are the latitude ϕ, the longitude λ and the height h. The WGS84 defining parameters are:

$$a = 6378137.0, \tag{A.1}$$
$$1/f = 298.257223563, \tag{A.2}$$

where a [m] is the semi-major axis, and f [-] is the flattening. From these parameters, the parameters that follow are:

$$b = a(1 - f), \tag{A.3}$$
$$e^2 = 1 - b^2/a^2 = 2f - f^2, \tag{A.4}$$

where b is the semi-minor axis, and e the first eccentricity. The parameters are necessary for coordinate transformations that will follow.

A.2. ECEF

ECEF (Earth-Centered, Earth-Fixed), also known as ECR (Earth Centered Rotational), is a Cartesian coordinate system, and is sometimes known as a "conventional terrestrial" system. It represents positions as (X, Y, Z) coordinates. The point (0,0,0) is defined as the center of mass of the Earth. Hence the name Earth-Centered.

WGS84 to ECEF   Geodetic coordinates (latitude ϕ, longitude λ, height h) can be converted into ECEF coordinates by using the following formulas:

$$X = (N(\phi) + h) \cos \phi \cos \lambda, \tag{A.5}$$
$$Y = (N(\phi) + h) \cos \phi \sin \lambda, \tag{A.6}$$
$$Z = (N(\phi)(1 - e^2) + h) \sin \phi, \tag{A.7}$$

where the normal N is defined as:

$$N = a/\sqrt{1 - e^2 \sin^2 \phi}. \tag{A.8}$$

ECEF to WGS84   The conversion of ECEF coordinates to WGS84 geodetic coordinates is a much harder problem. There exist two kinds of methods in order to solve the Bowring's irrational geodetic-latitude equation:

$$\kappa - 1 - \frac{e^2 a \kappa}{\sqrt{p^2 + (1 - e^2)z^2 \kappa^2}} = 0, \tag{A.9}$$

with

$$\kappa = \frac{p}{z} \tan \phi \text{ and } p^2 = X^2 + Y^2. \tag{A.10}$$

   Newton-Raphson method. The Bowring's irrational geodetic-latitude equation is efficiently solved by the Newton-Raphson iteration method: The algorithm starts with κ_0:

$$\kappa_0 = (1 - e^2)^{-1}. \tag{A.11}$$

Consequently, the solution is found by convergence of the following equations:

$$c_i = \frac{(p^2 + (1 - e^2)z^2 k_i^2)^{3/2}}{ae^2}, \tag{A.12}$$
$$\kappa_{i+1} = \frac{c_i + (1 - e^2)z^2 \kappa_i^3}{c_i - p^2}. \tag{A.13}$$

In the end, the height, longitude and latitude are calculated as:

$$\lambda_0 = \tan^{-1} y/x, \tag{A.14}$$

$$\lambda = \begin{cases} \lambda_0 & \text{for} & x >= 0 \\ \lambda_0 + \pi & \text{for} & x < 0 \text{ and } \lambda_0 < 0 \\ \lambda_0 - \pi & \text{for} & x < 0 \text{ and } \lambda_0 > 0. \end{cases} \tag{A.15}$$

And finally:

$$\phi = \tan^{-1} \frac{\kappa z}{p}, \tag{A.16}$$
$$h = e^{-2}(\kappa^{-1} - \kappa_0^{-1})\sqrt{p^2 + z^2 \kappa^2}. \tag{A.17}$$

In Eq. A.16, the inverse tangent is typically implemented with the 'atan2' function to get the right sign.

Ferrari's solution. An alternative is Ferrari's solution, which uses the following formulas to get a solution:

$$\zeta = (1 - e^2)z^2/a^2, \tag{A.18}$$

$$\rho = (p^2/a^2 + \zeta - e^4)/6, \tag{A.19}$$

$$s = e^4\zeta p^2/(4a^2), \tag{A.20}$$

$$t = (\rho^3 + s + \sqrt{s(s + 2\rho^3)})^{1/3}, \tag{A.21}$$

$$u = \rho + t + \rho^2/t, \tag{A.22}$$

$$v = \sqrt{u^2 + e^4\zeta}, \tag{A.23}$$

$$w = e^2(u + v - \zeta)/(2v), \tag{A.24}$$

$$\kappa = 1 + e^2(\sqrt{u + v + w^2} + w)/(u + v). \tag{A.25}$$

A.3. ENU

The local ENU coordinates are formed from a plane tangent to the Earth's surface fixed to a specific location. Hence it is sometimes known as a "local tangent" or "local geodetic" plane. By convention, the east axis is labeled x, the north y and the up z.

Conversion from and to the ECEF coordinate system is obtained via the following coordinate transformations. Here ϕ and λ are the WGS84 coordinates for the center of the ENU system, (X_r, Y_r, Z_r) are the ECEF coordinates for the center of the ENU system, and (x,y,z) are the ENU coordinates.

ECEF to ENU Given the reference coordinates, this coordinate transformation is obtained via the application of a rotation matrix:

$$\begin{pmatrix} x \\ y \\ z \end{pmatrix} = \begin{pmatrix} -\sin\lambda & \cos\lambda & 0 \\ -\sin\phi\cos\lambda & -\sin\phi\sin\lambda & \cos\phi \\ \cos\phi\cos\lambda & \cos\phi\sin\lambda & \sin\phi \end{pmatrix} \begin{pmatrix} X_p - X_r \\ Y_p - Y_r \\ Z_p - Z_r \end{pmatrix}. \tag{A.26}$$

ENU to ECEF This the reverse of the previous coordinate transformation, which is again the application of a rotation matrix:

$$\begin{pmatrix} X \\ Y \\ Z \end{pmatrix} = \begin{pmatrix} -\sin\lambda & -\sin\phi\cos\lambda & \cos\phi\cos\lambda \\ \cos\lambda & -\sin\phi\sin\lambda & \cos\phi\sin\lambda \\ 0 & \cos\phi & \sin\phi \end{pmatrix} \begin{pmatrix} x \\ y \\ z \end{pmatrix} + \begin{pmatrix} X_r \\ Y_r \\ Z_r \end{pmatrix}. \tag{A.27}$$

A.4. AZEL

The AZimuth-ELevation coordinate system, also known as the radar instrument coordinates or the horizontal coordinate system, consists of the instrument antenna looking angles. The coordinates for a point in space are the azimuth angle α, the

elevation angle γ and the range r. The following coordinates transformations are used to transform coordinates back and forth from the ENU coordinate system.

ENU to AZEL

$$x = r \cos \gamma \sin \alpha, \tag{A.28}$$
$$y = r \cos \gamma \cos \alpha, \tag{A.29}$$
$$z = r \sin \gamma. \tag{A.30}$$

AZEL to ENU

$$\gamma_0 = \tan^{-1} x/y, \tag{A.31}$$

$$\gamma = \begin{cases} \gamma_0 & \text{for} & y >= 0 \\ \gamma_0 + \pi & \text{for} & y < 0 \text{ and } \lambda_0 < 0 \\ \gamma_0 - \pi & \text{for} & y < 0 \text{ and } \lambda_0 > 0. \end{cases} \tag{A.32}$$

The inverse tangent is typically implemented with the "atan2´´ function to get the right sign. The range r and the azimuth α are then found with:

$$r = \sqrt{x^2 + y^2 + z^2}, \tag{A.33}$$
$$\alpha = \sin^{-1}(z/r). \tag{A.34}$$

Effective earth correction   As a radio ray passes through the atmosphere, the length and direction of its path vary with the radio refractive index. A simple first-order correction is given by Doviak and Zrnić (1993), known as the effective earth correction, or the 4/3 effective earth assumption. The coordinates x, y, and z transformation between AZEL radar coordinates r, θ_e, and ϕ and ENU coordinates are given in the following formulas. Here is γ' the sum of the beam's elevation angle to the data point and the angle subtended by the verticals at the radar and the measurement point. Note that z is different here from Doviak and Zrnić (1993), because we stick here to the ENU representation of coordinates, whereas in Doviak and Zrnić (1993) $z = (a_e^2 + r^2 + 2r a_e \sin \theta_e)^{1/2} - a_e$ and it presents the height above the surface.

AZEL to ENU with effective earth correction

$$\gamma' = \gamma + \tan^{-1}[r \cos \gamma/(a_e + r \sin \gamma)], \tag{A.35}$$
$$x = r \cos \gamma' \sin \alpha, \tag{A.36}$$
$$y = r \cos \gamma' \cos \alpha, \tag{A.37}$$
$$z = r \sin \gamma', \tag{A.38}$$

where γ' is the modified elevation angle.

ENU to AZEL with effective earth correction   The inverse of the above coordinate transformation is:

$$r = \sqrt{x^2 + y^2 + z^2}, \tag{A.39}$$

$$\alpha = \tan^{-1}(x/y), \tag{A.40}$$

$$\gamma' = \sin^{-1}(z/r). \tag{A.41}$$

$$\tag{A.42}$$

To obtain γ from γ' we have to solve:

$$\tan(\gamma' - \gamma) = \frac{r \cos \gamma}{a_e + r \sin \gamma}. \tag{A.43}$$

By using trigonometric identities, the following solution can be found:

$$\gamma_{12} = \tan^{-1}\left(\frac{\tan \gamma' \pm (r/a_e)\sqrt{1 + \tan^2 \gamma' - (r/a_e)^2}}{1 - (r/a_e)^2}\right) \tag{A.44}$$

A.5. BEAM

The BEAM coordinate system describes points in space with regards to a given reference radar antenna looking direction. The beam coordinates are the offset angle θ (with regards to the center beam), the azimuth angle ϕ, and the range r. It is thus a spherical coordinate system, where $\theta = 0$ for the center of the beam, and for increasing θ the points in space go away from the radar beam center. Note that the range r is the same in the BEAM coordinate system as in the AZEL coordinate system.

The conversion between the BEAM and the AZEL coordinate system, can be best understood by reminding ourselves how a spherical coordinate system is related to a Cartesian coordinate system with coordinates (x, y, z). For example, a BEAM coordinate (ϕ, θ, r) can be presented as a Cartesian coordinate (x, y, z) with reference point (x_0, y_0, z_0):

$$x - x_0 = r \sin \theta \cos \phi, \tag{A.45}$$

$$y - y_0 = r \cos \theta, \tag{A.46}$$

$$z - z_0 = r \sin \theta \sin \phi. \tag{A.47}$$

Here the beam azimuth ϕ is thus the difference with regards to the x-axis.

AZEL to BEAM   A convenient way of going from AZEL to BEAM is to use the difference in azimuth $(\alpha - \alpha_0)$, and the difference in elevation $(\gamma - \gamma_0)$. Here (α_0, γ_0) are the AZEL coordinates for the main beam direction, and (α, γ) are the AZEL coordinates for the actual beam direction. We can then go from AZEL coordinates (α, γ) to beam coordinates (ϕ, θ) via the following transformation:

$$\tan(\alpha - \alpha_0) = \tan \theta \cos \phi, \tag{A.48}$$

$$\sin(\gamma - \gamma_0) = \sin \theta \sin \phi. \tag{A.49}$$

BEAM to AZEL   For the reverse action, the formulas are:

$$\cos\theta = \cos(\gamma - \gamma_0)\cos(\alpha - \alpha_0), \qquad\qquad\qquad \text{(A.50)}$$
$$\tan\phi = \tan(\gamma - \gamma_0)\sin(\alpha - \alpha_0). \qquad\qquad\qquad \text{(A.51)}$$

About the author

Albert C.P. Oude Nijhuis received his MSc degree in Meteorology and Physical Oceanography at the Utrecht University in 2012. He worked as a satellite remote sensing researcher at the Royal Dutch Meteorological Institute (KNMI). After that, he worked on improvements for the OMI total ozone column DOAS technique and for the ISOTROP project on satellite retrieval error estimation of e.g. tropospheric NO2 for the new generation of European Sentinel research satellites. In January 2013 he started as a PhD candidate at the Delft University of Technology, working on new retrieval techniques for wind and turbulence parameters by using radar and lidar observations. After his PhD, he started working as a weather data scientist at SkyEcho.

List of Publications

Journal articles

1. Oude Nijhuis, A. C. P., and Coauthors, 2018: Wind hazard and turbulence monitoring at airports with lidar, radar and Mode-S downlinks: The UFO Project. Bull. Am. Meteorol. Soc., 99 (11), 2275–2293.

2. Oude Nijhuis, A. C. P., C. M. H. Unal, O. A. Krasnov, H. W. J. Russchenberg, and A. G. Yarovoy, 2018: Velocity-based EDR retrieval techniques applied to Doppler radar measurements from rain: Two case studies (under review). J. Atmos. Ocean. Technol., - (-), –.

3. Oude Nijhuis, A. C. P., F. J. Yanovsky, O. Krasnov, C. M. H. Unal, H. W. J. Russchenberg, and A. G. Yarovoy, 2016: Assessment of the rain drop inertia effect for radar-based turbulence intensity retrievals. Int. J. Microw. Wirel. Technol., 8 (6), 835–844.

Conference proceedings

1. Oude Nijhuis, A. C. P., C. M. H. Unal, O. A. Krasnov, H. W. J. Russchenberg, and A. G. Yarovoy, 2014: Outlook for a new wind field retrieval technique: The 4D-Var wind retrieval. Int. Radar Conf., 1–6.

2. Yanovsky, F. J., D. M. Turenko, A. C. P. Oude Nijhuis, O. A. Krasnov, and A. G. Yarovoy, 2015: A new model for retrieving information about turbulence intensity from radar signal. 2015 Signal Process. Symp., IEEE, 1–6.

3. Yanovsky, F. J., A. C. P. Oude Nijhuis, O. A. Krasnov, C. M. H. Unal, H. W. J. Russchenberg, and A. G. Yarovoy, 2015: Turbulence intensity estimation using advanced radar methods. Radar Conf. (EuRAD), 2015 Eur., 141–144.

4. Oude Nijhuis, A. C. P., O. A. Krasnov, C. M. H. Unal, H. W. J. Russchenberg, and A. G. Yarovoy, 2015: Exploitation of homogeneous isotropic turbulence models for optimization of turbulence remote sensing. 15th Eur. Turbul. Conf. 2015, Delft.

5. Oude Nijhuis, A. C. P., O. A. Krasnov, A. G. Yarovoy, C. M. H. Unal, and H. W. J. Russchenberg, 2016: Implementation of wind vector and turbulence intensity retrievals: Application to fast scanning X-band radar. 2016 IEEE Metrol. Aerosp., Florence, 113–117.